



Universiteit
Leiden
The Netherlands

Graphene at fluidic interfaces

Belyaeva, L.A.

Citation

Belyaeva, L. A. (2019, October 23). *Graphene at fluidic interfaces*. Retrieved from <https://hdl.handle.net/1887/79822>

Version: Publisher's Version

License: [Licence agreement concerning inclusion of doctoral thesis in the Institutional Repository of the University of Leiden](#)

Downloaded from: <https://hdl.handle.net/1887/79822>

Note: To cite this publication please use the final published version (if applicable).

Cover Page



Universiteit Leiden



The handle <http://hdl.handle.net/1887/79822> holds various files of this Leiden University dissertation.

Author: Belyaeva, L.A.

Title: Graphene at fluidic interfaces

Issue Date: 2019-10-23

GRAPHENE AT FLUIDIC INTERFACES

PROEFSCHRIFT

Ter verkrijging van
de graad van Doctor aan de Universiteit Leiden,
op gezag van Rector Magnificus Prof. mr. C. J. J. M. Stolker,
volgens besluit van het College voor Promoties
te verdedigen op woensdag 23 Oktober 2019
klokke 15.00 uur

Liubov Alexandrovna Belyaeva
geboren te Nabereznie Chelny, Rusland, 1990

Samenstelling Promotiecommissie

Promotors

Prof. dr. J. Aarts

Prof. dr. A. Kros

Copromotor

Dr. G. F. Schneider

Overige Leden

Prof. dr. H.S. Overkleeft, LIC (voorzitter)

Prof. dr. J. Brouwer, LIC (secretaris)

Dr. L. Juurlink, LIC

Dr. E. M. Blokhuis, LIC

Prof. dr. P. Rudolf, University of Groningen

Prof. dr. D. Bonn, University of Amsterdam

Prof. dr. H. Liu, University of Pittsburgh

“Life is nothing but an electron looking for a place to rest”

Albert Szent-Györgyi

Table of Contents

CHAPTER 1	7
Introduction	
CHAPTER 2	47
Molecular caging of graphene with cyclohexane: transfer and electrical transport	
CHAPTER 3	63
Liquids relax and unify strain in graphene	
CHAPTER 4	89
Contact angle measurement of freestanding square millimetre single layer graphene	
CHAPTER 5	105
Hydrophilicity of graphene in water through transparency to polar and dispersive interactions	
CHAPTER 6	123
Macroscopic and microscopic wettability of graphene: substrate effect	
CHAPTER 7	137
Summary, conclusions and outlook	
APPENDIX 1	143
Supporting information to Chapter 2	
APPENDIX 2	147
Supporting information to Chapter 3	
APPENDIX 3	159
Supporting information to Chapter 4	
APPENDIX 4	171
Supporting information to Chapter 5	

APPENDIX 5	189
Supporting information to Chapter 6	
Samenvatting	193
Curriculum vitae	197
List of publications	199

CHAPTER 1

Introduction

Graphene is a two dimensional (2D) allotrope of carbon, in which carbon atoms are packed in a hexagonal crystalline lattice.¹ Each carbon atom has four outer electrons, the s , p_x , and p_y orbitals which all participate in sp^2 hybridization and form three σ bonds with three neighbor atoms, and the electron on the p_z orbital forms a π bond. The π bonds result in an extended conjugated aromatic system over the entire graphene layer. Such electronic structure and, particularly, the π and π^* bands give rise to the diversity of graphene's remarkable electronic properties.² First, ideal graphene is a zero-gap semiconductor, or a semimetal, with the valence and conductance bands meeting at the Dirac points (Figure 1.1a).^{2,3} Unlike most semiconductors, graphene exhibits a linear energy dispersion relation (and, therefore, conical valence and conductance bands as opposed to parabolic, see Figure 1.1a), which implies that electrons are massless (or Dirac electrons, *i.e.* obeying the Dirac equation) and behave relativistically, moving with a speed close to the speed of light.^{2,3} Additionally, graphene shows outstanding hole and electron mobilities, reaching $15000 \text{ cm}^2 \text{ V}^{-1} \text{ s}^{-1}$ at room temperature.⁴ Anomalous Hall effect is another notable consequence of the unique electronic properties of graphene.⁵⁻⁷ Separately, the network of covalent C-C bonds makes graphene the strongest material, with a reported tensile strength of 130.5 GPa and a Young modulus of 1 TPa.⁸ Graphene is intrinsically rippled, with out-of-plane deformations up to 1 nm, as perfectly flat graphene is thermodynamically unstable.⁹⁻¹¹ Due to its linear energy dispersion and conical band structure, graphene absorbs $\sim 2.3\%$ of light and thus can even be visible by naked eye (Figure 1.1b).^{12,13} Finally, graphene is one of the most thermally conductive materials with reported thermal conductivity values of $1500\text{--}2500 \text{ Wm}^{-1}\text{K}^{-1}$.^{14,15}

The combination of these most prominent properties made graphene one of the most studied materials since it had been isolated in 2004.¹ Graphene offers rich fundamental physics as well as vast application opportunities, including field effect transistors, gas sensors, wearable electronics, water filtration, DNA sequencing, to name a few.¹⁶⁻²² Most far reaching promises relate to the exploitation of its "all in one package" unique electronic properties, mechanical robustness, atomic thinness and large surface-to-volume ratio.

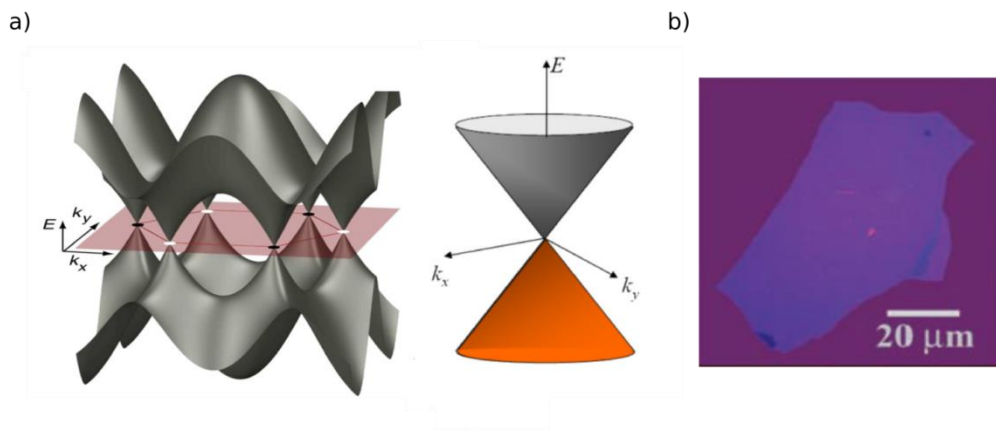


Figure 1.1. Electronic and optical properties of graphene. a) Dirac point and band structure of ideal monolayer graphene.²³ b) Optical image of a monolayer graphene flake exfoliated from graphite and transferred to a silicon/silicon oxide wafer (n-doped, with a silicon oxide layer of 300 nm) using the scotch tape method.¹

1.1. Fabrication of graphene

Mechanical exfoliation of graphite with scotch tape was the first successful method used to isolate a single layer of graphene (see Figure 1.1b for an example of mechanically-exfoliated monolayer graphene flake).¹ Although a great number of fundamental physical properties were discovered using mechanically-exfoliated graphene,^{7,24–27} the scotch-tape method only yields small micrometer-sized monolayer flakes with a very low yield (although of high quality). The expanding research and industrial interests demand – instead – larger flakes and scalable processes for producing graphene. Since 2004, various graphene production methods have been developed: chemical vapor deposition (CVD),^{28–34} chemical exfoliation of graphite and graphite oxide,^{35–37} epitaxial growth,³⁸ total organic synthesis,^{39,40} liquid-phase exfoliation (sonication of graphite suspensions),⁴¹ pyrolysis⁴² and carbon nanotube slicing.^{43,44} Depending on the method, graphene is obtained in the form of continuous supported monolayers (CVD, epitaxial growth, carbon nanotube slicing), powders or suspensions (chemical and liquid-phase exfoliation, pyrolysis). Each of these production

methods yield graphene of various structural characteristics, such as number of layers, crystallinity, flake size, intrinsic roughness, presence of functional groups, adatoms and defects.^{45,46} Such diversification, on one hand, creates a versatile toolbox for the usage of graphene, but, on the other hand, results in graphene materials with appreciably different (electronic and mechanical) characteristics and overall performance in devices, which must be considered whenever the generic “graphene” term occurs.⁴⁶

Currently, CVD proved to be the most optimal method to fabricate graphene on a large scale.^{28–34} Essentially, graphene is produced through the dehydrogenation of a hydrocarbon precursor (usually methane or ethene) in presence of a metal catalyst, followed by the adsorption of carbon atoms on the surface of the catalyst, which in a last step arrange into the hexagonal graphene lattice (Figure 1.2a). Typically, the growth process is self-limited, and terminates when the catalyst is passivated with a continuous graphene monolayer.⁴⁷ In some cases, however, single islands of bi- and few-layers graphene may grow (Figure 1.2b),⁴⁸ particularly on a metal such as nickel in which the solubility of carbon is higher, compare to copper.³³ Depending on the exact growth conditions, CVD can yield mono- or polycrystalline graphene with, in principle, controllable domain size and orientation,⁴⁹ and with charge carrier mobilities almost as high as in mechanically exfoliated graphene.^{50,51} Advantageously to other production methods, the maximal size of the graphene sheet is only limited by the dimensions of the oven, reportedly reaching $5 \times 50 \text{ cm}^2$.⁴⁹

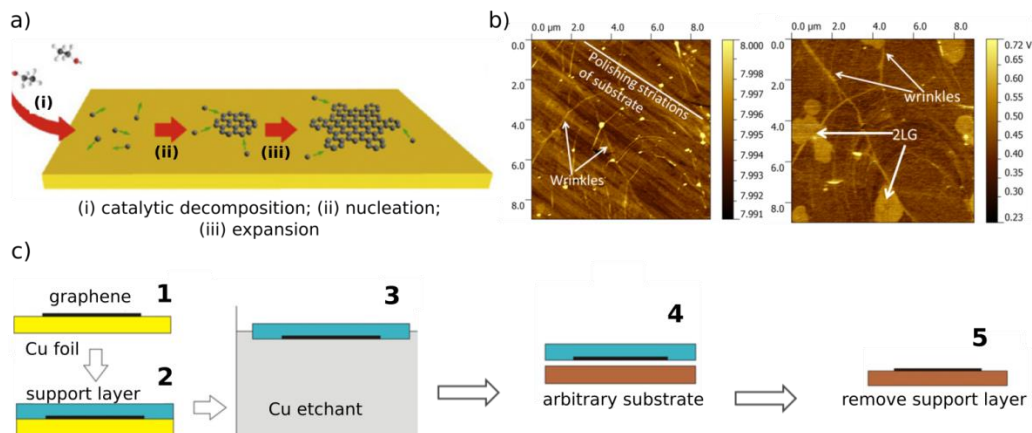


Figure 1.2. Most common methods to produce and transfer graphene on a large scale.

a) Illustration of chemical vapour deposition (CVD) for the growth of graphene on a metal catalyst.⁵² b) Atomic force microscopy (AFM) and scanning Kelvin probe microscopy (SKPM) images of CVD-grown graphene on a quartz substrate illustrating imperfections in graphene morphology common for CVD-grown samples: wrinkles, bilayers, grain boundaries.⁵³ c) Schematics of the most commonly used polymer-assisted method to transfer graphene:⁵⁴ 1) graphene is grown on copper, 2) a support polymeric layer is deposited on graphene on copper, 3) copper is etched, 4) the polymer/graphene stack is transferred on a target substrate, and 5) the polymer support layer is removed.

1.2. Methods to transfer graphene

The CVD method produces graphene on metallic (*i.e.* conductive) supports, while for most applications, especially in electrical circuits, an insulating layer underneath graphene is required. The routine transfer of an atomically thin layer from substrate to substrate, preserving the pristine excellent properties, is very challenging and stimulated the development of several transfer approaches. The earliest and the most common transfer method utilizes a polymer, typically poly(methyl methacrylate) (PMMA), as a support layer to preserve the integrity of graphene during the transfer (Figure 1.2c).^{54–57} After coating graphene with the polymer, the metal/graphene/polymer stack is placed floating on the surface of an aqueous solution of the metal etchant (Figure 1.2c). Then, once the metal support is fully etched, the graphene/polymer stack is transferred on the target

substrate (Figure 1.2c). In a last step, the polymer layer is dissolved in an organic solvent, typically acetone (Figure 1.2c). The use of a polymer support allows transferring large (centimeter-size) graphene sheets. The drawback, however, is that the polymer drastically contaminates the graphene surface,^{58,59} hindering its intrinsic thermal conductivity⁶⁰ and reducing charge carrier mobilities due to introduced doping and additional scattering sites.^{61–64} Moreover, polymer supports also induce extrinsic roughness and other morphological defects in graphene, affecting its properties.⁶⁵ Many potential applications of graphene are based on the exceptional sensitivity of its surface to the environment²⁰ and, therefore, transferring graphene using a clean transfer methodology is crucial.

To overcome the contamination introduced by polymers, several polymer-free strategies were developed.^{66–71} Generally, the transfer scheme resembles that of the polymer-assisted method, with the distinction that the polymer is substituted with a non-polymeric supporting layer, such as a metal,⁷² a naphthalene film,⁷¹ liquid hexane,⁶⁷ or even using graphite holders.⁶⁶ The major drawbacks of all polymer-free methods, however, are the morphological distortion of the graphene surface (cracks, wrinkles, folds) caused by the capillary forces and conformational mismatch between graphene and the supportive layer, which not only prevent the scalability of the transfer methods, but also alter the electronic, mechanical, thermal and wetting properties of graphene.^{65,73}

In summary, despite active research efforts, the transfer and handling of graphene still pose nontrivial challenges on the way towards widespread application and production of graphene-based devices. For the physics community exfoliated graphene still represents the standard, particularly since the discovery of the so called van der Waals heterostructures.⁷⁴ For larger graphene flakes, CVD graphene requires clean transfer methods. In Chapter 2 a new polymer-free transfer method is presented, which principally improved the quality of transferred graphene. In this method, the physical properties of cyclohexane were exploited to provide a soft and adaptable yet non-contaminating support to transfer centimeter-sized graphene layers. The electrical characterization of graphene at the water/cyclohexane interface confirmed the superior cleanness and charge carrier mobilities of the graphene which were compared to other well established transfer techniques.

1.3. Graphene at liquid interfaces

Graphene is atomically thin and, therefore, all the carbon atoms composing its surface are always in direct contact with the environment in which graphene is embedded. More precisely, each atom of graphene is always in contact with two media, the one at the bottom and the one on top of the graphene layer. The medium on one side of the graphene surface alters the work function (*i.e.* chemical potential) of graphene, which, in turn, affects the interactions between graphene and the medium on the other side. As a result, experimentally observed (electronic and chemical) properties of graphene are dictated not only by the electronic structure of graphene itself, but also by the combined effects of the interactions between graphene and the media from both sides. Furthermore, the interactions of any particular medium (solid surface, liquid, gas, molecules of adsorbate, etc.) with graphene must be interpreted in the context of the effect of the medium from the other side of graphene. For applications and research purposes where graphene cannot be free-standing in vacuum, understanding the interfacial physics and chemistry of graphene (especially CVD graphene) is, therefore, of paramount importance. Studying the physical and chemical phenomena at graphene interfaces, however, poses two main challenges: the uncontrollable alteration of the surface/physical/chemical properties of graphene introduced during transfer and handling, and the disentanglement of the intrinsic properties of graphene from the effects of the substrate and of the environment (even provided there are no transfer-related alterations).

Specifically, research focused on understanding the effect of the substrate on the properties of graphene. Strain and doping induced by the underlying substrate were found to play the most important roles in affecting the electronic band structure and phononic properties of graphene (Figure 1.3).^{75–81} In fact, unintentional non-uniform strain inevitably occurs due to the corrugations of the graphene sheet caused by the mismatch in structure^{79,81} and thermal expansion coefficients^{83,84} between the graphene and the substrate. Additionally, doping by the substrate is also ubiquitously present in supported graphene.^{80,85}

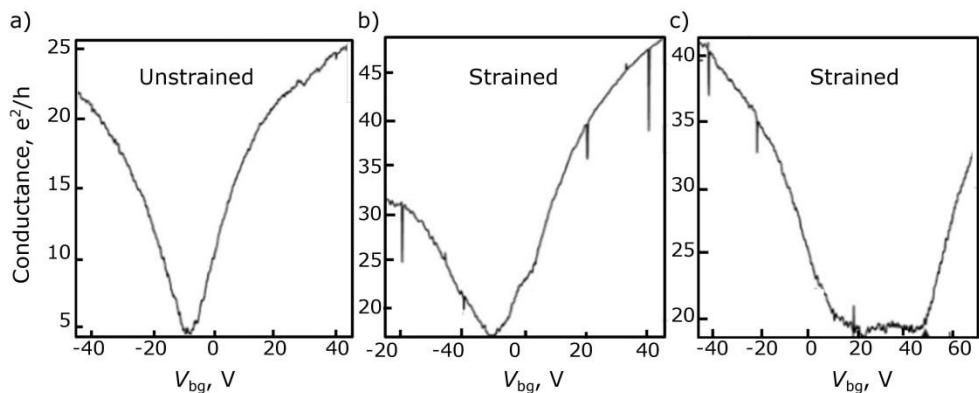


Figure 1.3. Effect of strain on the electronic properties of graphene. Gate voltage (V_{bg}) dependent sheet conductance measured at $T=1.5$ K and $V=100$ μ V for a) unstrained graphene and b, c) for graphene under applied uniaxial strain of different magnitudes.⁸¹

In contrast to graphene on solid supports, studies of graphene's behavior at liquid interfaces are scarce, and mostly limited to studies of the wettability of graphene on solid substrates (*i.e.* graphene at solid/liquid interfaces).⁸⁶ In Chapter 2 the properties of graphene at liquid/liquid interfaces were probed for the first time by measuring charge carrier mobilities of graphene free-floating directly at a liquid/liquid interface. A significant enhancement of the mobilities compared to graphene supported by conventional solid supports was observed at a water/cyclohexane interface. Next, in Chapter 3 confocal Raman spectroscopy was used to characterize graphene at liquid/air and liquid/liquid interfaces. It is shown that, in stark contrast to solid supports, liquid supports induce very small to zero strain and doping in graphene, which is in excellent agreement with the enhanced charge carrier mobilities reported in Chapter 2. Additionally, Chapter 3 exemplifies how the strain relaxation induced by liquid supports could be used to monitor hydrogenation or other functionalization of graphene.

Furthermore, Chapters 4, 5 and 6 present new insights and strategies for studying the wettability of supported, free-standing and free-floating graphene in water. Specifically, Chapter 4 reports the contact angle of fully free-standing graphene in air, Chapter 5 studies the wettability of graphene in water, particularly the diverse factors affecting the wetting of supported graphene, and Chapter 6 compares the interactions between graphene and water at a molecular and bulk levels.

1.4. Wettability of graphene.

The wettability of a solid surface characterizes its affinity to water and provides an indication about possible interactions with molecules other than water.^{87,88} For graphene, however, a simple measurement of the water contact angle yielded a remarkably wide range of values – from hydrophilic to hydrophobic^{89–92} – and an extensive debate over the origin of the contact angle discrepancies, which still seems not resolved. Most researchers now agree that, due to the atomic thickness of graphene, the underlying substrate has a critical effect on the apparent wettability of graphene.^{91,93–97} On the other hand, the extent to which graphene is transparent to wetting is still debated – graphene has been reported to be fully wetting transparent,⁹³ partially wetting transparent^{96,98,99} and fully opaque.^{91,92,100} As discussed previously, the apparent (*i.e.* observed experimentally) wettability of graphene is determined by the intrinsic wettability of graphene and external factors. The intrinsic wettability of graphene is dictated solely by the properties of pristine and isolated graphene, a situation which does not occur practically. All external factors altering the intrinsic wettability of graphene can be categorized into 1) fundamental substrate effects and 2) environmental effects. The substrate effects include well-defined (as opposed to environmental) effects of the polarity¹⁰¹ and doping of the substrate.^{102,103} In principle, the intrinsic wettability and the substrate effects are sufficient to describe the wettability of supported graphene. They are, however, often hindered by the environmental effects, which are induced unintentionally during sample preparation (different graphene production methods,^{104,105} transfer and handling-related contamination and structural irregularities⁵⁷) and measurement conditions (adsorption of air contaminants^{98,106}). Environmental factors do not represent the properties of graphene, nor of the substrate, and often cause non-negligible sample-to-sample variations and, therefore, must be minimized.¹⁰⁶ In practice, however, the contributions of the substrate and of the environment are difficult to disentangle. The following subchapters will introduce the intrinsic wettability of graphene, and discuss how it is affected by the substrate and the environment.

In addition to the conventional characterization of wettability in ambient by means of contact angle measurements, interactions between graphene and other molecules in ultra-high vacuum (UHV) were also investigated using surface science methods.^{107–113} For example, the comparison between the UHV and the ambient studies demonstrated that microscopic hydrophobicity does not straightforwardly translate into macroscopic hydrophobicity, but rather provides complementary insights.

1.4.1. Thermodynamics of graphene wetting

The surface energy of a solid σ_S is the interfacial tension of solid-gas interface σ_{SG} and is defined as an excess energy of its surface compared to the bulk, and related to the contact angle θ with the Young equation (Figure 1.4a):

$$\sigma_{SG} - \sigma_{SL} - \sigma_{LG} \cos\theta = 0,$$

where σ_{SL} is solid-liquid interfacial energy and σ_{LG} is liquid-gas interfacial energy (or surface tension of the liquid σ_L).

Graphene and other two-dimensional (2D) materials do not have a bulk phase, and, therefore, the definition of the surface energy cannot be applied to describe a completely isolated monolayer graphene. The contact angle and the surface energy of graphene, therefore, must be always regarded in the context of the underlying substrate (or liquid and gaseous medium underneath graphene). In fact, similarly to the water contact angle measurements, attempts to determine the surface energy of graphene resulted in very sparse and spreaded values. As a few examples, the surface energy was reported to be 46.7 mJ/m² for graphene on a silicon substrate (chemically exfoliated flakes),¹¹⁴ 62.2 ± 3.1 mJ/m² for graphene on copper (CVD),⁹⁸ 40.4 mJ/m² for graphene on PDMS (CVD),⁹⁶ 48.8 mJ/m² for graphene on glass⁹⁶ and 115±4 mJ/m² for suspended graphene (CVD).¹¹⁵ These examples demonstrate that the deviations from the structurally ideal non-contaminated graphene surface, caused by the environmental (production method, transfer, environment) factors and by the effect of the underlying substrate, result in graphene interfaces with significantly different

wetting properties. Theoretical studies also show disagreement: molecular dynamic (MD) simulations predict a surface energy of zero,¹¹⁶ whereas quantum Monte Carlo and advanced density-functional first-principles calculations predict values in the range 144-171 mJ/m².^{117,118} The type of interactions between graphene and a wetting liquid can be determined from the contributions of polar (hydrogen bonding, dipole-dipole and dipole-induced dipole) and dispersive (London-van der Waals) interactions to the total surface energy,¹¹⁹ by measuring multiple contact angle measurements with liquids of different polarities as described in Fowkes,¹²⁰ Owens-Wendt¹²¹ or Neumann model (Figure 1.4b).¹²²⁻¹²⁴ Interestingly, such an approach yielded more consistent results than determining the total surface energy (*i.e.* the sum of dispersive and polar contributions): most studies agree, in qualitative terms, on the dominance of the dispersion forces in the surface energy of graphene.^{96,98,101,125} Moreover, by comparing polar (σ_s^P) and dispersive (σ_s^D) components of graphene-on-a-substrate ($\sigma_{s_2}^D$ and $\sigma_{s_2}^P$ in Figure 1.4c) and those of the bare substrate ($\sigma_{s_1}^D$ and $\sigma_{s_1}^P$ in Figure 1.4c), the transmittance of graphene to specific interactions (polar or dispersive) can be estimated (Figure 1.4c),¹²⁶ providing new insights into the chemical origin of the wetting transparency of graphene.

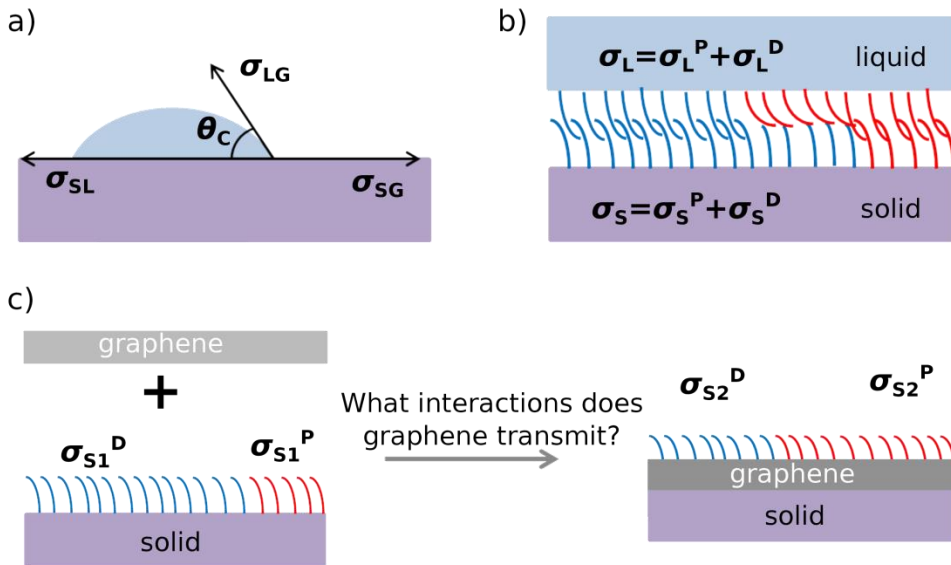


Figure 1.4. Thermodynamics of graphene wetting. a) Three phase equilibrium diagram in the sessile drop technique: θ_c is the contact angle and σ_{SL} , σ_{LG} and σ_{SG} are the interfacial tensions at solid-liquid, liquid-gas and solid-gas interfaces respectively. b) Model of polar and dispersive interactions between a solid and a liquid represented by the polar (σ_S^P and σ_L^P) and dispersive (σ_S^D and σ_L^D) components of the surface tensions σ_S and σ_L . Blue and red lines depict the contributions of dispersive and polar interactions respectively. c) Illustration of the effect of graphene transmitting polar and dispersive components of the surface energy of the solid substrate. The addition of a graphene layer on top of the solid changes the contributions of polar and dispersive interactions from σ_{S1}^D and σ_{S1}^P to σ_{S2}^D and σ_{S2}^P .

Chapter 5 demonstrates that in the case of a clean non-corrugated graphene-substrate interface (*i.e.* when the interface was not exposed to air and was not subjected to any transfer-related contamination and mechanical deformation), the graphene is transparent to both polar and dispersive interactions independently of the polarity of the substrate. Remarkably, graphene was almost entirely opaque to polar interactions when it was transferred on a substrate using PMMA transfer, presumably due to contamination and morphological distortions.

1.4.2. Wetting of free-standing graphene

The characterization of the intrinsic wetting properties of graphene is technically complicated, because both the environmental factors and the substrate contribute to the observed wetting characteristics. The influence of the substrate can be eliminated in a free-standing geometry. However, so far, it was only possible to make graphene free-standing over a few square micrometers, rendering difficult to measure the contact angle of a microliter droplet (with a millimeter range diameter). Simulations of the contact angle of water on free-standing graphene have been challenging as well and were shown to highly depend on the choice of the graphene-water interaction model. Suchwise, independent MD simulations resulted in the contact angles of suspended graphene as different as $90\text{-}127^\circ$ ^{91,127,128} and $45.7^\circ \pm 1.3^\circ$.¹²⁹

Only a few experimental approaches attempting to circumvent the complications of the conventional contact angle measurements yielded information on the intrinsic wettability of suspended graphene.^{73,90} In the first study, graphene was suspended over hydrophilic and hydrophobic nanopatterned silicon substrates (Figure 1.5a) with varying area fractions of suspended graphene. By extrapolation of the contact angle values of partially suspended graphene, the water contact angle for fully suspended graphene was estimated to be $85^\circ \pm 5^\circ$. Interestingly, the contact angle of partially suspended graphene did not depend on the area of suspended graphene (*i.e.* it was $85^\circ \pm 5^\circ$ for all measured area fractions, Figure 1.5b), and neither on the wettability of the underlying substrate (Figure 1.5b).⁷³ The major drawback of using partially suspended graphene, however, is that the deposition of monolayer graphene on such sharply patterned structures (the conical pillars were 5-15 nm in width, spaced by 10 nm, Figure 1.5a) and the water-based transfer method that was used, created a large density of wrinkles, pinholes and cracks which certainly alter the structural properties of the graphene surface.⁷³ Moreover, the ability of such suspended graphene structures to sustain the weight of a water droplet, particularly for contact angle measurement, was not supported experimentally and is, therefore, questionable.

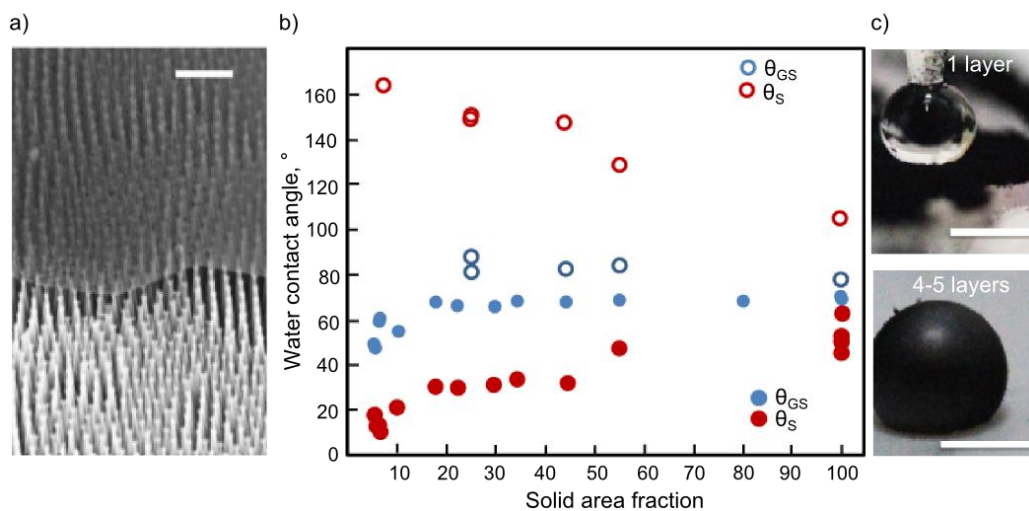


Figure 1.5. Experimental water contact angle measurements on free-standing graphene.

a) Scanning Electron microscopy (SEM) image of a graphene monolayer partially suspended over nanopatterned silicon pillars.⁷³ The scale bar represents 200 nm. b) Contact angle as a function of solid area fraction at the top of the texture.⁷³: water contact angle values for bare hydrophilic pillars (θ_s) are represented by filled red circles, for bare hydrophobic pillars – by hollow red circles; water contact angle values for graphene deposited on hydrophobic and hydrophilic substrates (θ_{GS}) are represented by hollow and filled blue circles respectively. c) Graphene (reduced graphene oxide) nanopowders of monolayer (top) and 4-5 layers (bottom) flakes in contact with a water droplet, *i.e.* the “liquid marble” experiment.⁹⁰ The scale bars represent 2 mm.

In a second study, the wetting properties of suspended graphene were characterized based on the ability of graphene nanopowders to adsorb water.⁹⁰ Graphene nanopowders consisted of nanoflakes of reduced graphene oxide separated by air cavities and, therefore, represented free-standing graphene. Remarkably, water adsorption measurements on such graphene nanopowders of different thicknesses (*i.e.* flakes with different number of stacked graphene monolayers) yielded contact angles of $179^\circ \pm 2^\circ$ (for nanopowders with monolayer flakes), $163^\circ \pm 2^\circ$ (for nanopowders with the flakes of 4-5 layers) and $140^\circ \pm 2^\circ$ (for nanopowders with the flakes of 25 layers).⁹⁰ The “liquid marbles” experiments, in which the ability of a powder to adsorb on a water droplet is tested, also showed

that the nanopowder composed of monolayer flakes is superhydrophobic (no flakes adsorbed on the surface of the droplet, Figure 1.5c) while nanopowder samples with 4-5 layers flakes showed a hydrophobic character (the flakes indeed adsorbed on the surface of the droplet, without intruding inside the droplet, Figure 1.5c). Although the experimental approach was clever from a methodological point of view, reduced graphene oxide powders are, however, different from pristine graphene monolayer as they are structurally disordered materials containing significant amount of oxidized edges (based on Raman spectroscopy and chemical analysis) particularly the powder containing the thinnest flakes (~one layer).

In addition, besides still being indirect indications of the wettability of free-standing graphene, the two approaches described above do not take into account the adsorption of airborne hydrocarbons which are known to substantially alter wetting of graphitic surfaces.^{129,130}

In Chapter 4 a direct contact angle measurement on fully free-standing graphene in air was realized using the so-called captive bubble method, which avoids the mechanical tearing of graphene because of the droplet weight. The captive bubble approach also prevents handling-related structural deformations and contamination of graphene, and, importantly, airborne hydrocarbons adsorption. Essentially, in the captive bubble method an air bubble is injected underneath a graphene monolayer floating at the water-air interface, intrinsically forming a millimeter-scale air-suspended graphene, allowing for the direct measurement of the contact angle, and hence the wettability of free-standing graphene. In contrast with the studies on partially suspended graphene and nanopowders of reduced graphene oxide, the captive bubble method showed that graphene is hydrophilic with a measured water contact angle of $42^{\circ} \pm 3^{\circ}$. Distinctively, the captive bubble experimental design provides measurements on large area of smooth (*i.e.* graphene floats on the surface of water) fully free-standing graphene avoiding any transfer-related contamination and adsorption of hydrocarbons.¹⁰⁶

1.4.3. Effects of the substrate on the wettability of graphene

The substrate on which graphene is transferred or grown has a strong influence on the wettability of graphene. In fact, the underlying substrate alters the electronic structure and, consequently, the chemical potential of graphene. The first MD modelling of van der Waals (vdW) interactions between a liquid and a graphene sheet introduced the “wetting translucency” as opposed to the “wetting transparency” of graphene and suggested that wetting transparency does not occur when graphene is supported by superhydrophobic or superhydrophilic substrates.⁹⁵ The model, however, assumes that the solid-liquid interactions are dominated by vdW forces and does not take into account the electrostatic interactions or hydrogen bonding between liquids and solids, which could also contribute to the wetting properties.

Interestingly, density-functional theory (DFT) calculations showed that the dipole moment of water does not affect the electronic structure and doping in fully suspended graphene.^{89,132} However, if a solid substrate is present (namely, SiO₂¹³² and copper¹⁰¹), the subsequent charge transfer between the substrate and the graphene triggers the polarization effect of water on graphene¹³² and modulates the Fermi level of graphene,^{101,133} all of which result in altering the graphene-water interactions and, therefore, the apparent macroscopic wettability.

Finally, experimental studies also confirmed that inducing p- or n-doping by applying a gate voltage (Figure 1.6a),¹⁰² or by introducing a layer of metal or polyelectrolytes (namely poly(sodium 4-styrenesulfonate), poly(acrylic acid), poly(allylamine hydrochloride) and poly-L-lysine) between graphene and the substrate, and by fabricating metal-graphene heterojunctions,¹⁰³ alters the properties of graphene towards more hydrophilic (Figure 1.6b).^{102,103} According to DFT and molecular dynamics calculations, the induced doping modulates the charge carrier density in graphene and binding energy between graphene and water, which affects the wettability of graphene.¹⁰³

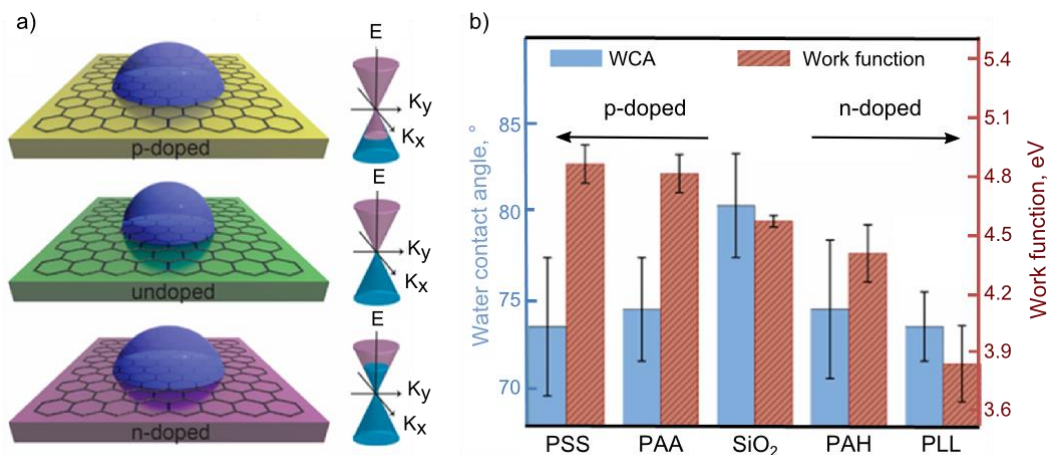


Figure 1.6. Effect of doping on the water contact angle of graphene. a) Illustration of the effect of the doping-induced shift of the Fermi level of graphene on the measured water contact angle.¹⁰³ b) Water contact angle and work function of undoped graphene on SiO₂ substrate and of graphene doped by introducing a layer of poly(sodium 4-styrenesulfonate) (PSS), poly(acrylic acid) (PAA), poly(allylamine hydrochloride) (PAH) and poly-L-lysine (PLL) between graphene and the SiO₂ substrate.¹⁰³

1.4.4. Environmental factors affecting the wettability of graphene

Environmental factors are the factors responsible for the variability of reported contact angles due to sample preparation and measurement conditions (adsorption of airborne hydrocarbons, growth and transfer of graphene).

The adsorption of airborne hydrocarbons is the major cause of the false apparent hydrophobicity of graphitic surfaces and false apparent contact angle of $\sim 90^\circ$.^{106,129,133–136} In fact, ellipsometry and attenuated total reflectance-Fourier transform infrared spectroscopy (ATR-FTIR) studies showed that a 5 Å thick layer of hydrocarbon contaminants forms on graphite upon exposure to air.¹³⁸ Disproving the long-held belief, first, graphite,¹³⁰ and then graphene^{98,106} were demonstrated to be intrinsically mildly hydrophilic exhibiting contact angles of $\sim 60^\circ$ and $\sim 40^\circ$ (for graphene on copper) respectively, when the measurements were conducted on contamination-free samples (Figure 1.7a). Hydrocarbons are

ubiquitously present in the environment. Even storing graphene samples in a plastic Petri dish as opposed to a glass one results in a noticeable increase of the contact angle in the course of fifteen minutes (Figure 1.7b).¹⁰⁶ Thermal annealing, ultraviolet ozone treatment¹⁰⁶ and hydrogen plasma¹³⁹ can be utilized to remove the adsorbed hydrocarbons from graphene (Figure 1.7c). Another way to preserve the intrinsic wettability of graphene is to store graphene at low temperature (-15°C): a protective layer of ice forms on the graphene surface preventing hydrocarbon adsorption.¹⁴⁰ Contact angle measurements (and any other surface inspection) on graphene samples must, therefore, be conducted within minutes after growth or using the surface treatments mentioned above.

Separately, the broad diversity of synthetic¹⁰⁴ and transfer⁵⁷ methods yield graphene materials with different surface properties.^{45,105} Most wettability studies were performed on CVD grown graphene, as CVD is the most convenient method to produce large sheets of monolayer graphene up to now, suitable for contact angle measurements.²⁸⁻³⁴ However, even considering only CVD graphene samples, varying the growth conditions (catalytic metal, morphology of the substrate, temperature, pressure, annealing conditions, precursor gas, gas flow, presence of oxygen and hydrogen) results in different number of layers, domain size and orientation, type and density of defects, density of oxidized carbon atoms, size and density of wrinkles and other morphological features, which affect the wetting behavior of graphene.¹⁴¹ For example, the introduction of point defects in the graphene lattice using an oxygen plasma changed the contact angle of graphene on SiC from 92.5° to 55.1°, and the subsequent restoration of the graphene lattice upon annealing in UHV increased the contact angle to 87.3°, close to the pristine value.¹⁰⁰ Separately, the effect of line defects (dislocations and grain boundaries) on the wetting of graphene was probed by scanning tunnelling microscopy (STM) and indicated that interactions between water and line defects in graphene caused water to intercalate and split the graphene into fragments.¹⁴² Interestingly, this phenomenon was shown to be substrate-dependent and was observed for graphene on Ru(0001) but not on Cu(111), with copper known to interact more weakly with graphene.¹⁴² Also, a number of MD studies reported that the imperfections in graphene, such as multilayers,¹²⁶ holes¹⁴³ and roughness^{99,126} generate a variety of wetting states (Figure 1.7d),

naturally implying that varying their concentrations and dimensions would result in different wettabilities.

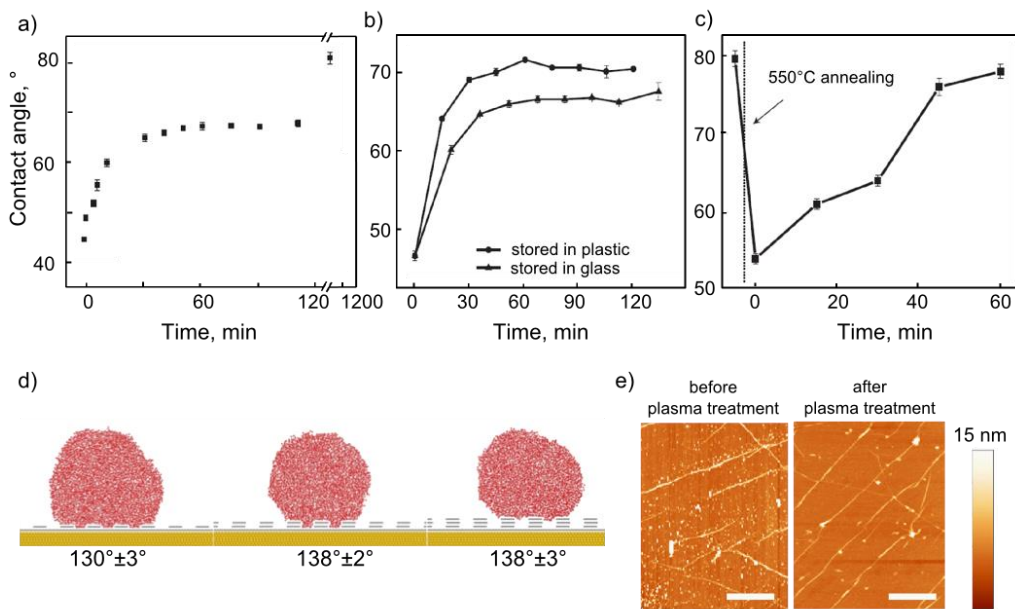


Figure 1.7. Environmental effects affecting the wettability of graphene. a) Water contact angle of monolayer graphene-on-copper upon exposure to ambient air after CVD growth.¹⁰⁶ b) Water contact angles of graphene-on-copper stored in plastic and glass Petri dishes as a function of storage time.¹⁰⁶ c) Effect of annealing at 550°C in argon atmosphere on the water contact angle of graphene on copper.¹⁰⁶ d) MD simulation of the effect of surface morphology on the water contact angle of graphene.¹²⁶ e) AFM images of wrinkles, folds, contamination and other imperfections in graphene transferred on a Si/SiO₂ substrate using the PMMA-assisted method before (left) and after (right) hydrogen plasma.¹³⁹

Yet, the transfer of graphene from the growth catalyst to a target substrate induces even larger irregularities (ripples, folds, cracks, contamination) in the graphene structure and graphene-substrate interface, and causes additional sample-to-sample variations (Figure 1.7e).^{62,138,144} The most widely used polymer-based transfer methods irreversibly contaminate the surface with polymer residues (Figure 1.7e),^{144,146–148} whereas alternative polymer-free transfer

methods provide minimal contamination,^{66–70} but often at the cost of disintegrity and formation of micrometer-sized folds and wrinkles in the graphene layer.⁶⁴

Chapter 5 presents a comparative study of three types of samples: non-transferred graphene samples, graphene transferred using a polymer-free method and samples transferred using PMMA. Interestingly, non-transferred graphene samples were transparent to wetting, graphene transferred using a polymer-free method significantly altered the contact angle and surface energy of the substrate, and samples transferred using PMMA yielded irreproducible wetting behavior, suggesting that transfer, contamination and handling yield graphene with large sample-to-sample variation from very hydrophilic to hydrophobic.

1.4.5. Microscopic wettability of graphene

In parallel with the macroscopic investigations in ambient atmosphere, surface science methods were also employed to probe the affinity of water molecules to graphene under UHV conditions, the so-called “microscopic wettability” or wettability at the molecular level.^{107–113,149–151} Measurements under UHV provide extreme pureness of the environment and sensitivity and can, in principle, allow the accurate probing of the interactions between graphene and single water molecules. Temperature programmed desorption (TPD) is a method typically used for investigating the microscopic wettability of surfaces.¹⁵² Essentially, a TPD experiment yields a desorption curve which represents the amount of water molecules (or of other adsorbate) desorbing from a surface upon heating. Typically, a set of curves is recorded at different initial partial pressures of water in the UHV chamber (that is, different coverages of the studied surface with water). The onset temperature at which molecules start desorbing, the shape of the curves and the evolution of the curves with increasing coverage (alignment of the leading edges, tails etc.) provide information about the desorption energy, the kinetic order of desorption, the binding energy and the ordering of the adsorbate molecules in the first and subsequent adsorbate layers.¹⁵²

It must be noted, however, that the wettability at the molecular level cannot be directly compared with the macroscopically observed wettability, as

experimental conditions are different (*i.e.* UHV versus ambient) and TPD studies refer to different molecular events (*i.e.* the adsorption of single molecules versus a collective adsorption of molecules in contact angle measurements). The difference between desorption and reaction mechanisms in UHV and ambient atmosphere, the so-called “pressure gap”, is an interesting subject on its own, and most recent advances in understanding its physical nature can be found elsewhere.¹⁵³

A number of thorough studies reported on the desorption kinetics of water,¹⁰⁹ methanol,¹⁰⁹ ethanol,¹⁰⁹ Ar,¹¹¹ Kr,¹¹¹ Xe,¹¹¹ N₂,¹¹¹ O₂,¹¹¹ CO,¹¹¹ methane,¹¹¹ ethane,¹¹¹ propane,¹¹¹ benzene¹¹² and cyclohexane¹¹² from graphene grown on Pt(111) *in situ* in a UHV chamber. Interestingly, while most adsorbates showed kinetic orders and desorption energies very similar to those on highly oriented pyrolytic graphite (HOPG),¹⁵⁴ water displayed a more complicated behavior at submonolayer coverages (*i.e.* when the amount of water molecules is not enough to form a continuous monolayer): misaligned leading edges, “dips” and “bumps”, peak shifts to higher temperatures upon desorption of the second and subsequent layers. It was reported that the first monolayer of water forms a new ice polymorph on graphene, in which planar hexagons of water molecules are stacked directly on top of each other, maximizing the number of hydrogen bonds (at the expense of their weakening), as opposed to normal puckered three dimensional (3D) hexagonal ice (Figure 1.8a).^{107,109} Although this phenomenon was previously predicted as a result of the confinement of water between two hydrophobic surfaces,^{155,156} the low energy electron diffraction, reflection–absorption infrared spectroscopy and rare-gas adsorption/desorption measurements showed that the surface of graphene actuates the unusual planar ordering of water molecules without any confinement. All other adsorbates (except benzene) manifested zero order kinetics desorption from graphene-on-platinum (111), indicating formation of the islands of condensed adsorbate in equilibrium with individual adsorbate molecules.^{109,111,157} In contrast, benzene showed a first order kinetics at submonolayer coverages on graphene-on-platinum (111), which transitions to zero order for the second and subsequent adsorbed layers, indicating that island formation (*i.e.* when the adsorbate forms multilayer islands instead of continuous monolayer) is unfavorable for aromatic molecules due to the weaker adsorbate-adsorbate (compared to adsorbate-

substrate) attractive interactions.¹¹² In that respect, benzene wets graphene on Pt(111) similarly to HOPG.¹⁵⁸ Methanol and ethanol, on one hand, have similar desorption energies on graphene and on HOPG, but on the other, presented a zero kinetic order on graphene, as opposed to the fractional kinetics orders on HOPG (0.26 and 0.08 respectively).^{109,159,160}

By comparing the desorption characteristics of graphene on various substrates with those of the bare substrates, the substrate effect and the wetting transparency were assessed.^{113,150,151} Interestingly, the transparency of graphene to desorption was shown to strongly depend on the adsorbate. Particularly, silicon and copper substrates strongly affect desorption of benzene,¹⁵⁰ n-pentane,¹¹³ butane¹⁵¹ and water¹⁴⁹ from graphene, even manifesting full transparency in the case of benzene (no data was presented for the desorption of n-pentane and butane from bare substrates thus no conclusion about wetting transparency in these cases could be made). The effect of the substrate on the microscopic wettability of graphene can be deduced as a difference between desorption energies of an adsorbate from graphene-on-a-substrate and from the bare substrate.^{113,150,151} For example, the desorption energies and their coverage dependences of benzene on copper and on silicon were not affected by the graphene layer at all (Figure 1.8b and c).¹⁵⁰ Water, in contrast, exhibits different desorption characteristics (kinetic order and desorption energy) on substrates (namely, silicon and copper) with and without graphene layer.¹⁴⁹ Interestingly, graphene-coated SiO₂ appeared to be more hydrophilic than bare SiO₂, and graphene-coated copper appeared to be more hydrophobic than bare copper.¹⁴⁹ Also, a complex desorption behavior of graphene on ruthenium (0001) was reported: no transparency to the desorption of water¹¹⁰ and benzene,¹⁰⁸ but full transparency to desorption of n-butane.¹⁵¹ These findings can be related to the fact that water intercalates and splits graphene on Ru(0001), as it was observed by STM.¹⁴²

Finally, the preparation and the quality of graphene samples must be taken into consideration in microscopic wettability studies as it is in the macroscopic contact angle measurements. In fact, graphene on Pt(111) and Ru(0001) were grown *in situ* in the UHV chamber, graphene on copper was grown using the CVD method and then mounted in the UHV chamber for desorption measurements, and graphene on SiO₂ was grown by CVD and then transferred using the PMMA-

assisted method (with polymer residues inevitably adsorbed on the graphene surface). Certainly, graphene grown *in situ* in UHV on well-defined smooth and extremely clean metallic surfaces is expected to be of higher quality and to represent properties of a single layer of ideal (non-contaminated and free of bulk defects) graphene. Such samples, however, are only relevant to fundamental UHV studies, and there are no available contact angles for a comparative analysis. Samples which were exposed to air and underwent a transfer step (graphene on copper and SiO₂), on the other hand, are widely used and studied, but have structural defects and contamination, especially for graphene on SiO₂.

Overall, surface science methods allow probing the interactions between graphene and individual molecules in ultra-pure environment and determination of the energy of desorption (which characterizes the strength of the interactions) and kinetic order of desorption (indicates how the molecules pack on the graphene surface). However, correlating the interaction parameters of individual molecules in UHV with the macroscopic wettability of graphene in ambient atmosphere is not straightforward. As well as in the case of macroscopic measurements, inconsistencies associated with the sample preparation pose a real challenge for the interpretation and the comparison between different sets of data, especially between microscopic (samples are prepared in UHV) and macroscopic (samples are exposed to air) studies. A systematic comparative analysis, which takes into consideration the effect of the sample preparation, is, therefore, needed.

In order to bridge the gap between the macroscopic and microscopic approaches, in Chapter 6 a comparative study was conducted on the effect of the irregularities in the graphene surface introduced during the transfer of graphene with the wettability both at a microscopic (water desorption measurements under UHV) and at the macroscopic level (contact angle measurements). Testing exactly the same samples in both TPD and contact angle measurements ensured the possibility to systematically compare the two approaches. Interestingly, the transparency of graphene to macroscopic wetting does not necessarily translate into the transparency to desorption of individual water molecules. While variations in roughness of the substrate seem to be of primary importance for the interactions between graphene and individual water molecules in vacuum, the

macroscopic wettability of graphene, in contrast, depends more strongly on the chemical composition of the substrate.

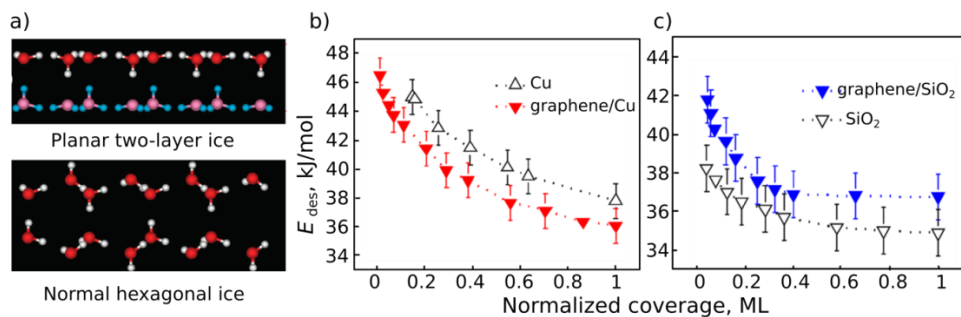


Figure 1.8. Molecular adsorption on graphene or microscopic wettability of graphene under UHV. a) Calculated structures (side view) of the planar two-layers polymorph of water ice that forms on graphene (top) and normal three-dimensional hexagonal water ice (bottom).¹⁰⁷ b) Desorption energy (E_{des}) as a function of benzene coverage (with ML depicting the number of benzene monolayers desorbed from the surface) for desorption of benzene from bare copper and graphene-on-copper.¹⁵⁰ c) Desorption energy (E_{des}) as a function of benzene coverage (ML – number of benzene monolayers desorbed from the surface) for desorption of benzene from bare SiO₂ and graphene-on-SiO₂.¹⁵⁰

1.5. Aim and outline

In this thesis unconventional tools based on fluidic interfaces were developed to study the surface and interfacial chemistry of graphene, to characterize the intrinsic properties of graphene, to disentangle the effects of substrate and of the environmental factors, and to improve handling protocols towards the preservation of the graphene cleanliness, morphology and electrical properties.

In Chapter 2 a liquid biphasic system was developed to transfer graphene without using a polymer support. Additionally, by probing electrically graphene *in situ* at a water/cyclohexane interface, an enhancement of charge carrier mobilities compared to supported graphene was observed, which was the first indication of the benefit of using a liquid interface to preserve the properties of pristine graphene.

Chapter 3 demonstrates how confocal Raman spectroscopy can be used to study graphene at a liquid/air and liquid/liquid interface, and presented a correlation study of graphene Raman bands. The results demonstrated that, unlike solid substrates, liquids do not induce strain and doping in graphene and are ideal supports for preserving the intrinsic electronic properties of graphene.

Chapter 4 further exemplifies how a liquid support can be used to probe the wettability of free-standing graphene revealing that graphene is inherently mildly hydrophilic.

Chapter 5 introduces ice and hydrogels as alternative supports for studying graphene-water interactions. The results show that graphene is hydrophilic in water and fully transparent to water-water interactions. Additionally, the selective transmittance of polar and dispersive interactions through graphene layer was investigated. Interestingly, while being fully transparent to dispersive interactions, graphene screens polar interactions in the samples that underwent a transfer step, presumably due to the structural distortions in the graphene layer induced by the transfer.

Finally, in Chapter 6 the macroscopic wettability in ambient atmosphere and the microscopic wettability under UHV conditions were systematically compared. The analysis showed that, while providing insights into the fundamental parameters

of graphene-water interactions, the microscopic wettability cannot characterize the macroscopic wettability of graphene. Additionally, the roughness of the underlying substrate was shown to affect the microscopic wettability and wetting transparency of graphene in UHV.

The use of liquid interfaces in graphene research is now emerging, and this thesis shows that the structural adaptability, molecular smoothness and weaker (compared to solids) intermolecular bonding of fluidic interfaces allow for experimental designs radically different from those involving solid substrates. By demonstrating that fluidic interfaces preserve graphene clean, smooth, unstrained and undoped, and by exploiting these advantages, a step forward was made to the design of (more) accessible and efficient graphene-based devices and technologies.

1.6. References

1. K. S. Novoselov, S. V. Morozov, D. Jiang, Y. Zhang, S. V. Dubonos, I. V. Grigorieva, A. A. Firsov, A. K. G. Electric field effect in atomically thin carbon films. *Science* **306**, 666–669 (2004).
2. Castro Neto, A. H., Guinea, F., Peres, N. M. R., Novoselov, K. S. & Geim, A. K. The electronic properties of graphene. *Rev. Mod. Phys.* **81**, 109–162 (2009).
3. Jorio, A., Dresselhaus, G. & Dresselhaus, M. S. *Carbon nanotubes: advanced topics in the synthesis, structure, properties and applications*. (Springer Berlin Heidelberg, 2007).
4. Geim, A. K. & Novoselov, K. S. The rise of graphene. *Nat. Mater.* **6**, 183–191 (2007).
5. Novoselov, K. S. *et al.* Two-dimensional gas of massless Dirac fermions in graphene. *Nature* **438**, 197–200 (2005).
6. Gusynin, V. P. & Sharapov, S. G. Unconventional integer quantum Hall effect in graphene. *Phys. Rev. Lett.* **95**, 146801 (2005).
7. Novoselov, K. S. *et al.* Room-temperature quantum Hall effect in graphene. *Science* **315**, 1379–1379 (2007).
8. Lee, C., Wei, X., Kysar, J. W. & Hone, J. Measurement of the elastic properties and intrinsic strength of monolayer graphene. *Science* **321**, 385–388 (2008).
9. Meyer, J. C. *et al.* The structure of suspended graphene sheets. *Nature* **446**, 60–63 (2007).
10. Fasolino, A., Los, J. H. & Katsnelson, M. I. Intrinsic ripples in graphene. *Nat. Mater.* **6**, 858–861 (2007).
11. Carlsson, J. M. Buckle or break. *Nat. Mater.* **6**, 801–802 (2007).
12. Nair, R. R. *et al.* Fine structure constant defines visual transparency of graphene. *Science* **320**, 1308 (2008).
13. Kuzmenko, A. B., van Heumen, E., Carbone, F. & van der Marel, D. Universal optical conductance of graphite. *Phys. Rev. Lett.* **100**, 117401

(2008).

14. Faugeras, C. *et al.* Thermal conductivity of graphene in Corbino membrane geometry. *ACS Nano* **4**, 1889–1892 (2010).
15. Cai, W. *et al.* Thermal transport in suspended and supported monolayer graphene grown by chemical vapor deposition. *Nano Lett.* **10**, 1645–1651 (2010).
16. Seo, D. H. *et al.* Anti-fouling graphene-based membranes for effective water desalination. *Nat. Commun.* **9**, 683 (2018).
17. Singh, E., Meyyappan, M. & Nalwa, H. S. Flexible graphene-based wearable gas and chemical sensors. *ACS Appl. Mater. Interfaces* **9**, 34544–34586 (2017).
18. Lemme, M. C., Echtermeyer, T. J., Baus, M. & Kurz, H. A Graphene field-effect device. *IEEE Electron Device Lett.* **28**, 282–284 (2007).
19. Matyba, P., Yamaguchi, H., Eda, G., Chhowalla, M., Edman, L. y Robinson, N. D. Graphene and mobile ions: the key to all plastic, solution processed light emitting devices. *ACS Nano* **4**, 637–642 (2010).
20. Schedin, F. *et al.* Detection of individual gas molecules adsorbed on graphene. *Nat. Mater.* **6**, 652–655 (2007).
21. Arjmandi-Tash, H., Belyaeva, L. A. & Schneider, G. F. Single molecule detection with graphene and other two-dimensional materials: nanopores and beyond. *Chem. Soc. Rev.* **45**, 476–493 (2016).
22. Heerema, S. J. & Dekker, C. Graphene nanodevices for DNA sequencing. *Nat. Nanotechnol.* **11**, 127–136 (2016).
23. Du, E. Y. A. and G. L. and X. Electronic properties of graphene: a perspective from scanning tunneling microscopy and magnetotransport. *Reports Prog. Phys.* **75**, 56501 (2012).
24. Novoselov, K. S. *et al.* Two-dimensional gas of massless Dirac fermions in graphene. *Nature* **438**, 197–200 (2005).
25. Novoselov, K. S. *et al.* Unconventional quantum Hall effect and Berry's phase of 2π in bilayer graphene. *Nat. Phys.* **2**, 177–180 (2006).
26. Katsnelson, M. I., Novoselov, K. S. & Geim, A. K. Chiral tunnelling and the

- Klein paradox in graphene. *Nat. Phys.* **2**, 620–625 (2006).
27. Pisana, S. *et al.* Breakdown of the adiabatic Born–Oppenheimer approximation in graphene. *Nat. Mater.* **6**, 198–201 (2007).
 28. Yu, Q. *et al.* Graphene segregated on Ni surfaces and transferred to insulators. *Appl. Phys. Lett.* **93**, 113103 (2008).
 29. Arco, L. G. De, Zhang, Y., Kumar, A. & Zhou, C. Synthesis, transfer, and devices of single- and few-layer graphene by chemical vapor deposition. *IEEE Trans. Nanotechnol.* **8**, 135–138 (2009).
 30. Reina, A. *et al.* Large area, few-layer graphene films on arbitrary substrates by chemical vapor deposition. *Nano Lett.* **9**, 30–35 (2009).
 31. Kim, K. S. *et al.* Large-scale pattern growth of graphene films for stretchable transparent electrodes. *Nature* **457**, 706–710 (2009).
 32. Li, X. *et al.* Large-area synthesis of high-quality and uniform graphene films on copper foils. *Science* **324**, 1312–1314 (2009).
 33. Zhang, Y., Zhang, L. & Zhou, C. Review of chemical vapor deposition of graphene and related applications. *Acc. Chem. Res.* **46**, 2329–2339 (2013).
 34. Lee, H. C. *et al.* Synthesis of single-layer graphene: a review of recent development. *Procedia Chem.* **19**, 916–921 (2016).
 35. Chen, G., Wu, D., Weng, W. & Wu, C. Exfoliation of graphite flake and its nanocomposites. *Carbon N. Y.* **41**, 619–621 (2003).
 36. Dreyer, D. R., Park, S., Bielawski, C. W. & Ruoff, R. S. The chemistry of graphene oxide. *Chem. Soc. Rev.* **39**, 228–240 (2010).
 37. Zhan, D. *et al.* FeCl₃-based few-layer graphene intercalation compounds: single linear dispersion electronic band structure and strong charge transfer doping. *Adv. Funct. Mater.* **20**, 3504–3509 (2010).
 38. Emtsev, K. V. *et al.* Towards wafer-size graphene layers by atmospheric pressure graphitization of silicon carbide. *Nat. Mater.* **8**, 203–207 (2009).
 39. Dötz, F., Brand, J. D., Ito, S., Gherghel, L. & Müllen, K. Synthesis of large polycyclic aromatic hydrocarbons: variation of size and periphery. *J. Am. Chem. Soc.* **122**, 7707–7717 (2000).

40. Segawa, Y., Ito, H. & Itami, K. Structurally uniform and atomically precise carbon nanostructures. *Nat. Rev. Mater.* **1**, 15002 (2016).
41. Hernandez, Y. *et al.* High-yield production of graphene by liquid-phase exfoliation of graphite. *Nat. Nanotechnol.* **3**, 563–568 (2008).
42. Choucair, M., Thordarson, P. & Stride, J. A. Gram-scale production of graphene based on solvothermal synthesis and sonication. *Nat. Nanotechnol.* **4**, 30–33 (2008).
43. Jiao, L., Zhang, L., Wang, X., Diankov, G. & Dai, H. Narrow graphene nanoribbons from carbon nanotubes. *Nature* **458**, 877–880 (2009).
44. Kosynkin, D. V *et al.* Longitudinal unzipping of carbon nanotubes to form graphene nanoribbons. *Nature* **458**, 872–876 (2009).
45. Shams, S. S., Zhang, R. & Zhu, J. Graphene synthesis: A Review. *Mater. Sci.* **33**, 566–578 (2015).
46. Kauling, A. P. *et al.* The worldwide graphene flake production. *Adv. Mater.* **0**, 1803784 (2018).
47. Li, X. *et al.* Large area synthesis of high quality and uniform graphene films on copper foils. *Science* **324**, 1312–1314 (2009).
48. Robertson, A. W. & Warner, J. H. Hexagonal single crystal domains of few-layer graphene on copper foils. *Nano Lett.* **11**, 1182–1189 (2011).
49. Xu, X. *et al.* Ultrafast epitaxial growth of metre-sized single-crystal graphene on industrial Cu foil. *Sci. Bull.* **62**, 1074–1080 (2017).
50. Banszerus, L. *et al.* Ultrahigh-mobility graphene devices from chemical vapor deposition on reusable copper. *Sci. Adv.* **1**, e1500222 (2015).
51. Petrone, N. *et al.* Chemical vapor deposition-derived graphene with electrical performance of exfoliated graphene. *Nano Lett.* **12**, 2751–2756 (2012).
52. Chen, X., Zhang, L. & Chen, S. Large area CVD growth of graphene. *Synth. Met.* **210**, 95–108 (2015).
53. Wang, R. *et al.* Investigation of CVD graphene topography and surface electrical properties. *Surf. Topogr. Metrol. Prop.* **4**, 25001 (2016).

54. Suk, J. W. *et al.* Transfer of CVD-grown monolayer graphene onto arbitrary substrates. *ACS Nano* **5**, 6916–6924 (2011).
55. Li, X. *et al.* Transfer of large-area graphene films for high-performance transparent conductive electrodes. *Nano Lett.* **9**, 4359–4363 (2009).
56. Gao, L. *et al.* Face-to-face transfer of wafer-scale graphene films. *Nature* **505**, 190–194 (2013).
57. Chen, M., Haddon, R. C., Yan, R. & Bekyarova, E. Advances in transferring chemical vapour deposition graphene: a review. *Mater. Horizons* **4**, 1054–1063 (2017).
58. Ishigami, M., Chen, J. H., Cullen, W. G., Fuhrer, M. S. & Williams, E. D. Atomic structure of graphene on SiO₂. *Nano Lett.* **7**, 1643–1648 (2007).
59. Suk, J. W. *et al.* Enhancement of the electrical properties of graphene grown by chemical vapor deposition via controlling the effects of polymer residue. *Nano Lett.* **13**, 1462–1467 (2013).
60. Pettes, M. T., Jo, I., Yao, Z. & Shi, L. Influence of polymeric residue on the thermal conductivity of suspended bilayer graphene. *Nano Lett.* **11**, 1195–1200 (2011).
61. Chen, J.-H., Jang, C., Xiao, S., Ishigami, M. & Fuhrer, M. S. Intrinsic and extrinsic performance limits of graphene devices on SiO₂. *Nat. Nanotechnol.* **3**, 206–209 (2008).
62. Chen, J.-H. *et al.* Charged-impurity scattering in graphene. *Nat. Phys.* **4**, 377–381 (2008).
63. Pirkle, A. *et al.* The effect of chemical residues on the physical and electrical properties of chemical vapor deposited graphene transferred to SiO₂. *Appl. Phys. Lett.* **99**, 122108 (2011).
64. Ryu, S. *et al.* Atmospheric oxygen binding and hole doping in deformed graphene on a SiO₂ substrate. *Nano Lett.* **10**, 4944–4951 (2010).
65. Arjmandi-Tash, H., Jiang, L. & Schneider, G. F. Rupture index: A quantitative measure of sub-micrometer cracks in graphene. *Carbon N. Y.* **118**, 556–560 (2017).
66. Lin, W.-H. *et al.* A direct and polymer-free method for transferring graphene grown by chemical vapor deposition to any substrate. *ACS Nano*

- 8**, 1784–1791 (2014).
67. Zhang, G. *et al.* Versatile polymer-free graphene transfer method and applications. *ACS Appl. Mater. Interfaces* **8**, 8008–8016 (2016).
 68. Park, H. *et al.* Polymer-free graphene transfer for enhanced reliability of graphene field-effect transistors. *2D Mater.* **3**, 21003 (2016).
 69. Pasternak, I. *et al.* Graphene films transfer using marker-frame method. *AIP Adv.* **4**, 97133 (2014).
 70. Lima, L. M. C., Arjmandi-Tash, H. & Schneider, G. F. Lateral non-covalent clamping of graphene at the edges using a lipid scaffold. *ACS Appl. Mater. Interfaces* **10**, 11328–11332 (2018).
 71. Bekyarova, M. C. and D. S. and W. L. and B. A. and R. C. H. and E. Sublimation-assisted graphene transfer technique based on small polyaromatic hydrocarbons. *Nanotechnology* **28**, 255701 (2017).
 72. Matruglio, A. *et al.* Contamination-free suspended graphene structures by a Ti-based transfer method. *Carbon N. Y.* **103**, 305–310 (2016).
 73. Ondarçuhu, T. *et al.* Wettability of partially suspended graphene. *Sci. Rep.* **6**, 24237 (2016).
 74. Geim, A. K. & Grigorieva, I. V. Van der Waals heterostructures. *Nature* **499**, 419–425 (2013).
 75. Guinea, F., Katsnelson, M. I. & Geim, A. K. Energy gaps and a zero-field quantum Hall effect in graphene by strain engineering. *Nat. Phys.* **6**, 30–33 (2009).
 76. Pereira, V. M. & Castro Neto, A. H. Strain engineering of graphene's electronic structure. *Phys. Rev. Lett.* **103**, 46801 (2009).
 77. Bao, W. *et al.* Controlled ripple texturing of suspended graphene and ultrathin graphite membranes. *Nat. Nanotechnol.* **4**, 562–566 (2009).
 78. Wang, Y. Y. *et al.* Raman studies of monolayer graphene: the substrate effect. *J. Phys. Chem. C* **112**, 10637–10640 (2008).
 79. Lee, J. E., Ahn, G., Shim, J., Lee, Y. S. & Ryu, S. Optical separation of mechanical strain from charge doping in graphene. *Nat. Commun.* **3**, 1024 (2012).

80. Bendiab, N. *et al.* Unravelling external perturbation effects on the optical phonon response of graphene. *J. Raman Spectrosc.* **49**, 130–145 (2018).
81. Shioya, H., Russo, S., Yamamoto, M., Craciun, M. F. & Tarucha, S. Electron states of uniaxially strained graphene. *Nano Lett.* **15**, 7943–7948 (2015).
82. Bao, W. *et al.* Controlled ripple texturing of suspended graphene and ultrathin graphite membranes. *Nat. Nanotechnol.* **4**, 562–566 (2009).
83. Yoon, D., Son, Y.-W. & Cheong, H. Negative thermal expansion coefficient of graphene measured by Raman spectroscopy. *Nano Lett.* **11**, 3227–3231 (2011).
84. Lee, Y. R., Huang, J. X., Lin, J. C. & Lee, J. R. Study of the substrate-induced strain of as-grown graphene on Cu(100) using temperature-dependent Raman spectroscopy: estimating the mode Grüneisen parameter with temperature. *J. Phys. Chem. C* **121**, 27427–27436 (2017).
85. Casiraghi, C., Pisana, S., Novoselov, K. S., Geim, A. K. & Ferrari, A. C. Raman fingerprint of charged impurities in graphene. *Appl. Phys. Lett.* **91**, 233108 (2007).
86. Parobek, D. & Liu, H. Wettability of graphene. *2D Mater.* **2**, 32001 (2015).
87. de Gennes, P. G. Wetting: statics and dynamics. *Rev. Mod. Phys.* **57**, 827–863 (1985).
88. Bonn, D., Eggers, J., Indekeu, J., Meunier, J. & Rolley, E. Wetting and spreading. *Rev. Mod. Phys.* **81**, 739–805 (2009).
89. Leenaerts, O., Partoens, B. & Peeters, F. M. Water on graphene: Hydrophobicity and dipole moment using density functional theory. *Phys. Rev. B* **79**, 235440 (2009).
90. Bera, B. *et al.* Wetting of water on graphene nanopowders of different thicknesses. *Appl. Phys. Lett.* **112**, 1–6 (2018).
91. Taherian, F., Marcon, V., Van Der Vegt, N. F. A. & Leroy, F. What is the contact angle of water on graphene? *Langmuir* **29**, 1457–1465 (2013).
92. Raj, R., Maroo, S. C. & Wang, E. N. Wettability of graphene. *Nano Lett.* **13**, 1509–1515 (2013).
93. Rafiee, J. *et al.* Wetting transparency of graphene. *Nat. Mater.* **11**, 217–

222 (2012).

94. Driskill, J., Vanzo, D., Bratko, D. & Luzar, A. Wetting transparency of graphene in water. *J. Chem. Phys.* **141**, 18C517 (2014).
95. Shih, C. J. *et al.* Breakdown in the wetting transparency of graphene. *Phys. Rev. Lett.* **109**, 176101 (2012).
96. Du, F., Huang, J., Duan, H., Xiong, C. & Wang, J. Wetting transparency of supported graphene is regulated by polarities of liquids and substrates. *Appl. Surf. Sci.* **454**, 249–255 (2018).
97. Wang, Q. H. *et al.* Understanding and controlling the substrate effect on graphene electron-transfer chemistry via reactivity imprint lithography. *Nat. Chem.* **4**, 724–732 (2012).
98. Kozbial, A. *et al.* Study on the surface energy of graphene by contact angle measurements. *Langmuir* **30**, 8598–606 (2014).
99. Kim, D., Pugno, N. M., Buehler, M. J. & Ryu, S. Solving the controversy on the wetting transparency of graphene. *Sci. Rep.* **5**, 15526 (2015).
100. Shin, Y. J. *et al.* Surface-energy engineering of graphene. *Langmuir* **26**, 3798–3802 (2010).
101. Liu, J., Lai, C.-Y., Zhang, Y.-Y., Chiesa, M. & Pantelides, S. T. Water wettability of graphene: interplay between the interfacial water structure and the electronic structure. *RSC Adv.* **8**, 16918–16926 (2018).
102. Hong, G. *et al.* On the mechanism of hydrophilicity of graphene. *Nano Lett.* **16**, 4447–4453 (2016).
103. Ashraf, A. *et al.* Doping-induced tunable wettability and adhesion of graphene. *Nano Lett.* **16**, 4708–4712 (2016).
104. Shams, S. S., Zhang, R. & Zhu, J. Graphene synthesis: A Review. *Mater. Sci.* **33**, 566–578 (2015).
105. Lee, H. C. *et al.* Review of the synthesis, transfer, characterization and growth mechanisms of single and multilayer graphene. *RSC Adv.* **7**, 15644–15693 (2017).
106. Li, Z. *et al.* Effect of airborne contaminants on the wettability of supported graphene and graphite. *Nat. Mater.* **12**, 925–931 (2013).

107. Kimmel, G. A. *et al.* No confinement needed: observation of a metastable hydrophobic wetting two-layer ice on graphene. *J. Am. Chem. Soc.* **131**, 12838–12844 (2009).
108. Chakradhar, A., Trettel, K. & Burghaus, U. Benzene adsorption on Ru(0001) and graphene/Ru(0001)—How to synthesize epitaxial graphene without STM or LEED? *Chem. Phys. Lett.* **590**, 146–152 (2013).
109. Smith, R. S., Matthiesen, J. & Kay, B. D. Desorption kinetics of methanol, ethanol, and water from graphene. *J. Phys. Chem. A* **118**, 8242–8250 (2014).
110. Chakradhar, A. & Burghaus, U. Adsorption of water on graphene/Ru(0001)—an experimental ultra-high vacuum study. *Chem. Commun.* **50**, 7698–7701 (2014).
111. Smith, R. S., May, R. A. & Kay, B. D. Desorption kinetics of Ar, Kr, Xe, N₂, O₂, CO, methane, ethane, and propane from graphene and amorphous solid water surfaces. *J. Phys. Chem. B* **120**, 1979–1987 (2016).
112. Smith, R. S. & Kay, B. D. Desorption kinetics of benzene and cyclohexane from a graphene surface. *J. Phys. Chem. B* **122**, 587–594 (2018).
113. Sivapragasam, N., Nayakasinghe, M. T., Chakradhar, A. & Burghaus, U. Effects of the support on the desorption kinetics of n-pentane from graphene: an ultrahigh vacuum adsorption study. *J. Vac. Sci. Technol. A* **35**, 61404 (2017).
114. Wang, S., Zhang, Y., Abidi, N. & Cabrales, L. Wettability and surface free energy of graphene films. *Langmuir* **25**, 11078–11081 (2009).
115. van Engers, C. D. *et al.* Direct measurement of the surface energy of graphene. *Nano Lett.* **17**, 3815–3821 (2017).
116. Su, R. & Zhang, X. Wettability and surface free energy analyses of monolayer graphene. *J. Therm. Sci.* **27**, 359–363 (2018).
117. Spanu, L., Sorella, S. & Galli, G. Nature and strength of interlayer binding in graphite. *Phys. Rev. Lett.* **103**, 196401 (2009).
118. Björkman, T., Gulans, A., Krasheninnikov, A. V & Nieminen, R. M. van der Waals bonding in layered compounds from advanced density-functional first-principles calculations. *Phys. Rev. Lett.* **108**, 235502 (2012).

119. Van Oss, C. J., Roberts, M. J., Good, R. J. & Chaudhury, M. K. Determination of the apolar component of the surface tension of water by contact angle measurements on gels. *Colloids and Surfaces* **23**, 369–373 (1987).
120. Fowkes, F. M. Attractive forces at interfaces. *Ind. Eng. Chem.* **56**, 40–52 (1964).
121. Owens, D. K. & Wendt, R. C. Estimation of the surface free energy of polymers. *J. Appl. Polym. Sci.* **13**, 1741–1747 (1969).
122. Li, D. & Neumann, A. W. Contact angles on hydrophobic solid surfaces and their interpretation. *J. Colloid Interface Sci.* **148**, 190–200 (1992).
123. Li, D. & Neumann, A. W. Equilibrium of capillary systems with an elastic liquid-vapor interface. *Langmuir* **9**, 50–54 (1993).
124. Neumann, A. W., Good, R. J., Hope, C. J. & Sejpal, M. An equation-of-state approach to determine surface tensions of low-energy solids from contact angles. *J. Colloid Interface Sci.* **49**, 291–304 (1974).
125. Annamalai, M. *et al.* Surface energy and wettability of van der Waals structures. *Nanoscale* **8**, 5764–5770 (2016).
126. Andrews, J. E., Wang, Y., Sinha, S., Chung, P. W. & Das, S. Roughness-induced chemical heterogeneity leads to large hydrophobicity in wetting-translucent nanostructures. *Nano Lett.* **19**, 27421–27434 (2018).
127. Scocchi, G., Sergi, D., D’Angelo, C. & Ortona, A. Wetting and contact-line effects for spherical and cylindrical droplets on graphene layers: a comparative molecular-dynamics investigation. *Phys. Rev. E* **84**, 61602 (2011).
128. Andrews, J. E., Sinha, S., Chung, P. W. & Das, S. Wetting dynamics of a water nanodrop on graphene. *Phys. Chem. Chem. Phys.* **18**, 23482–23493 (2016).
129. Yiapanis, G., Makarucha, A. J., Baldauf, J. S. & Downton, M. T. Simulations of graphitic nanoparticles at air-water interfaces. *Nanoscale* **8**, 19620–19628 (2016).
130. Schrader, M. E. Ultrahigh vacuum techniques in the measurement of contact angles. IV. Water on graphite (0001). *J. Phys. Chem.* **79**, 2508–

- 2515 (1975).
131. Martinez-Martin, D. *et al.* Atmospheric contaminants on graphitic surfaces. *Carbon N. Y.* **61**, 33–39 (2013).
 132. Wehling, T. O., Lichtenstein, A. I. & Katsnelson, M. I. First-principles studies of water adsorption on graphene: the role of the substrate. *Appl. Phys. Lett.* **93**, 202110 (2008).
 133. Sengupta, S., Nichols, N. S., Del Maestro, A. & Kotov, V. N. Theory of liquid film growth and wetting instabilities on graphene. *Phys. Rev. Lett.* **120**, 236802 (2018).
 134. Ashraf, A. *et al.* Spectroscopic investigation of the wettability of multilayer graphene using highly ordered pyrolytic graphite as a model material. *Langmuir* **30**, 12827–12836 (2014).
 135. Amadei, C. A., Lai, C.-Y., Heskes, D. & Chiesa, M. Time dependent wettability of graphite upon ambient exposure: The role of water adsorption. *J. Chem. Phys.* **141**, 84709 (2014).
 136. Lai, C.-Y. *et al.* A nanoscopic approach to studying evolution in graphene wettability. *Carbon N. Y.* **80**, 784–792 (2014).
 137. Aria, A. I. *et al.* Time evolution of the wettability of supported graphene under ambient air exposure. *J. Phys. Chem. C* **120**, 2215–2224 (2016).
 138. Kozbial, A. *et al.* Understanding the intrinsic water wettability of graphite. *Carbon N. Y.* **74**, 218–225 (2014).
 139. Cunge, G. *et al.* Dry efficient cleaning of poly-methyl-methacrylate residues from graphene with high-density H₂ and H₂-N₂ plasmas. *J. Appl. Phys.* **118**, 123302 (2015).
 140. Li, Z. *et al.* Water protects graphitic surface from airborne hydrocarbon contamination. *ACS Nano* **10**, 349–359 (2016).
 141. Xue, R., Abidi, I. & Luo, Z. Domain size, layer number and morphology control for graphene grown by chemical vapor deposition. *Funct. Mater. Lett.* **10**, 1730003 (2017).
 142. Feng, X., Maier, S. & Salmeron, M. Water splits epitaxial graphene and intercalates. *J. Am. Chem. Soc.* **134**, 5662–5668 (2012).

143. Wang, Y., Sinha, S., Hu, L. & Das, S. Interaction between a water drop and holey graphene: retarded imbibition and generation of novel water-graphene wetting states. *Nano Lett.* **5**, 3815–3821 (2017).
144. Hallam, T., Berner, N. C., Yim, C. & Duesberg, G. S. Strain, bubbles, dirt, and folds: a study of graphene polymer-assisted transfer. *Adv. Mater. Interfaces* **1**, 1400115 (2014).
145. Belyaeva, L. A., van Deursen, P. M. G., Barbetsea, K. I. & Schneider, G. F. Hydrophilicity of graphene in water through transparency to polar and dispersive interactions. *Adv. Mater.* **30**, 1–7 (2018).
146. Su, Y. *et al.* Polymer adsorption on graphite and CVD graphene surfaces studied by surface-specific vibrational spectroscopy. *Nano Lett.* **15**, 6501–6505 (2015).
147. Han, Y. *et al.* Clean surface transfer of graphene films via an effective sandwich method for organic light-emitting diode applications. *J. Mater. Chem. C* **2**, 201–207 (2014).
148. Kumar, K., Kim, Y.-S. & Yang, E.-H. The influence of thermal annealing to remove polymeric residue on the electronic doping and morphological characteristics of graphene. *Carbon N. Y.* **65**, 35–45 (2013).
149. Chakradhar, A., Sivapragasam, N., Nayakasinghe, M. T. & Burghaus, U. Support effects in the adsorption of water on CVD graphene: an ultra-high vacuum adsorption study. *Chem. Commun.* **51**, 11463–11466 (2015).
150. Chakradhar, A., Sivapragasam, N., Nayakasinghe, M. T. & Burghaus, U. Adsorption kinetics of benzene on graphene: an ultrahigh vacuum study. *J. Vac. Sci. Technol. A Vacuum, Surfaces, Film.* **34**, 21402 (2016).
151. Sivapragasam, N., Nayakasinghe, M. T. & Burghaus, U. Adsorption of n-butane on graphene/Ru(0001)—a molecular beam scattering study. *J. Vac. Sci. Technol. A* **34**, 41404 (2016).
152. King, D. A. Thermal desorption from metal surfaces: A review. *Surf. Sci.* **47**, 384–402 (1975).
153. Ceyer, S. T. New mechanisms for chemistry at surfaces. *Science* **249**, 133–139 (1990).
154. Ulbricht, H., Zacharia, R., Cindir, N. & Hertel, T. Thermal desorption of

- gases and solvents from graphite and carbon nanotube surfaces. *Carbon N. Y.* **44**, 2931–2942 (2006).
155. Zangi, R. Water confined to a slab geometry: a review of recent computer simulation studies. *J. Phys. Condens. Matter* **16**, S5371 (2004).
 156. Giovambattista, N., Rosky, P. J. & Debenedetti, P. G. Phase transitions induced by nanoconfinement in liquid water. *Phys. Rev. Lett.* **102**, 50603 (2009).
 157. Daschbach, J. L., Peden, B. M., Smith, R. S. & Kay, B. D. Adsorption, desorption, and clustering of H₂O on Pt(111). *J. Chem. Phys.* **120**, 1516–1523 (2004).
 158. Ulbricht, H., Zacharia, R., Cindir, N. & Hertel, T. Thermal desorption of gases and solvents from graphite and carbon nanotube surfaces. *Carbon N. Y.* **44**, 2931–2942 (2006).
 159. Brown, W. A. & Bolina, A. S. Fundamental data on the desorption of pure interstellar ices. *Mon. Not. R. Astron. Soc.* **374**, 1006–1014 (2007).
 160. Bolina, A. S., Wolff, A. J. & Brown, W. A. Reflection absorption infrared spectroscopy and temperature-programmed desorption studies of the adsorption and desorption of amorphous and crystalline water on a graphite surface. *J. Phys. Chem. B* **109**, 16836–16845 (2005).

CHAPTER 2

Molecular caging of graphene with cyclohexane: transfer and electrical transport

Transfer of large, clean, crack- and fold-free graphene sheets is a critical challenge in the field of graphene-based electronic devices. Polymers, conventionally used to transfer two-dimensional materials irreversibly adsorb on their surface yielding a range of unwanted chemical functions and contaminations. An oil-water interface represents an ideal support for graphene. Cyclohexane, the oil phase, protects graphene from mechanical deformation and minimizes vibrations of the water surface. Remarkably, cyclohexane solidifies at 7°C forming a plastic crystal phase molecularly conforming graphene, preventing the use of polymers, and thus drastically limiting contamination. Graphene floating at the cyclohexane/water interface exhibits improved electrical performances allowing for new possibilities of in situ, flexible sensor devices at a water interface.

This chapter was published as an article: Liubov A. Belyaeva, Wangyang Fu, Hadi Arjmandi Tash, and Grégory F. Schneider. ACS Cent. Sci., 2016, 2 (12), pp 904–909.

2.1. Introduction

For years now, long chain polymers are used to prevent cracking and to preserve the two-dimensional nature of graphene during transfer.¹⁻⁶ Because of their macromolecular structures, polymers can hardly be removed from the graphene surface:⁷⁻⁹ they irreversibly adsorb and modify the chemical and physical properties of graphene.^{10,11} Instead of using polymers, so-called polymer-free transfer techniques use special frames and holders to keep the sheet integrity of graphene.^{12,13} Very recently a biphasic system composed of an aqueous solution of ammonium persulfate and hexane has been employed to transfer clean graphene.¹⁴ Transfers not involving polymers, however, are widely known to induce cracks as graphene is a macroscopic sheet that has to be mechanically maintained while and after the underlying growth catalyst is etched. Polymers are known to protect graphene from cracking and folding at the cost of extensive contamination, highlighting the need for a top phase that can be solidified without the use of polymerization reactions. This chapter demonstrates that cyclohexane can operate similarly to a polymer support, however, without inducing major contamination on the graphene surface. The caging of graphene at a cyclohexane/water interface harvests nonpolar binding interactions between graphene and an organic liquid to maintain graphene flat, while still permitting the etching of the growth catalyst from the etchant bottom aqueous phase. Such organic-aqueous interfaces have been used for separating and extracting products of chemical reactions,^{15,16} and have the potential for *in situ* graphene functionalization^{17,18} and electrochemistry.^{19,20}

Here, the fluidic interface – that is two immiscible liquids with graphene in between – allows to mechanically and continuously relax graphene from stresses induced during etching, preventing the formation of the wrinkles always observed in conventional graphene transfers. In addition, the surface tension forces at the cyclohexane-water interface damp down low amplitude vibrations therefore preventing graphene from cracking, which always occur when graphene floats on the surface of water without a polymer support.

Cyclohexane was employed as the organic phase because of several important physical properties: i) cyclohexane is immiscible with water, ii) cyclohexane conforms the surface of graphene during copper etching at room temperature, and most importantly, iii) cyclohexane solidifies at 7°C forming a plastic crystal phase supporting graphene once the copper is etched. The soft gel-like structure of the plastic crystal phase of cyclohexane (this chapter only considers the high-temperature solid phase of cyclohexane, stable between -87°C and melting at 7°C, as shown in Figure 2.1a) conforms the surface of graphene preventing mechanical damaging with minimum contamination and handling, because only cooling down from room temperature to 0-7°C is needed to solidify the cyclohexane phase. After transfer to the final substrate, the residues of cyclohexane are easily removed by melting and evaporating cyclohexane at room temperature.

Such biphasic platform also yields intact graphene with high electrical performance as cyclohexane is chemically benign and completely removable from graphene: for the first time, probing the electric field-effect properties of graphene at the biphasic interface showed a charge carrier mobility reaching $\mu=3,470 \text{ cm}^2/\text{Vs}$, a value superior to — for example — the same batch of graphene transferred on a Si/SiO₂ ($\mu=2,180 \text{ cm}^2/\text{Vs}$) and epoxy substrates ($\mu=1,505 \text{ cm}^2/\text{Vs}$).

2.2. Results and Discussion

2.2.1. Interfacial caging of graphene: the concept

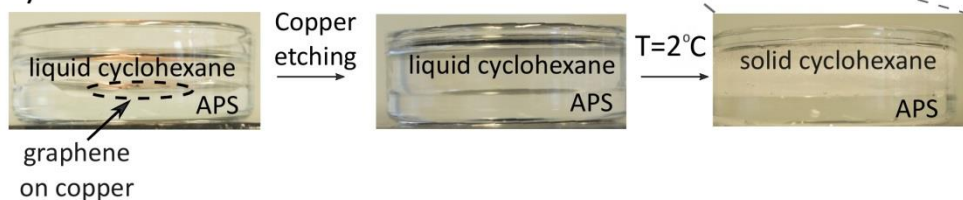
Water and cyclohexane are immiscible (solubility of cyclohexane in water is 0.006% at 25°C; solubility of water in cyclohexane is 0.01% at 20°C) and ammonium persulfate – the copper etchant – is insoluble in cyclohexane, minimizing the interchange of matter between the two phases. Once placed at the cyclohexane-air interface, the graphene/copper sample sinks to the cyclohexane/water interface and floats there exposing graphene to the cyclohexane phase and copper to the etchant solution (see Figure 2.1b and c).

Once the copper is completely etched graphene remains floating in between the two phases (Figure 2.1b). Water and cyclohexane apply pressure on both sides of graphene, and serve as a firm, but flexible shell conforming the surface of graphene.

a)



b)



c)

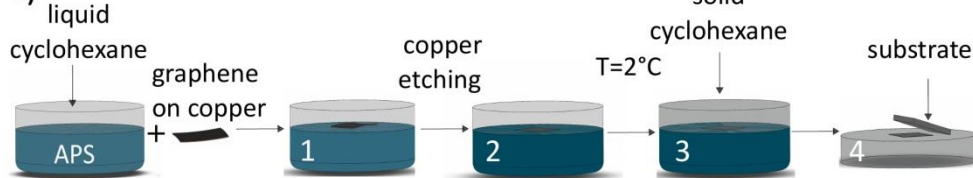


Figure 2.1. The cyclohexane and water interface for graphene caging and biphasic transfer. a) Temperature dependence of the state of matter for cyclohexane and water. In the temperature (T) range $-87^{\circ}\text{C} < T < 7^{\circ}\text{C}$ cyclohexane forms a plastic crystal phase, whereas water is liquid at temperatures above 0°C . b) Interfacial caging employed at temperatures above 0°C . Biphasic transfer is carried at temperatures between 0°C and 7°C in which cyclohexane is a plastic crystal and water is liquid. c) Illustration depicting the interfacial transfer process. Graphene on copper is placed in a biphasic mixture of water and cyclohexane at room temperature (1), the copper is etched using ammonium persulfate in water (2), the solution is then cooled down to 2°C until the cyclohexane phase solidifies (3), and the cyclohexane phase with graphene adsorbed is transferred onto a substrate (4). In a last step the sample is kept at 2°C until the cyclohexane sublimates completely from the solid to the gas phase.

2.2.2. Interfacial transfer process

After copper is etched, the biphasic oil-water mixture is cooled down to 2°C (Figure 2.1c). At 2°C cyclohexane solidifies and forms a solid mold on the top-side of the graphene surface. The solid cyclohexane phase with adsorbed graphene can be separated from the etchant and rinsed with cold water at 2°C to remove residues of etchant. The cyclohexane mold is then taken out and placed on the final substrate that has been preliminarily cooled down. The cyclohexane/graphene/substrate stack is then placed in an open container with constant temperature around 0-2°C (a box with water ice or ventilated fridge in our case). Cyclohexane kept at 2°C is volatile and sublimates gently in 15-90 minutes depending on the volume used, leaving graphene intact on the substrate. A volume ratio between the two phases of 1:1 was used, typically 10 mL of 0.5M APS in water and 10 mL of cyclohexane. Cyclohexane was then left to evaporate overnight at a temperature ranging from 0-4°C, typically in an ice-water bath or in a ventilated fridge.

An alternative is to directly deposit the substrate on the copper foil covered with graphene at the cyclohexane-water interface. Next, cyclohexane is solidified by cooling down the biphasic mixture to 0-2°C, and the solid cyclohexane phase with the incrustated substrate with graphene is taken out of the beaker. The fact that graphene was in contact with the substrate from the very start of the transfer prevents the presence of ammonium persulfate residues between graphene and the substrate. The APS salt residues on the other side of graphene can be removed by rinsing the sample with water. The rinsing has to be done slowly to maintain the 0-2°C as it can cause melting of cyclohexane and the detachment of graphene.

2.2.3. Crucial to freeze cyclohexane

To demonstrate the importance of freezing cyclohexane, three control transfer experiments were performed. First, cyclohexane was not frozen and the graphene floating at the interface was directly “fished-out”, that is contact-

stamped, using a silicon wafer. The turbulence occurring both in the cyclohexane phase and in the etchant phase due to the insertion of the wafer broke the graphene apart. In a second experiment, a wafer was placed on copper/graphene prior etching without freezing the cyclohexane. In both cases, no graphene was transferred to the substrate, which therefore, indicated that solidification of cyclohexane prior transferring graphene was an essential step. In a last experiment a silicon wafer was placed on copper/graphene floating on the etchant without using cyclohexane: again, no graphene was found on the wafer after the transfer.

2.2.4. Integrity and quality of graphene transferred using interfacial caging

The properties of graphene (continuity, density of cracks, size of wrinkles, density of wrinkles) transferred using interfacial caging were compared with: i) the most commonly used PMMA-based polymer-assisted transfer (Figure 2.2b),^{2,3} ii) the potentially most “clean” method, which is introduced here as “contact-stamping”, where graphene is transferred by pushing the substrate down into water towards a floating graphene flake, and iii) the hexane-assisted transfer (see Appendix 1 for more details).¹⁴ The PMMA polymer (i.e., poly(methylmethacrylate)) protects and conforms the surface of graphene and therefore allows transferring large and continuous areas of graphene (Figure 2.2b). Polymer residuals, however, are inevitable, contaminating the surface of graphene.¹¹ In contrast, contact-stamping and hexane-assisted transfer methods result in cleaner, but discontinuous graphene samples with multiple irregularities (foldings, wrinkles, cracks, etc., see Figure 2.2c-d). Interfacial caging, however, yields large and continuous graphene sheets if transferred onto Si/SiO₂ substrates (Figure 2.2a) with negligible folding and almost no micrometer-scale wrinkles.

The optical micrographs of graphene transferred with PMMA and interfacial caging are similar (Figure 2.2a versus Figure 2.2b). Among all the existing transfer methods, interfacial caging and the PMMA-assisted method showed least amounts of cracks (Figure 2.2a, b). Graphene transferred by contact stamping is less uniform (cracked) and has a higher density of wrinkles, even more evident on the magnified optical micrographs (Figure 2.2c, inset). Those wrinkles likely

originate from the moment when graphene floating on the etchant is brought in contact with the wafer during stamping. Contact stamping and hexane-assisted transfer methods yield similar graphene morphologies: when graphene is scooped out of the biphasic system, the graphene breaks into smaller pieces and therefore becomes largely wrinkled and cracked (Figure 2.2c and d).

The Raman spectra of graphene transferred on silicon wafers using the interfacial caging, the PMMA-assisted method and the contact stamping are similar, showing the characteristic peaks of monolayer graphene (Figure 2.2e, Table 2.1): a sharp 2D peak (I_{2D}/I_G ratio of 2.4 for interfacial caging, 1.4 for PMMA-assisted and 2 for contact stamping methods respectively; with a FWHM for the 2D peak of 30 cm^{-1}), fitting one Lorentz function indicating the presence of monolayer graphene,²¹ and a negligible D peak suggesting almost no defects in the graphene lattice (I_D/I_G ratio of 0.1 for interfacial caging and the PMMA-assisted transfer methods, and I_D/I_G ratio of 0.2 for contact stamping).²¹ These ratios indicate that the graphene transferred using interfacial caging has a defect density similar to the graphene samples transferred using PMMA and contact-stamping.

Table 2.1. Raman characteristics of graphene transferred by interfacial caging, PMMA-assisted and contact stamping transfer methods

	D peak position, cm^{-1}	G peak position, cm^{-1}	2D peak position, cm^{-1}	I_D/I_G	I_{2D}/I_G	FWHM, cm^{-1}
Interfacial caging	1343	1587	2686	0.1	2.4	30
PMMA-assisted	1345	1587	2687	0.1	1.4	26
Contact stamping	1343	1587	2687	0.2	2	33

Remarkably, if interfacial caging is used to fabricate suspended graphene areas ($\sim 2\ \mu\text{m}^2$) on a porous substrate, a full coverage is achieved in large scale. Figure 2.2f shows scanning electron micrographs images of the samples transferred using the interfacial caging on holey transmission electron microscope grids. Particularly, free-standing graphene membranes are free from wrinkles, tears and visible contamination (see Figure 2.2f).

Graphene transferred to quantifoil grids also showed no traces of cyclohexane, as shown by TEM in Figure 2.2g. Upon exposure to the electron beam of the TEM, contamination on the graphene surface accumulates quickly (in the course of 40 s) in the area exposed to the electron beam, and is seen as amorphization in the diffraction patterns of graphene.²² In contrast, our sample exhibited almost no change in diffraction patterns taken over 15 minutes, which indicates, that no noticeable contamination took place on graphene surface (Figure 2.2g).

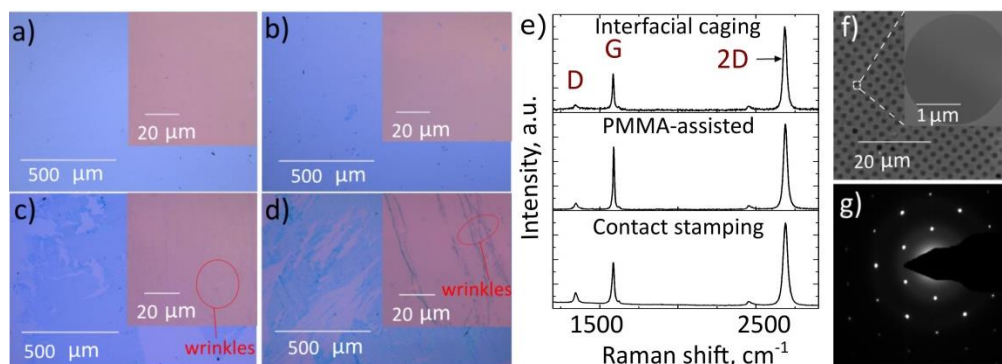


Figure 2.2. Comparison of the interfacial caging transfer with conventional transfer methods (PMMA-assisted, contact stamping, hexane-assisted). a) Optical micrograph of graphene transferred using interfacial caging with solidified cyclohexane. b) Optical micrograph of graphene transferred using the PMMA-assisted method. c) Optical micrograph of graphene transferred using contact stamping. d) Optical micrograph of graphene transferred using the hexane-assisted method.¹⁴ e) Raman spectra of graphene transferred onto silicon wafers using interfacial caging, PMMA-assisted and contact stamping. f) Scanning electron micrograph of graphene transferred to a quantifoil electron microscopy grid using interfacial caging. Inset: zoomed-in view of graphene free-standing on top of a hole on the grid – no contamination, cracks and folding's are visible. g) Diffraction pattern of graphene transferred with interfacial caging. TEM was carried with a 300kV electron beam focused to a 100 nm probe size, spot size 3, C_2 aperture of 20 mm on a FEI Titan.

Graphene transferred by interfacial caging (Figure 2.3a) was further studied using atomic force microscopy (AFM) and compared with the results obtained with conventional transfer methods (Figure 2.3b-d). A typical AFM image of graphene transferred to a silicon wafer using PMMA shows multiple features that

correspond to wrinkles, PMMA residues, dust particles and other topological features (Figure 2.3b).^{8,9,11} The wrinkles are denser and larger for PMMA transferred graphene (3-10 nm in height) than for interfacial caging (below 2 nm, see Figure 2.3a and 2.3b). Contact stamped graphene, as expected, exhibits repetitive patterns with parallel wrinkles (white lines with a length of a few micrometers and heights up to 10 nm, see Figure 2.3c), a result in agreement with the optical micrographs of the same samples (Figure 2.2c). The surface of the hexane-transferred graphene also contains wrinkles with heights of 2-5 nm, which are smaller than for contact stamped graphene, and larger than for the samples transferred using interfacial caging (Figure 2.3d). The large particles that are seen in all AFM images, for all three samples are dust particles and possibly copper etchant crystals/residuals. Those contaminants are very difficult to avoid when working under atmospheric conditions, and not in a cleanroom.

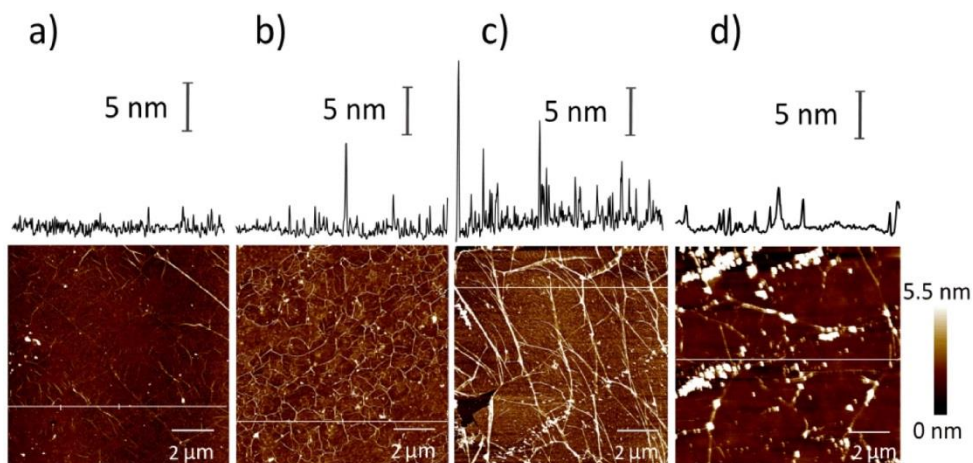


Figure 2.3. AFM images and height profiles of graphene samples transferred to a silicon wafer using interfacial caging and other conventional transfer methods. a) Interfacial caging method. b) PMMA-assisted method. c) Contact stamping method. d) Hexane-assisted transfer method.¹⁴ The top panel in each image shows the height profile along the line (in white) highlighted in the main image.

2.2.5. Biphasic electrolyte-gated graphene field-effect transistor

In order to confirm that the interfacial transfer procedure yields intact graphene with high electrical performance, the electric field-effect of graphene at the biphasic interface was examined. For the device fabrication, while graphene was

floating at the organic/water interface, the source and drain electrodes (25 μm thick copper) were protected by using PMMA against the etchant, leaving the upper surface available to electrically contact graphene after etching (Figure 2.4b, top) with needle electrodes. As a control, graphene devices on an epoxy substrate and on a Si/SiO₂ substrate were fabricated.²³ Ag/AgCl reference electrodes were used as the electrolyte gate. The conductance (G) versus gate voltage (V_{ref}) curves of graphene are shown in Figure 2.4a.

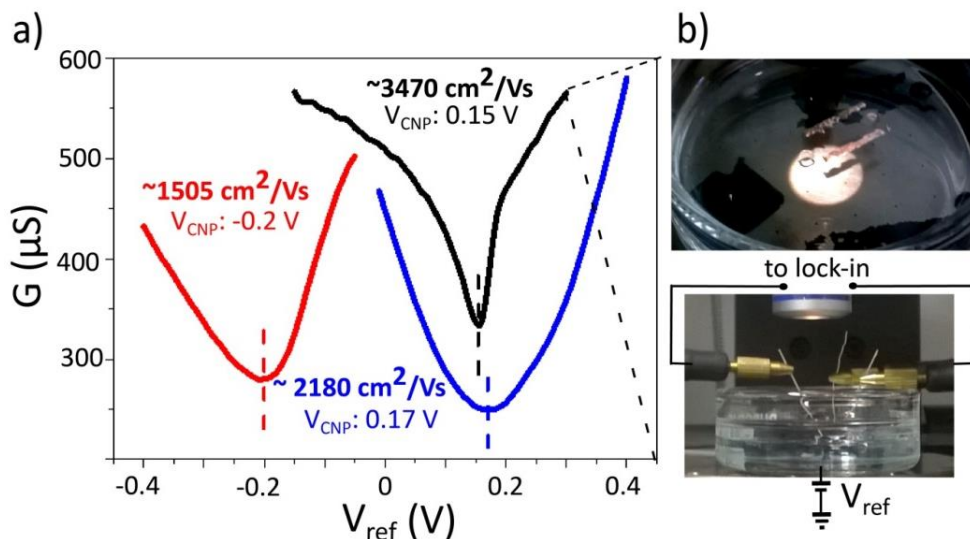


Figure 2.4. Electrical characterization of graphene at a cyclohexane/water interface. a) Electrolyte gate voltage (V_{ref}) dependent sheet conductance (G) of polymer-free graphene at a cyclohexane-water interface (black), on an epoxy substrate (red) and on a Si/SiO₂ substrate (blue). The gate voltage of the charge neutrality point V_{CNP} is 0.15 V for the graphene at the cyclohexane-water interface, -0.2 V on an epoxy substrate and 0.17 V for the graphene on Si/SiO₂. b) Photographs of the experimental setup used for probing the electronic properties of graphene at the water/cyclohexane interface: top-view (top) and side-view (bottom). As graphene floats at the organic/water interface, a bias voltage applied between the source and drain electrodes (V_{SD}) was applied between the two source and drain copper electrodes (25 μm thick Cu).

Significantly higher carrier mobility were measured for graphene floating at the water/cyclohexane interface ($\sim 3470 \text{ cm}^2/\text{Vs}$, $\sim 1940 \text{ cm}^2/\text{Vs}$ for holes and $\sim 5000 \text{ cm}^2/\text{Vs}$ for electrons; see Figure 2.4a), compared to $\sim 1505 \text{ cm}^2/\text{Vs}$ ($\sim 940 \text{ cm}^2/\text{Vs}$ for holes and $\sim 2070 \text{ cm}^2/\text{Vs}$ for electrons) on the epoxy substrate and $\sim 2180 \text{ cm}^2/\text{Vs}$ ($\sim 1840 \text{ cm}^2/\text{Vs}$ for holes and $\sim 2520 \text{ cm}^2/\text{Vs}$ for electrons) on the Si/SiO₂

substrate. Consequently, in the interfacial configuration the electrical properties of graphene are better than for graphene on substrates. The observed reduction in mobility after transfer onto epoxy or Si/SiO₂ (but with electrical properties comparable to CVD graphene transferred to Si/SiO₂ substrates using a PMMA – assisted method, i.e. $\sim 100\text{-}1400\text{ cm}^2/\text{Vs}$,²⁴ $\sim 1100\text{ cm}^2/\text{Vs}$ ²⁵) suggests substrate scattering. The observed higher charge carrier mobilities in the case of caged graphene can be due to the fact that graphene is cleaner because of the absence of polymer contamination. The results, however, were not compared to free-standing or h-BN encapsulated graphene transistor devices, which exhibit very high carrier mobilities by removing any possible substrate scattering effects such as the one induced, for example, by Si/SiO₂ substrates. Important to mention, that depending on the quality of the CVD graphene, the floating graphene devices tend to break if the CVD graphene contains too many defects.

This work introduced interfacial caging and compared the performance of graphene with the most employed graphene transfer methods. The results are summarized in Table 2.2.

Table 2.2. Comparative analysis of graphene samples transferred with interfacial caging, PMMA, contact stamping and the hexane-assisted method.

	Interfacial caging method	PMMA-assisted method	Contact stamping	Hexane-assisted method
Continuity	full coverage of the wafer	full coverage of the wafer	partial coverage of the wafer	partial coverage of the wafer
Density of cracks	low	low	high	high
Size of wrinkles	2-3 nm high, 0.5-2 μm long	2-15 nm high, up to 10 μm long	>15 nm high, >10 μm long	2-15 nm high, up to 10 μm long
Density of wrinkles	low	high	high	medium

For polymer-based transfer using PMMA, graphene is supported by a polymer, promoting a stable mold so that further handling and lithography is possible. The polymer maintains the integrity of graphene, conforms the graphene surface and prevents graphene from forming large wrinkles. PMMA, however, conforms the catalyst, which is typically rough hence resulting in wrinkles after transfer. Another drawback of using polymers (PMMA or others) for transfer is the unavoidable presence of polymer residues on graphene, which remains even after several annealing steps. Contact stamping and hexane-assisted transfer result in cleaner, but largely cracked and wrinkled graphene.

Interfacial caging allows, on one hand, to softly support graphene from its both sides, inherently minimizing irregularities such as wrinkles and foldings using the difference in surface tension and capillary forces at a water/cyclohexane interface. On the other hand, cyclohexane, contrarily to PMMA, is a smaller molecule without a conjugated electron system, i.e. not prone to π - π stacking on graphene surface (such as benzene for example), which together with its high volatility renders cyclohexane to be very easily removed from graphene. Additionally, interfacial caging and biphasic transfer only require cooling down graphene sample without subjecting it to harsh treatments. Big areas of graphene can be transferred without inducing defects and multiple big cracks, which was confirmed by Raman spectroscopy, optical, atomic force microscopy and scanning electron microscopy.

While interfacial caging is an appealing method for transfer applications, the technique also opens new modalities for fundamental studies of floating graphene. For lithographic purposes, however, the method may be less appealing unless a physical (non-sticky) mask is used for patterning. For the first time, our interfacial approach enables electrical measurement of electrolyte-gated graphene field-effect transistors with improved electrical performance for graphene caged at a cyclohexane/water interface. The remarkably higher carrier mobility of a floating graphene flake compared to its counterpart after transfer onto either epoxy or Si/SiO₂ substrates, suggests that the intrinsic electrical properties of graphene are largely retained presumably thanks to minimal contaminations. Such high-performance, flexible graphene transistors in a

floating configuration can be readily used for in-situ sensing, for example directly at liquid/liquid interfaces.

2.3. References

1. K. S. Novoselov, S. V. Morozov, D. Jiang, Y. Zhang, S. V. Dubonos, I. V. Grigorieva, A. A. Firsov, A. K. G. Electric field effect in atomically thin carbon films. *Science* **306**, 666–669 (2004).
2. Li, X. *et al.* Transfer of large-area graphene films for high-performance transparent conductive electrodes. *Nano Lett.* **9**, 4359–4363 (2009).
3. Suk, J. W. *et al.* Transfer of CVD-grown monolayer graphene onto arbitrary substrates. *ACS Nano* **5**, 6916–6924 (2011).
4. Wood, J. D. *et al.* Annealing free, clean graphene transfer using alternative polymer scaffolds. *Nanotechnology* **26**, 55302 (2015).
5. Gao, L. *et al.* Face-to-face transfer of wafer-scale graphene films. *Nature* **505**, 190–194 (2014).
6. Feng, Y.; Huang, S.; Kang, K.; Duan, X. Preparation and characterization of graphene and few-layer graphene. *New Carbon Mater.* **26**, 26–30 (2011).
7. Su, Y. *et al.* Polymer adsorption on graphite and CVD graphene surfaces studied by surface-specific vibrational spectroscopy. *Nano Lett.* **15**, 6501–6505 (2015).
8. Han, Y. *et al.* Clean surface transfer of graphene films via an effective sandwich method for organic light-emitting diode applications. *J. Mater. Chem. C* **2**, 201–207 (2014).
9. Hallam, T., Berner, N. C., Yim, C. & Duesberg, G. S. Strain, bubbles, dirt, and folds: a study of graphene polymer-assisted transfer. *Adv. Mater. Interfaces* **1**, 1400115 (2014).
10. Pirkle, A. *et al.* The effect of chemical residues on the physical and electrical properties of chemical vapor deposited graphene transferred to SiO₂. *Appl. Phys. Lett.* **99**, 122108 (2011).

11. Kumar, K., Kim, Y.-S. & Yang, E.-H. The influence of thermal annealing to remove polymeric residue on the electronic doping and morphological characteristics of graphene. *Carbon N. Y.* **65**, 35–45 (2013).
12. Lin, W.-H. et al. A direct and polymer-free method for transferring graphene grown by chemical vapor deposition to any substrate. *ACS Nano* **8**, 1784–1791 (2014).
13. Algara-Siller, G. et al. Square ice in graphene nanocapillaries. *Nature* **519**, 443–5 (2015).
14. Zhang, G. et al. Versatile polymer-free graphene transfer method and applications. *ACS Appl. Mater. Interfaces* **8**, 8008–8016 (2016).
15. Treybal, R. E. Liquid Extraction. *Ind. Eng. Chem.* **94**, 91–99 (1951).
16. Joshi, M. D. & Anderson, J. L. Recent advances of ionic liquids in separation science and mass spectrometry. *RSC Adv.* **2**, 5470–5484 (2012).
17. Toth, P. S., Ramasse, Q. M., Velický, M. & Dryfe, R. a. W. Functionalization of graphene at the organic/water interface. *Chem. Sci.* **6**, 1316–1323 (2015).
18. Toth, P. S., Velický, M., Ramasse, Q. M., Kepaptsoglou, D. M. & Dryfe, R. a. W. Symmetric and asymmetric decoration of graphene: bimetal-graphene sandwiches. *Adv. Funct. Mater.* **25**, 2899–2909 (2015).
19. Rodgers, A. N. J. & Dryfe, R. a. W. Oxygen reduction at the liquid-liquid interface: bipolar electrochemistry through adsorbed graphene layers. *ChemElectroChem* **3**, 472–479 (2016).
20. Feng, Y. & Chen, K. Dry transfer of chemical-vapor-deposition-grown graphene onto liquid-sensitive surfaces for tunnel junction applications. *Nanotechnology* **26**, 35302 (2015).
21. Ferrari, A. C. & Basko, D. M. Raman spectroscopy as a versatile tool for studying the properties of graphene. *Nat. Nanotechnol.* **8**, 235–246

(2013).

22. Schneider, G. F. *et al.* Tailoring the hydrophobicity of graphene for its use as nanopores for DNA translocation. *Nat. Commun.* **4**, 2619 (2013).
23. Fu, W. *et al.* High mobility graphene ion-sensitive field-effect transistors by noncovalent functionalization. *Nanoscale* **5**, 12104–10 (2013).
24. Liang, X. *et al.* Toward clean and crackless transfer of graphene. *ACS Nano* **5**, 9144–9153 (2011).
25. Song, H. S. *et al.* Origin of the relatively low transport mobility of graphene grown through chemical vapor deposition. *Sci. Rep.* **2**, 337 (2012).

CHAPTER 3

Liquids relax and unify strain in graphene

Solid substrates often induce non-uniform strain and doping in graphene monolayer therefore altering the intrinsic properties of graphene, reducing its charge carrier mobilities and, consequently, the overall electrical performance. Here confocal Raman spectroscopy is exploited to study graphene directly free-floating on the surface of water, and to show that liquid supports relief the preexisting strain, have negligible doping effect and restore the uniformity of the properties throughout the graphene sheet. Such an effect originates from the molecular smoothness, structural adaptability and flexibility, lesser contamination and weaker intermolecular bonding of liquids compared to solid supports, independently of the chemical nature of the liquid. Moreover, water provides a platform to study and distinguish chemical defects from substrate-induced defects, in the particular case of hydrogenated graphene. Liquid supports, thus, are advantageous over solid supports for a range of applications, particularly for monitoring changes in the graphene structure upon chemical modification.

3.1. Introduction

Graphene is typically perceived as a two dimensional film with outstanding electrical and optical properties, but unstable mechanically and, therefore, necessitating a solid support.¹⁻³ The use of supporting substrates restored the lacking mechanical stability and prompted the development of the vast variety of graphene-based devices, such as field effect transistors,^{4,5} transparent conducting electrodes,⁶ gas and pressure sensors,^{7,8} DNA-single molecule detections, to name a few.^{9,10} Although being widely adapted for the fabrication of current graphene-based devices and technologies, solid substrates largely affect graphene due to doping and induced strain, and thus hinder the intrinsic properties of graphene.¹¹⁻¹⁹ The effect is even more prominent for CVD (chemical vapor deposition)-grown graphene samples, in which numerous inhomogeneities, inevitably caused by the growth and transfer processes, result in a wide variability of the band structure (and thus Raman signature), not only from sample to sample, but also from spot to spot within a single graphene sample.¹³⁻²⁴ This chapter studies graphene supported by liquids, namely graphene at liquid/air and liquid/liquid interfaces, with the benefit of providing molecularly defined boundaries, unlike solid/graphene/air interfaces.

Graphene caged between two immiscible liquids displays strikingly higher charge carrier mobilities as compared to graphene supported by solid substrates, presumably attributed to fewer contamination and the absence of scattering from the substrate.²⁵ However, the exact effect of liquids on the morphology and the properties of large sheets of CVD-graphene has not been ascertained yet. Although Raman spectroscopy has been recently successfully applied to characterize graphene flakes exfoliated in water,^{26,27} in that case Raman spectrum is acquired as an average spectrum over all dispersed flakes and does not provide information about strain level and deviations in a single graphene flake. Moreover, no characterization of CVD graphene at liquid-liquid interfaces has been reported so far.

By studying the effect that liquid interfaces have on the properties of graphene, this chapter demonstrates that a liquid can be a standalone support for graphene. Remarkably, confocal Raman spectroscopy on graphene free-floating at an water/air and water/oil interfaces has shown that graphene supported by

liquid(s) undergoes very small to zero strain and doping effect, compared to “conventional” solid-supported or free-standing graphene, known to be always subjected to strain and doping.^{11–19} Additionally, a statistical analysis of the graphene Raman peaks showed that also the variations of strain and doping values across the graphene sheet are significantly smaller when supported by liquids, owing to a more homogeneous and molecularly-defined graphene-liquid interface, as opposed to graphene-solid interface. Finally, the exceptional uniformity of the Raman signature of graphene in a liquid environment was used to characterize the changes in the properties of graphene upon hydrogenation and upon modifying the liquid environment.

3.2. Results and discussion

3.2.1. Raman spectroscopy of graphene at liquid interfaces

Graphene floats when placed on the surface of water due to the water surface tension. This property is routinely used during the transfer of CVD graphene from a catalyst substrate – the graphene/catalyst stack is placed on the surface of an aqueous solution of an etchant until the catalyst is fully dissolved and the graphene sheet remains free-floating at the water/air interface.^{28,29} Similarly, the use of a biphasic mixture of water (or an aqueous etchant solution) and a non-polar liquid causes the graphene/catalyst stack to float in between the two immiscible phases, which yields graphene free-floating at the liquid/liquid interface once the catalyst is etched away.²⁵ In such biphasic design graphene is supported and protected by liquids on its both sides and, therefore, is less subjected to contamination and mechanical perturbations.^{25,30} However, up to now, the only experimental insight into the graphene properties *in situ* at liquid/liquid and liquid/air interfaces has been the increase in charge carrier mobilities as compared to solid-supported graphene samples,²⁵ which indeed could be indicative of reduced contamination and strain.

This chapter presents a Raman study of a single layer graphene at water/air, water/1-octanol and water/cyclohexane interfaces; graphene on copper (as-grown), free-standing graphene (transferred onto quantifoil grids with the

interfacial caging method²⁵) and graphene transferred onto Si/SiO₂ wafers (transferred with the interfacial caging method²⁵). All graphene samples were grown according to the same growth protocol. The measurements were conducted at two excitation wavelengths, 457 nm and 532 nm respectively (as the 457 nm better suits Raman measurements of graphene on copper, and 532 nm those of graphene on Si/SiO₂), see Figure 3.1. Noteworthy, detecting just a single layer of graphene on water or at a water/liquid interface is very challenging if not impossible with a conventional Raman spectrometer, due to much larger quantities and very intensive Raman bands of the liquids. A confocal Raman spectrometer, on the other hand, can provide spatial resolution sufficient for focusing on the graphene sheet and recording a Raman spectrum where the bands of graphene and of the liquids have comparable intensities.

The two most intensive Raman bands of pristine graphene are the G band at $\sim 1585\text{ cm}^{-1}$ and 2D band at $\sim 2700\text{ cm}^{-1}$ (for 532 nm excitation wavelength, Figure 3.1a) or at $\sim 2730\text{ cm}^{-1}$ (for 457 nm excitation wavelength, Figure 3.1b). The G band originates from a first-order one-phonon scattering process and the 2D band from a second-order two-phonon intervalley scattering process, and are both typical of all sp² carbon materials.³¹ The frequencies, intensities and linewidths of the G and 2D bands of graphene are affected by the laser excitation energy (of the G band negligibly), number of graphene layers, strain and doping.^{31,32} Presence of defects in graphene lattice (including rehybridization of sp² bonds due to chemical functionalization) breaks the symmetry and activates the D band at $\sim 1350\text{ cm}^{-1}$. The relative intensity of the D band with respect to the G band is commonly used to characterize the amount of defects and disorder in graphene materials.

Graphene Raman bands can be unambiguously distinguished from the Raman bands of the liquids (as seen from Figure 3.1 and Table A2.1 in Appendix 2). The only overlap occurs between the 2D band of graphene and one of the bands of 1-octanol at $\sim 2730\text{ cm}^{-1}$ measured with 457 nm laser wavelength. But given that the 2D band of graphene is at least three times as intensive, the overlap does not hinder the determination of the 2D band position (Figure 3.1a, c). At an excitation wavelength of 532 nm, the two peaks are fully resolved as the 2D band is downshifted by $\sim 30\text{ cm}^{-1}$ due to dispersion (Figure 3.1b, d).

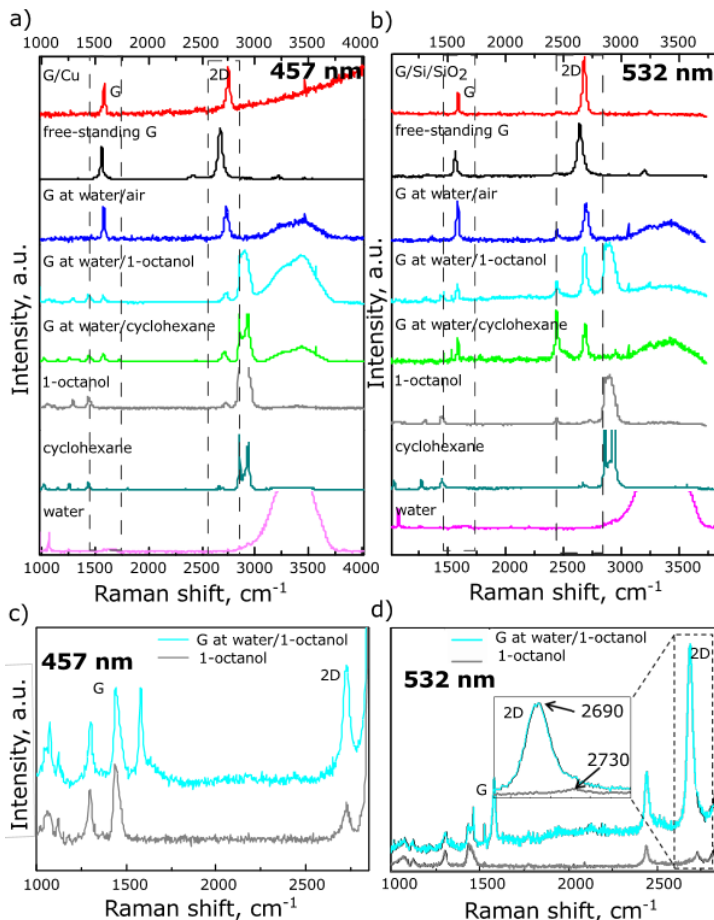


Figure 3.1. Raman spectra of graphene on different solid and liquid supports. a) Graphene-on-copper, free-standing graphene on a quantifoil grid, graphene at a water/air interface, graphene at a water/1-octanol interface, graphene at a water/cyclohexane interface, pure 1-octanol, pure cyclohexane, pure water. Laser excitation wavelength is 457 nm. b) Graphene on a Si/SiO₂ wafer, free-standing graphene on a quantifoil grid, graphene at a water/air interface, graphene at a water/1-octanol interface, graphene at a water/cyclohexane interface, pure 1-octanol, pure cyclohexane, pure water. Laser excitation wavelength is 532 nm. c) The Raman spectra of graphene at a water/1-octanol interface and of pure 1-octanol recorded at an excitation wavelength of 457 nm. The G and 2D peaks of graphene are distinguishable from the peaks of 1-octanol. d) The Raman spectra of graphene at water/1-octanol interface and pure 1-octanol recorded at 532 nm wavelength. The G and 2D peaks of graphene are distinguishable from the peaks of 1-octanol (see the inset).

Interestingly, by an in-depth Raman scanning of graphene at a liquid/liquid interface and profiling the intensities of the G and 2D modes of graphene the position of the interface can be determined (with a ~800 nm resolution limited by the instrument), while no information about the location of the interface can be obtained by profiling the peaks of the liquids (see Figures A2.1 and A2.2 in Appendix 2).

3.2.2. Graphene supported by water is strain- and doping-free

The detailed analysis of Raman peaks shifts provides information about strain and doping in the graphene lattice, and, therefore, about the effect of the substrate and environment on graphene intrinsic properties. Strain and doping induced by the substrate and by the environment are known to alter the frequencies of the G and 2D bands of graphene (w_G and w_{2D} respectively), and, in fact, can be quantified based on the shifts of the Raman bands.^{31,32} Moreover, a correlative analysis of the G and 2D peaks frequencies allows for the disentanglement of the effects of strain and doping.^{15,30} For that, the measured frequencies of G and 2D bands are plotted on a scatter plot with a non-orthogonal strain-doping framework (the so called correlation map, see Figure 3.2). Essentially, the black non-orthogonal axes titled as “hydrostatic strain”, “n-doping” and “p-doping” in Figure 3.2 represent frequencies of purely strained (doping-free) and purely doped (strain-free) graphene (and are determined theoretically and experimentally¹⁶), and their intersection point represents unstrained and undoped graphene.³⁴ Projections of a given data point on the strain and doping axes provide the values of strain and doping^{16,33,35} (differentiating between p- and n-doping, however, is not possible solely based on the Raman data, hence both types of doping are represented). The correlation maps at 457 and 532 nm wavelengths were recalculated based on a 2D mode dispersion of $100 \text{ cm}^{-1} \text{ eV}^{-1}$ ³⁶.

Remarkably, the correlation analysis of G and 2D frequencies of graphene in Figure 3.2 displayed two critical distinctions of graphene supported by liquids from graphene supported by solid substrates and from free-standing graphene: very small absolute values and very small deviations of strain and doping induced by the liquids.

Generally, the substrate and environment always induce strain and doping in graphene. Achieving a fully strain- and doping-free graphene area requires meticulous fabrication of a free-standing sheet suspended in a very particular geometry (across a circular well).¹⁶ In fact, the broadly scattered data points and wide frequency histograms in Figure 3.2 for graphene on copper, graphene on Si/SiO₂ and free-standing graphene indicate wide variations of strain and doping in these samples. Particularly, as seen from Figure 3.2a graphene on copper (the growth substrate) undergoes a wide range of strain values – from -0.8% (compressive strain) till 0.7% (tensile strain) with no evident dominating values (see wide frequency distribution histograms in Figure 3.2a). Importantly, such ununiformity of strain values occurs from spot to spot within a single graphene sheet, and is reproduced in all samples of graphene-on-copper (see Figure A2.3a in Appendix 2 for sample-to-sample variations). The wide variations of the strain level are typical for CVD graphene on copper and originate from the mismatch of the lattice parameters between graphene and copper and from the inhomogeneity of the surface of copper (differently oriented domains, grain boundaries, defects, steps in the case of unpolished polycrystalline copper).^{17,20–23}

Similarly, free-standing graphene also exhibits very wide strain variations, ranging from -0.1% to 1% (Figure 3.2 and Figures A2.3b and A2.3c in Appendix 2), indicating that the free-standing configuration induces predominantly tensile strain. Strain is known to vary significantly from spot to spot in suspended graphene films depending on the position of the spot with respect to the center and the supported part.^{17,37} Importantly, the measured strain values for free-standing CVD graphene are higher than those reported for an exfoliated free-standing graphene flake,³⁷ demonstrating that the CVD growth and possibly the transfer process induce the strain field that remains in graphene even when it is suspended, i.e. is in a potentially zero- or low-strain geometry.

Si/SiO₂ substrate is known to have a strain relaxation effect on graphene,²² and in fact, graphene transferred onto a Si/SiO₂ wafer exhibits much narrower data scattering and strain variation from -0.3% to 0.2% (Figure 3.2b and Figure A2.3d in Appendix 2).

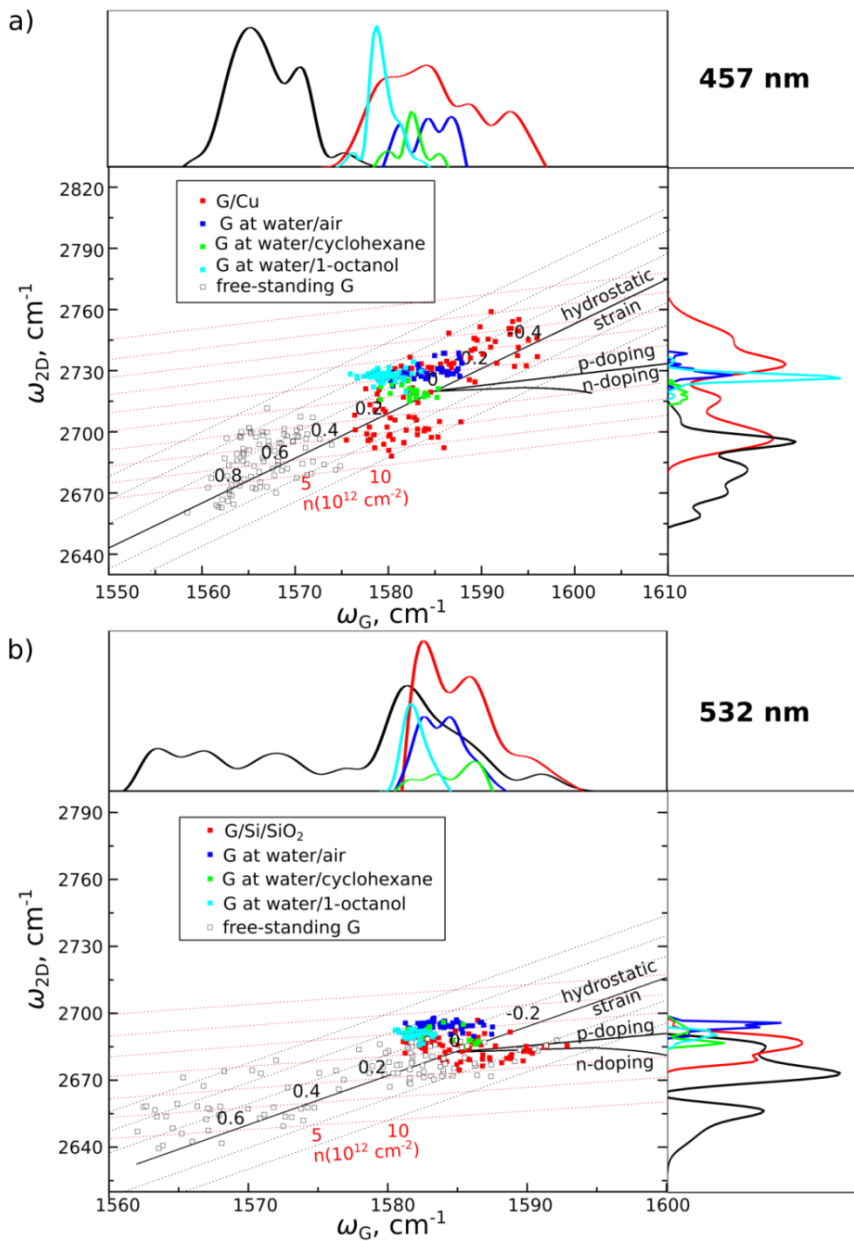


Figure 3.2. Correlation maps and statistical distributions of G and 2D Raman frequencies (ω_G and ω_{2D}) for graphene on different solid and liquid supports. a) Graphene on copper, graphene at water/air interface, graphene at water/cyclohexane interface, graphene at water/1-octanol interface and free-standing graphene on a quantifoil grid.

Black and red dash lines represent the strain and doping axes respectively. Laser excitation wavelength is 457 nm. b) Graphene on Si/SiO₂ wafer, graphene at water/air interface, graphene at water/cyclohexane interface, graphene at water/1-octanol interface, and free-standing graphene on a quantifoil grid. Black and red dash lines represent the strain and doping axes respectively. Laser excitation wavelength is 532 nm.

In contrast to the solid-supported and free-standing graphene, graphene floating at a water/air or a water/oil interfaces displays notably lower strain values and variations (Figure 3.2). Strain values of graphene at the water/air, water/cyclohexane and water/1-octanol cluster around zero with deviations within 0.1% (Figure 3.2).

In addition to lower strain, the correlation maps in Figure 3.2 also indicate lower and more uniform doping levels in the samples of graphene at liquid interfaces (compared to graphene on solid supports). Specifically, for all graphene samples at liquid interfaces the doping values deviate in the range of $2 \times 10^{12} \text{ cm}^{-2}$ - $3 \times 10^{12} \text{ cm}^{-2}$, up to $10 \times 10^{12} \text{ cm}^{-2}$ for graphene on copper and free-standing graphene, and up to $8 \times 10^{12} \text{ cm}^{-2}$ for the graphene on Si/SiO₂ (Figure 3.2).

Remarkably, graphene on water shows similar level of doping and slightly lower fluctuations of strain compared to graphene supported by h-BN (Figure A2.5 in Appendix 2). H-BN is known as a solid substrate with the best conformity to graphene and lowest induced strain and doping, allowing for the highest charge carrier mobilities reported for graphene.^{38,39} Important to note, however, that only CVD graphene on CVD h-BN (as a comparison to the CVD graphene in liquids) was studied in this work, while lower levels of strain and doping might be observed in mechanically exfoliated flakes of graphene on h-BN.

Figure 3.2 shows that the position of the Raman 2D band is a particularly evident distinction between the graphene supported by the liquids and graphene supported by solid substrates: the distribution histograms for all liquids are narrow with average values of $\sim 2727 \text{ cm}^{-1}$ (457 nm excitation wavelength, Figure 3.2a) and $\sim 2690 \text{ cm}^{-1}$ (532 nm excitation wavelength, Figure 3.2b). The G band, on the other hand, is less sensitive to strain,^{40,41} and therefore, is not indicative of strain-induced changes in graphene properties, although narrower distributions of the G band positions in Figure 3.2 do point at better uniformity of graphene-liquid interfaces as opposed to graphene-solid interfaces.

Additionally to the band frequencies, the full widths at half-maximum (FWHM) of the G and 2D bands (denoted here Γ_G and Γ_{2D} respectively) can also be used for monitoring strain and doping in graphene (Figure 3.3). A narrower G band corresponds to a larger charge doping,⁴² and a broadening of the 2D band suggests a nonuniform anisotropic character of strain.^{20,32,43} Although graphene supported by liquids displays more uniform strain fields than graphene on solids (Figure 3.2), the 2D bandwidths of graphene on liquids are similar to those of graphene on solids (Figure 3.3). Such broadening of the 2D band of graphene on liquids is likely to be caused by instrumental factors: Raman spectra of graphene floating in liquids typically have higher noise levels (due to vibrations on the liquid surface causing the graphene to fluctuate from the focal plane of the microscope) than those of graphene on solid substrates, leading to less accurate determination of peak widths. The positions of peaks maximums, on the other hand, are not affected by increased noise level and can be determined accurately.

Overall, replacing solid supports with liquid(s) results in an articulate relaxation of strain and reduction of doping level in graphene sheet. Additionally, the spot-to-spot deviations of strain and doping within the graphene sheet are significantly smaller for liquid-supported graphene, indicating more uniform properties of the graphene surface.

Importantly, the observed effects are stable in time, and the Raman signature and statistical distributions of the strain and doping values in graphene-on-water remained unchanged even after floating on the surface of water for eight days (Figure A2.6 in Appendix 2).

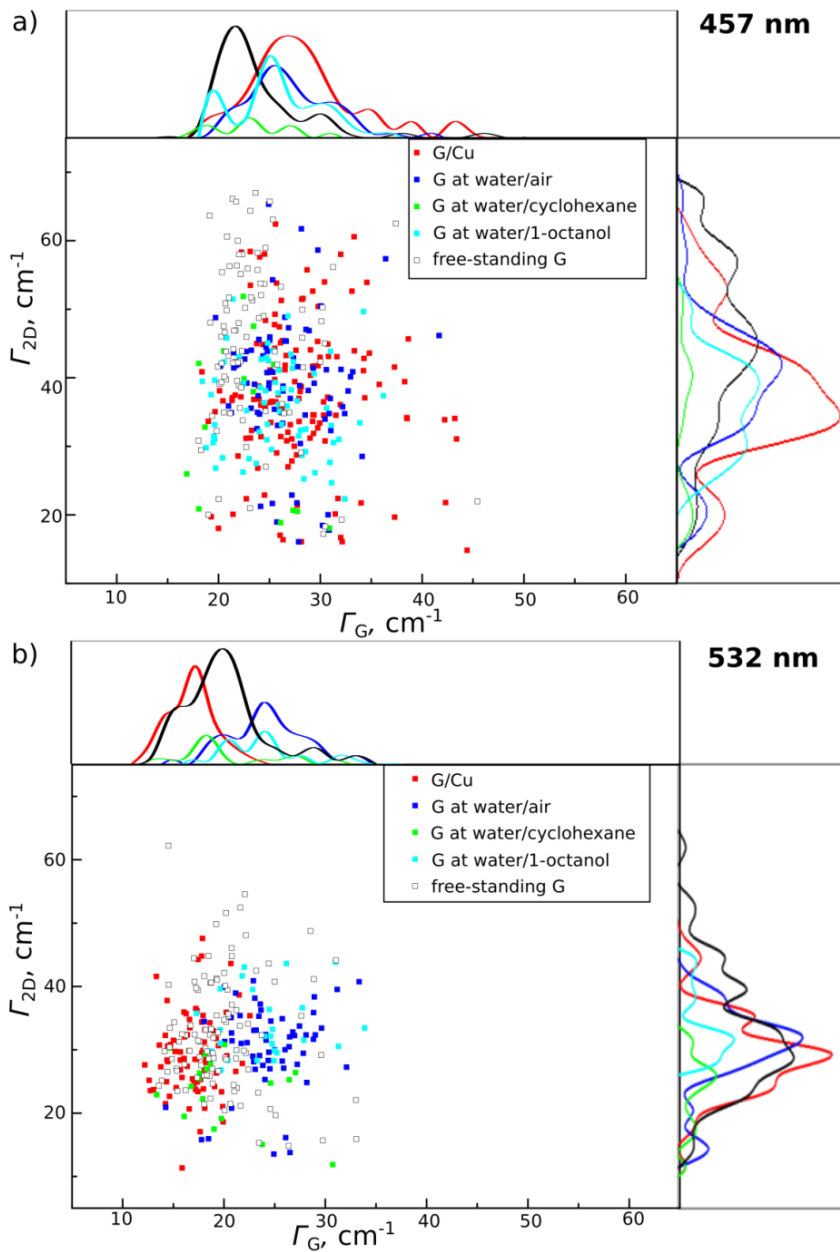


Figure 3.3. Correlation maps and statistical distributions of G and 2D Raman full widths at half maximum (FWHM or Γ_G and Γ_{2D}) for graphene on different solid and liquid supports. a) Graphene on copper, graphene at water/air interface, graphene at water/cyclohexane interface, graphene at water/1-octanol interface and free-standing

graphene on a quantifoil grid. Laser excitation wavelength is 457 nm. b) Graphene on Si/SiO₂ wafer, graphene at water/air interface, graphene at water/cyclohexane interface, graphene at water/1-octanol interface, and free-standing graphene on a quantifoil grid. Laser excitation wavelength is 532 nm.

3.2.3. Effects of different liquid environment on strain and doping in floating graphene

Next, the effects of different liquid interfaces on strain and doping levels of graphene were examined, based on the correlation map of G and 2D bands positions (Figure 3.4). Four different interfaces namely water/air, water/cyclohexane, water/1-octanol and deuterated water/air were studied. Interestingly, the data points for all interfaces are tightly clustered with small deviations from the point of zero strain and doping (within 0.1-0.2% for strain and 2×10^{12} - 3×10^{12} cm⁻² for doping, see Figure 3.4a and b).

As seen from the scattering of the data points in Figure 3.4a and b, graphene at water/1-octanol interface seems to undergo slightly lower and more uniform strain and doping than at water/cyclohexane interface, which can be attributed to a lower polarity gradient and stronger association (between the liquids) of the water/1-octanol interface.⁴⁴ Interestingly, compared to the graphene at the water/1-octanol and water/cyclohexane interfaces, graphene at water/air and deuterated water/air interfaces exhibit more uniform strain distributions, but also are slightly more doped (Figure 3.4a, b).

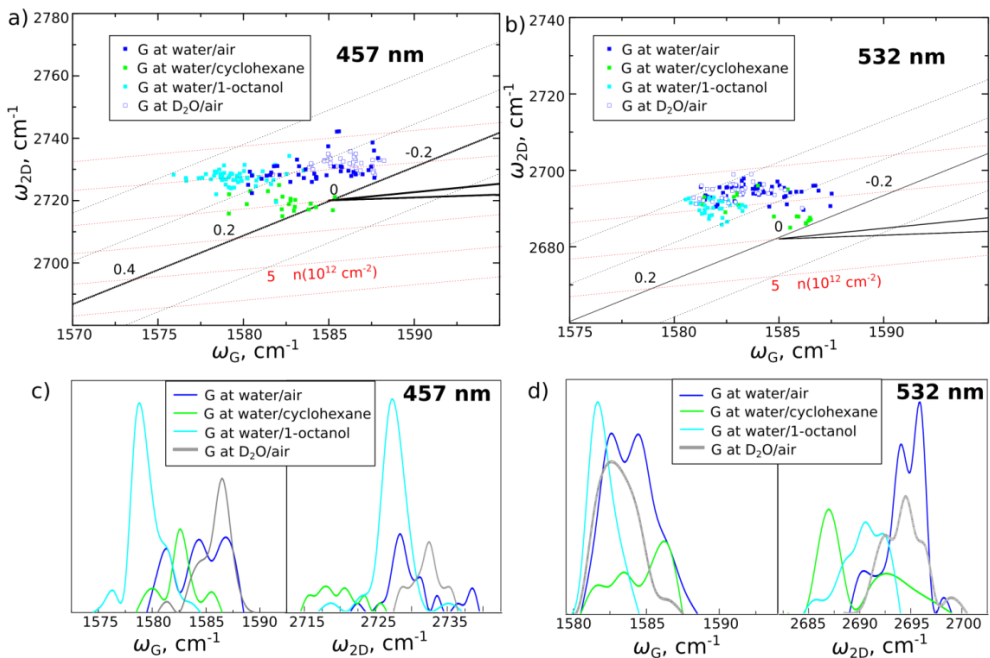


Figure 3.4. Effects of different liquid environment on strain and doping in floating graphene a) Correlation map of G and 2D band frequencies (ω_G and ω_{2D}) for graphene at the water/air interface, graphene at the water/cyclohexane interface, graphene at the water/1-octanol interface and graphene at the deuterated water/air interface. Laser excitation wavelength is 457 nm. b) Correlation map of G and 2D Raman frequencies (ω_G and ω_{2D}) for graphene at the water/air interface, graphene at the water/cyclohexane interface, graphene at the water/1-octanol interface and graphene at the deuterated water/air interface. Laser excitation wavelength is 532 nm. c) Statistical distributions of G and 2D Raman frequencies (ω_G and ω_{2D}) for graphene at water/air interface, graphene at water/cyclohexane interface, graphene at water/1-octanol interface and graphene at deuterated water/air interface. Laser excitation wavelength is 457 nm. d) Statistical distributions of G and 2D Raman frequencies (ω_G and ω_{2D}) for graphene at water/air interface, graphene at water/cyclohexane interface, graphene at water/1-octanol interface and graphene at deuterated water/air interface. Laser excitation wavelength is 532 nm.

The observed differences in strain and doping levels of graphene at different liquid interfaces are, therefore, insignificant, especially in contrast with their drastic difference from the strain and doping levels in graphene on solid

substrates demonstrated above. Remarkably, dissimilarities in the properties of the liquid interfaces, such as interfacial tensions, polarity gradients and intermolecular bonding did not have significantly different effect on the Raman signature of graphene.

Importantly, liquid/graphene/air and liquid/graphene/liquid interfaces are molecularly smooth, which was confirmed at least for the case of water/graphene interface by MD simulations (Figure A2.7 in Appendix 2), especially when compared to graphene in vacuum. This implies that the molecular smoothness together with the structural adaptability of liquid interfaces are likely to be the causes of the strain relaxation effect, irrespective of the chemical and physical properties of the liquids.

3.2.4. Raman spectroscopy of graphene on liquid supports to characterize functionalization of graphene

Finally, liquid supports were utilized to characterize the properties of graphene upon functionalization, specifically on the example of hydrogenation of graphene. Hydrogenated graphene (h-G) is typically characterized by the position (w_D) and relative intensity (the ratio between the intensities of the D and the G bands, or the I_D/I_G ratio) of the Raman D band arising from the formation of C-H bonds and rehybridization of the graphene lattice from sp^2 to sp^3 .^{45,46} Two types of samples with different hydrogenation degrees were prepared using a hydrogen plasma on graphene grown on copper (see Methods In Appendix 2 for details) – with plasma treatment duration of respectively 10 s and 60 s.⁴⁷ Raman spectra were recorded for a pristine graphene on copper and on water (the same graphene sheet before and after etching the copper and replacing the etchant with pure water) and for hydrogenated graphene samples on copper and water (same samples of hydrogenated graphene before and after etching the copper and replacing the etchant with pure water), Figure 3.5.

First, for the samples that underwent 10 s of hydrogenation, h-G floating on water have much narrower distributions of the D peak position w_D compared to that of h-G on copper ($1368 \pm 1 \text{ cm}^{-1}$ for h-G/water versus $1376 \pm 5 \text{ cm}^{-1}$ for h-G/Cu, see Figure 3.5a). Similarly, the distribution of the D peak width Γ_D is also narrower

for h-G on water as opposed to h-G on copper (Figure A2.4a in Appendix 2). The narrower distribution of w_D values in the case of h-G/water (Figure 3.5a) suggests the dominance of only one type of defects (hydrogenation-caused sp^3 carbon atoms), while in the case of h-G/Cu the multimodal distribution of w_D must be caused by a different types of defects (sp^3 carbon atoms and other defects not related to hydrogenation) or doping effect.^{48,49} The samples of h-G/Cu and h-G/water are, however, essentially the same sheet of graphene tested before and after copper etching, and, in principle, should have identical types and amounts of defects. The main differences between the samples (accounting for the difference in D peaks) are the different levels of strain and doping induced by copper and water. In fact, although strain *per se* does not generate a D peak in graphene, the strain fields in graphene induced by copper can activate defects such as interstitials and vacancies along the grain boundaries of graphene,⁵⁰ resulting in the shift and broadening of the D peak. This does not take place in the samples of h-G/water, because of lower strain induced by water (Figure 3.5c). Additionally, due to inhomogeneous strain fields in h-graphene on copper, there is a variation of C-H bond lengths across the h-graphene sheet, also resulting in the variation of the phonon frequencies (i.e. D peak positions).

In addition to strain-activated defects, doping is also known to cause shift in the D mode frequency and alter the D mode intensity.^{48,49} As shown in Figure 3.2a, copper induces significantly higher and more inhomogeneous doping levels in graphene compared to water. As a result, the inhomogeneous doping (i.e. different doping values across the sample) in the case of copper causes a wider variation in the D peak frequencies and intensities.

Using water as a substrate, therefore, allows extracting the effect of hydrogenation from substrate-activated defects. Furthermore, not only the w_D , but also the I_D/I_G ratio displays a lower variability across the h-G sheet when supported by water as opposed to copper (Figure 3.5b). Since in the case of h-G/water the D peak originates solely from hydrogenation, the I_D/I_G histogram of h-G/water is a better estimate of hydrogenation degree than that of h-G/Cu. Interestingly, the I_D/I_G histogram of h-G/Cu would mistakenly indicate a less uniform (compared to h-G/water) hydrogenation of the graphene sheet (Figure 3.5b). Given that the graphene sheets in h-G/water and h-G/Cu have identical degree and distribution of hydrogenation, the wider I_D/I_G histogram of h-G/Cu

thus proves the contribution of substrate-activated defects and doping in the intensity of the D peak.

Finally, variations in strain and doping levels can be assessed based on the correlation map of G and 2D bands in Figure 3.5c. h-G/water displays slightly lower variations (within 10^{13} cm^{-2}) of doping levels than h-G/Cu (within $15 \times 10^{12} \text{ cm}^{-2}$), which confirms that doping can be one of the reasons for the inhomogeneity of the D band position and intensity in the case of h-G/Cu. Similarly to pristine graphene, hydrogenated graphene is also subjected to greater and less uniform strain on copper, varying from -0.6 % to 0.1 %, than it is on water, where the strain varies from -0.2 % to 0 % (Figure 3.5c). Interestingly, graphene became slightly more doped after the hydrogenation, with the doping values varying from $2 \times 10^{12} \text{ cm}^{-2}$ to $12 \times 10^{12} \text{ cm}^{-2}$ for h-G/water and from 0 to $5 \times 10^{12} \text{ cm}^{-2}$ for the G/water, as seen from the correlation map for h-G/water and G/water (Figure 3.5c). Strain levels, on the other hand, remain low and unaffected by hydrogenation and vary between 0 and 0.2 % both for G/water and h-G/water (Figure 3.5c). Measurements on copper, in contrast, do not allow differentiating between G/Cu and h-G/Cu due to the wide variations of strain (Figure 3.5c).

For 60 s hydrogenation, results are similar to the 10 s hydrogenation (Figure 3.5d-f). The narrow distributions and the same mean values of w_D and Γ_D in the both cases (Figure 3.5d and Figure A2.4b in Appendix 2) demonstrate that the D peak of h-G/water reflects the hydrogenation effect (and not other defects) and is, therefore, a better indication of hydrogenation than the D peak of h-G/Cu. Interestingly, comparison between the I_D/I_G distributions of h-G/water in Figure 3.5b and 3.5e demonstrates that longer plasma exposure results in higher and less uniform hydrogenation of the graphene, which is in agreement with previous studies.^{51,52} Even more pronouncedly than in the case of 10s hydrogenation (Figure 3.5c), hydrogenation for 60 s results in higher doping values than in pristine graphene, from $0\text{-}5 \times 10^{12} \text{ cm}^{-2}$ for G/water to $5\text{-}15 \times 10^{12} \text{ cm}^{-2}$ for h-G/water (Figure 3.5f). Increased doping levels in hydrogenated graphene compared to pristine graphene were also observed previously^{45,53} and are linked to the difference in the work functions between graphene and the substrate.⁵⁴ The work function of graphene^{54,55} is close to that of water,⁵⁶ which results in insignificant charge carrier transfer between graphene and the substrate, and, therefore, low

doping levels in G/water observed in our work. Due to rehybridization of carbon atoms and formation of C-H bonds, hydrogenation alters the work function of graphene,⁵⁷⁻⁵⁹ increasing the difference with the work function of water and, therefore, facilitating doping of h-G.

Like in the case of 10 s hydrogenation, the strain levels did not change upon 60 s hydrogenation and are close to 0 with the deviations of 0.1 % for both G/water and h-G/water (Figure 3.5f).

By contrast, no conclusive evaluation of the hydrogenation effect can be made based on the data from h-G/Cu due to the higher variation in doping values ($\pm 10^{13}$ cm⁻² versus $\pm 5 \times 10^{12}$ cm⁻² for h-G/water) and possibly the presence of strain-activated defects (wide distribution histogram of w_D , Figure 3.5d) and their different contribution to the intensity of the D band (Figure 3.5e).³² Large variations of strain in h-G/Cu (-0.2 %-0.6 %) and G/Cu (-0.3 %-0.5 %), however, result in overlapping and thus non-distinguishable data on the correlation maps of G and 2D bands for the pristine and hydrogenated graphene supported by copper (Figure 3.5f).

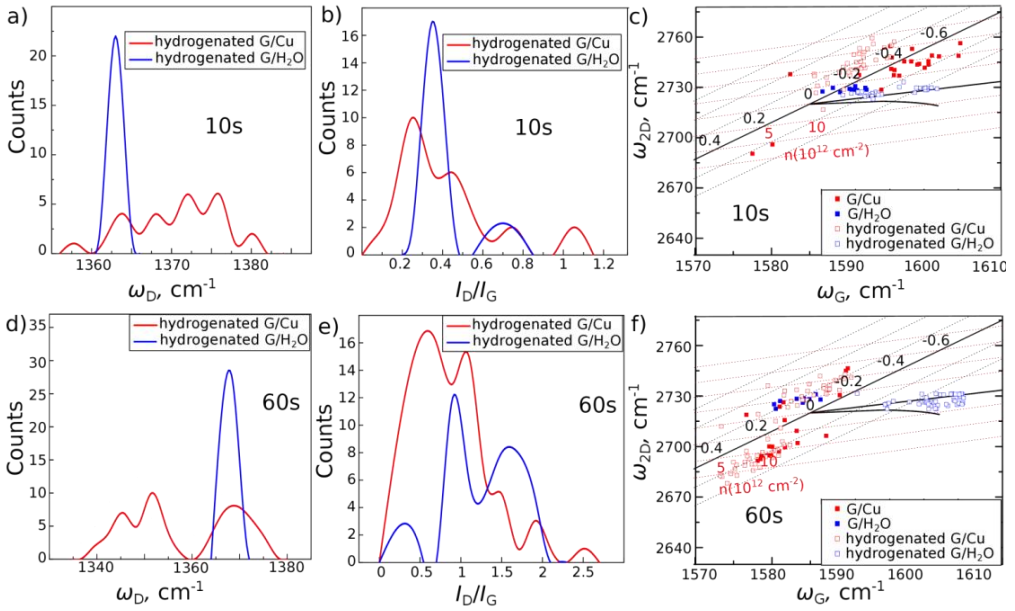


Figure 3.5. Raman analysis of hydrogenated graphene (h-G). a) Statistical distributions of D peak frequencies (ω_D) of h-G on copper and water. Hydrogenation time was 10 s. b) Statistical distributions of I_D/I_G ratios of hydrogenated graphene (h-G) on copper and on water after etching the copper. Hydrogenation time was 10 s. c) Correlation map of G and 2D peaks frequencies of non-treated graphene on copper, non-treated graphene on water, h-G on copper and h-G on water. Hydrogenation time was 10 s. d) Statistical distributions of D peak frequencies (ω_D) of h-G on copper and water. Hydrogenation time was 60 s. e) Statistical distributions of I_D/I_G ratios of hydrogenated graphene (h-G) on copper and on water after etching the copper. Hydrogenation time was 60 s. f) Correlation map of G and 2D peaks frequencies of non-treated graphene on copper, non-treated graphene on water, h-G on copper and h-G on water. Hydrogenation time was 60 s.

Ultimately, using water as a substrate minimizes the impact of the substrate not only on the G and 2D bands, directly responsive to strain, but also on the D band activated by defects in the graphene structure. Unlike hydrogenated graphene on copper, the D band of hydrogenated graphene on water originates solely from the hydrogenation effect, which allows accurately assessing the degree and

uniformity of hydrogenation and tracking the effect of hydrogenation on the strain and doping levels in graphene.

3.3. Conclusions

In a liquid attractive forces between the molecules are weaker than in a solid, allowing the molecules to move.^{60,61} Continuous movement of molecules allows the formation of a homogeneous, energy-minimized, self-healing surface free of kinetic traps (and consequently, defects), which adapts to and takes the shape of the surface the liquid is in contact with, i.e. graphene in our case.^{60,61} Homogeneity, molecular smoothness, structural adaptability of liquid interfaces are universal properties of all liquids, independently of their chemical nature.⁶⁰⁻⁶² Remarkably, various liquid interfaces relax and unify strain in graphene down to similar values, indicating that the structural, rather than chemical, properties of liquids are responsible for the strain relaxation effect.

In summary, graphene floating directly on a liquid or even buried in between two liquids was studied by Raman spectroscopy. All three major Raman bands of graphene – the D, G and 2D band remain unaffected by liquid substrates. Using liquids to support graphene, thus, can be beneficial over solid substrates whenever the properties of graphene need to be accurately monitored. Here the advantages of a water support were showcased through the example of hydrogenation of graphene, but can, in principle be applied for studying other effects on graphene structure.

3.4. References

1. Lau, C. N., Bao, W. & Velasco, J. Properties of suspended graphene membranes. *Mater. Today* **15**, 238–245 (2012).
2. Zandiataashbar, A. *et al.* Effect of defects on the intrinsic strength and stiffness of graphene. *Nat. Commun.* **5**, 3186 (2014).
3. Zhang, P. *et al.* Fracture toughness of graphene. *Nat. Commun.* **5**, 3782 (2014).
4. K. S. Novoselov, S. V. Morozov, D. Jiang, Y. Zhang, S. V. Dubonos, I. V. Grigorieva, A. A. Firsov, A. K. G. Electric field effect in atomically thin carbon films. *Science* **306**, 666–669 (2004).
5. Lemme, M. C., Echtermeyer, T. J., Baus, M. & Kurz, H. A Graphene field-effect device. *IEEE Electron Device Lett.* **28**, 282–284 (2007).
6. Matyba, P., Yamaguchi, H., Eda, G., Chhowalla, M., Edman, L. y Robinson, N. D. Graphene and mobile ions: the key to all plastic, solution processed light emitting devices. *ACS Nano* **4**, 637–642 (2010).
7. Schedin, F. *et al.* Detection of individual gas molecules adsorbed on graphene. *Nat. Mater.* **6**, 652–655 (2007).
8. Xu, Y. *et al.* In-plane and tunneling pressure sensors based on graphene/hexagonal boron nitride heterostructures. *Appl. Phys. Lett.* **99**, 1–4 (2011).
9. Heerema, S. J. & Dekker, C. Graphene nanodevices for DNA sequencing. *Nat. Nanotechnol.* **11**, 127–136 (2016).
10. Arjmandi-Tash, H., Belyaeva, L. A. & Schneider, G. F. Single molecule detection with graphene and other two-dimensional materials: nanopores and beyond. *Chem. Soc. Rev.* **45**, 476–493 (2016).
11. Guinea, F., Katsnelson, M. I. & Geim, A. K. Energy gaps and a zero-field quantum Hall effect in graphene by strain engineering. *Nat. Phys.* **6**, 30–33 (2009).
12. Pereira, V. M. & Castro Neto, A. H. Strain engineering of graphene's electronic structure. *Phys. Rev. Lett.* **103**, 46801 (2009).

13. Bao, W. *et al.* Controlled ripple texturing of suspended graphene and ultrathin graphite membranes. *Nat. Nanotechnol.* **4**, 562–566 (2009).
14. Wang, Y. Y. *et al.* Raman studies of monolayer graphene: the substrate effect. *J. Phys. Chem. C* **112**, 10637–10640 (2008).
15. Hu, Z., Prasad Sinha, D., Lee, J. U. & Liehr, M. Substrate dielectric effects on graphene field effect transistors. *J. Appl. Phys.* **115**, (2014).
16. Lee, J. E., Ahn, G., Shim, J., Lee, Y. S. & Ryu, S. Optical separation of mechanical strain from charge doping in graphene. *Nat. Commun.* **3**, 1024 (2012).
17. Bendiab, N. *et al.* Unravelling external perturbation effects on the optical phonon response of graphene. *J. Raman Spectrosc.* **49**, 130–145 (2018).
18. Neumann, C. *et al.* Raman spectroscopy as probe of nanometre-scale strain variations in graphene. *Nat. Commun.* **6**, 8429 (2015).
19. Lee, Y. R., Huang, J. X., Lin, J. C. & Lee, J. R. Study of the substrate-induced strain of as-grown graphene on Cu(100) using temperature-dependent Raman spectroscopy: estimating the mode Grüneisen parameter with temperature. *J. Phys. Chem. C* **121**, 27427–27436 (2017).
20. He, R. *et al.* Large physisorption strain in chemical vapor deposition of graphene on copper substrates. *Nano Lett.* **12**, 2408–2413 (2012).
21. Yu, V., Whiteway, E., Maassen, J. & Hilke, M. Raman spectroscopy of the internal strain of a graphene layer grown on copper tuned by chemical vapor deposition. *Phys. Rev. B - Condens. Matter Mater. Phys.* **84**, 1–5 (2011).
22. Troppenz, G. V., Gluba, M. A., Kraft, M., Rappich, J. & Nickel, N. H. Strain relaxation in graphene grown by chemical vapor deposition. *J. Appl. Phys.* **114**, (2013).
23. Zhang, Y. *et al.* Defect-like structures of graphene on copper foils for strain relief investigated by high-resolution scanning tunneling microscopy. *ACS Nano* **5**, 4014–4022 (2011).
24. Yoon, D., Son, Y.-W. & Cheong, H. Negative thermal expansion coefficient of graphene measured by Raman spectroscopy. *Nano Lett.* **11**, 3227–3231 (2011).

25. Belyaeva, L. A., Fu, W., Arjmandi-Tash, H. & Schneider, G. F. Molecular caging of graphene with cyclohexane: transfer and electrical transport. *ACS Cent. Sci.* **2**, 904–909 (2016).
26. Mary, R. *et al.* 1.5 GHz picosecond pulse generation from a monolithic waveguide laser with a graphene-film saturable output coupler. *Opt. Express* **21**, 7943–7950 (2013).
27. Bepete, G., Pénicaud, A., Drummond, C. & Anglaret, E. Raman signatures of single layer graphene dispersed in degassed water, “Eau de Graphene”. *J. Phys. Chem. C* **120**, 28204–28214 (2016).
28. Reina, A. *et al.* Transferring and identification of single- and few-layer graphene on arbitrary substrates. *J. Phys. Chem. C* **112**, 17741–17744 (2008).
29. Li, X. *et al.* Large-area synthesis of high-quality and uniform graphene films on copper foils. *Science* **324**, 1312–1314 (2009).
30. Zhang, G. *et al.* Versatile polymer-free graphene transfer method and applications. *ACS Appl. Mater. Interfaces* **8**, 8008–8016 (2016).
31. Malard, L. M., Pimenta, M. A., Dresselhaus, G. & Dresselhaus, M. S. Raman spectroscopy in graphene. *Phys. Rep.* **473**, 51–87 (2009).
32. Ferrari, A. C. & Basko, D. M. Raman spectroscopy as a versatile tool for studying the properties of graphene. *Nat. Nanotechnol.* **8**, 235–246 (2013).
33. Mueller, N. S. *et al.* Evaluating arbitrary strain configurations and doping in graphene with Raman spectroscopy. *2D Mater.* **5**, 15016 (2018).
34. Frank, O. *et al.* Phonon and structural changes in deformed bernal stacked bilayer graphene. *Nano Lett.* **12**, 687–693 (2012).
35. Froehlicher, G. & Berciaud, S. Raman spectroscopy of electrochemically gated graphene transistors: Geometrical capacitance, electron-phonon, electron-electron, and electron-defect scattering. *Phys. Rev. B* **91**, 205413 (2015).
36. Costa, S. D. *et al.* Resonant Raman spectroscopy of graphene grown on copper substrates. *Solid State Commun.* **152**, 1317–1320 (2012).

37. Metten, D., Federspiel, F., Romeo, M. & Berciaud, S. Probing built-in strain in freestanding graphene monolayers by raman spectroscopy. *Phys. Status Solidi Basic Res.* **250**, 2681–2686 (2013).
38. Wang, L. *et al.* One-dimensional electrical contact to a two-dimensional material. *Science* **342**, 614–617 (2013).
39. Banszerus, L. *et al.* Ultrahigh-mobility graphene devices from chemical vapor deposition on reusable copper. *Sci. Adv.* **1**, e1500222 (2015).
40. Teague, M. L. *et al.* Evidence for strain-induced local conductance modulations in single-layer graphene on SiO₂. *Nano Lett.* **9**, 2542–2546 (2009).
41. Huang, M., Yan, H., Heinz, T. F. & Hone, J. Probing strain-induced electronic structure change in graphene by Raman spectroscopy. *Nano Lett.* **10**, 4074–4079 (2010).
42. Yan, J., Zhang, Y., Kim, P. & Pinczuk, A. Electric field effect tuning of electron-phonon coupling in graphene. *Phys. Rev. Lett.* **98**, 166802 (2007).
43. Yoon, D., Son, Y.-W. & Cheong, H. Strain-dependent splitting of the double-resonance Raman scattering band in graphene. *Phys. Rev. Lett.* **106**, 155502 (2011).
44. Steel, W. H. & Walker, R. A. Measuring dipolar width across liquid-liquid interfaces with ‘molecular rulers’. *Nature* **424**, 296–299 (2003).
45. Elias, D. C. *et al.* Control of graphene’s properties by reversible hydrogenation: evidence for graphane. *Science* **323**, 610–613 (2009).
46. Cançado, L. G. *et al.* Quantifying defects in graphene via Raman spectroscopy at different excitation energies. *Nano Lett.* **11**, 3190–3196 (2011).
47. Jiang, L., Fu, W., Birdja, Y. Y., Koper, M. T. M. & Schneider, G. F. Quantum and electrochemical interplays in hydrogenated graphene. *Nat. Commun.* **9**, 793 (2018).
48. Liu, J. *et al.* The dependence of graphene Raman D-band on carrier density. *Nano Lett.* **13**, 6170–6175 (2013).
49. Bruna, M. *et al.* Doping dependence of the Raman spectrum of defected

- graphene. *ACS Nano* **8**, 7432–7441 (2014).
50. Wang, B., Puzyrev, Y. & Pantelides, S. T. Strain enhanced defect reactivity at grain boundaries in polycrystalline graphene. *Carbon N. Y.* **49**, 3983–3988 (2011).
 51. Whitener, K. E., Robinson, J. T. & Sheehan, P. E. Protection from below: stabilizing hydrogenated graphene using graphene underlayers. *Langmuir* **33**, 13749–13756 (2017).
 52. Bangert, U., Pan, C. T., Nair, R. R. & Gass, M. H. Structure of hydrogen-dosed graphene deduced from low electron energy loss characteristics and density functional calculations. *Appl. Phys. Lett.* **97**, 253118 (2010).
 53. Matis, B. R. *et al.* Surface doping and band gap tunability in hydrogenated graphene. *ACS Nano* **6**, 17–22 (2012).
 54. Niesner, D. & Fauster, T. Image-potential states and work function of graphene. *J. Phys. Condens. Matter* **26**, 393001 (2014).
 55. Yu, Y.-J. *et al.* Tuning the graphene work function by electric field effect. *Nano Lett.* **9**, 3430–3434 (2009).
 56. Olivieri, G., Goel, A., Kleibert, A., Cvetko, D. & Brown, M. A. Quantitative ionization energies and work functions of aqueous solutions. *Phys. Chem. Chem. Phys.* **18**, 29506–29515 (2016).
 57. Peng, X., Tang, F. & Copple, A. Engineering the work function of armchair graphene nanoribbons using strain and functional species: a first principles study. *J. Phys. Condens. Matter* **24**, 75501 (2012).
 58. Leenaerts, O., Peelaers, H., Hernández-Nieves, A. D., Partoens, B. & Peeters, F. M. First-principles investigation of graphene fluoride and graphane. *Phys. Rev. B* **82**, 195436 (2010).
 59. Wang, M., Zhou, Y., Kong Hark, S. & Zhu, X. A saw-tooth scaling of work function in hydrogenated graphene. *Preprint at <http://arXiv.org/1707.07784>* (2017).
 60. Hansen, J.-P. & R. McDonald, I. Theory of simple liquids: with applications to soft matter: fourth edition. *Elsevier* (2013).
 61. Fawcett, W. R. Liquids, solutions, and interfaces: from classical

macroscopic descriptions to modern microscopic details. *Oxford Univ. Press* (2004).

62. Ninham, B. & Lo Nostro, P. Molecular forces and self-assembly: in colloid, nano sciences and biology. *Phys. Today* **64**, (2010).

CHAPTER 4

Contact angle measurement of freestanding square millimeter single layer graphene

Square millimeters of free-standing graphene do not exist per se because of thermal fluctuations in two-dimensional (2D) crystals and their tendency to collapse during the detachment from the substrate. Here, millimeter-scale freely suspended graphene is formed by injecting an air bubble underneath a graphene monolayer floating at the water-air interface, which allowed us to measure the contact angle on fully free-standing non-contaminated graphene. A captive bubble measurement shows that free-standing clean graphene is hydrophilic with a contact angle of $42^{\circ}\pm 3^{\circ}$. The proposed design provides a simple tool to probe and explore the wettability of 2D materials in free-standing geometries and will expand our perception of 2D materials technologies from microscopic to now millimeter-scales.

This chapter was published as an article: Anna V. Prydatko*, Liubov A. Belyaeva*, Lin Jiang, Lia M.C. Lima and Grégory F. Schneider, Nat.Comm., 2018, 9, 4185.

4.1. Introduction

The wetting properties of graphene have been a subject of intensive theoretical and experimental investigations over the last decade. Extremely thin and electrically conductive, graphene is widely used in biosensors, lab-on-a-chip and microfluidics platforms where graphene is in contact with water, vapor and analytes.¹⁻⁴ Although graphene was long believed to be a graphite-like material,⁵⁻⁷ some recent studies have shown a wide spread of water contact angle (CA),^{5,6,8-10} with values ranging from 10° when supported by water¹⁰ to 127° on solid substrates.⁵ One reason for such discrepancies in the values of the contact angle is the difference in sample preparation and measurement conditions.^{6,8} The adsorption of airborne hydrocarbons, the cleanliness and quality of the graphene/substrate and graphene/water interface can have significant effects on the measured contact angles, which, however, can be minimized in most cases by conducting experiments in controlled atmospheres and by avoiding the use of polymers during the transfer process.¹¹⁻¹⁴

The wetting characteristics of a material are dictated by both the surface and the bulk properties of the material, which implies the impossibility to determine the intrinsic wetting properties of two-dimensional (2D) materials which have no bulk. In other words, all wetting characteristics of graphene, such as contact angle and surface energy, refer not only to the graphene surface but also to the bulk phase underneath it and must not be regarded as solely graphene's properties.

In this respect, probing the wetting characteristics of free-standing graphene can give an indispensable insight for understanding the wettability of graphene. Yet, due to the extreme fragility of graphene and other 2D materials, studies on free-standing graphene have been limited to theoretical predictions with only a few experimental works on partially suspended graphene.^{15,16} Being the only experimental indication of the wettability of free-standing graphene up to now, the contact angle of partially suspended graphene is still an indirect measure and requires multistep sample preparation which may result in an ill-defined graphene-substrate interface yielding a range of contact angle values.

In this work the wettability of free-standing graphene is directly characterized using a simple and clean captive bubble methodology. The captive bubble method, i.e. the injection of an air bubble underneath graphene floating on water, allows for the formation of a graphene free-standing area as large as 1.5 by 1.5 mm, the largest free-standing area that has been reported so far for a 2D material. Essentially, graphene remains floating on the water surface after copper etching, intrinsically preventing any transfer or handling-related contamination and corrugation. An additional advantage is that the graphene side on which the contact angle is measured (i.e. the side that initially faces copper and then water) has never been exposed to ambient air and is therefore not subjected to airborne hydrocarbons adsorption.^{16,17}

4.2. Results

4.2.1. Captive bubble versus sessile drop

The captive bubble method measures the contact angle using an air bubble at a solid/liquid interface. Often, the method works best for hydrophilic substrates in which liquid spreads out yielding more difficulties to determine the contact angle with the sessile drop technique, e.g. for contact lenses and hydrogels.^{19,20} The captive bubble and sessile drop configurations represent the same three-phase equilibrium and, therefore, are equivalent in determining the contact angle values (Figure 4.1a, b).

The difficulties associated with the contact angle measurement on free-standing graphene are that 2D materials do not withstand the mechanical disturbances originating from – for example – depositing a droplet of liquid on their surface because of their extremely low thickness.¹⁰ Additionally, free-standing graphene as big as a macroscopic droplet does not exist. Instead, using the captive bubble geometry (i.e. a water-air bubble-graphene interface), allows for a reliable contact angle measurement. The advantage of this method in comparison to the sessile drop technique is that deionized water is primarily composed of water molecules (and therefore less contamination per volume percent compared to air

and vacuum; i.e., water protects graphene from airborne hydrocarbon contamination). Another remarkable advantage of the technique is that the bubble is saturated with water vapor, therefore yielding a contact angle in equilibrium in time.

For the comparison of the captive bubble method with the sessile drop technique the water contact angle was first measured on highly oriented pyrolytic graphite (HOPG). For that, HOPG was exfoliated with a scotch tape in air or in water depending on the method used for measuring the contact angle. The average contact angles were $59^{\circ}\pm 3^{\circ}$ for the sessile drop method and $60^{\circ}\pm 3^{\circ}$ for the captive bubble method (Figure 4.1 a, b). Both methods show high reproducibility on solid substrates.

Additionally, contact angles of graphene with a 300 nm layer of poly(methyl methacrylate) (PMMA) were measured using the captive bubble method and the sessile drop technique as control tests respectively. Graphene appeared wetting transparent in both cases displaying the contact angle of the bare PMMA support – that is $53^{\circ}\pm 4^{\circ}$ measured by the captive bubble method (Figure 4.1c) and $54^{\circ}\pm 3^{\circ}$ using the sessile drop method (Figure 4.1d). Noteworthy, after two days the graphene/PMMA sample became more hydrophobic and after six days the contact angle of graphene increased up to 85° (Figure 4.1d). Such transition from a hydrophilic to a hydrophobic surface is known to be caused by the adsorption of hydrocarbons from the air.¹¹ A surface energy analysis using the Owens-Wendt method (see Appendix 3) showed that while the graphene surface is clean, hydrocarbons tend to adsorb to minimize the free surface energy. The decrease of the total surface energy and its dispersive component is consistent with previous reports (Figure 4.1e).²¹

The agreement between the sessile drop and captive bubble results for freshly-exfoliated graphite and graphene/PMMA in which graphene was not exposed to air shows that, although the air in the bubble may contain hydrocarbon contaminants, they do not affect the contact angle because of the short-lived graphene-bubble contact and/or negligible amount of hydrocarbons present in the bubble.

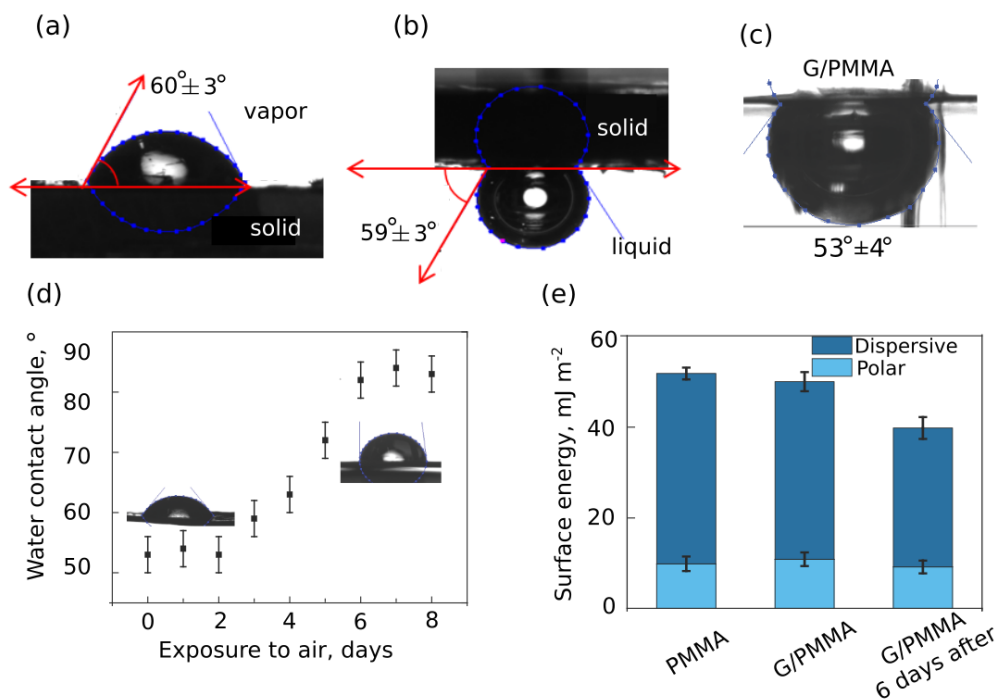


Figure 4.1. Sessile drop and captive bubble measurements on graphite and supported graphene. a) Sessile drop of water on freshly exfoliated highly oriented pyrolytic graphite (HOPG) in air. The measured contact angle is $60^\circ \pm 3^\circ$. The measurement was reproduced on ten samples and the error bar represents the standard deviation. b) Captive bubble configuration on freshly exfoliated HOPG in water. The measured contact angle is $59^\circ \pm 3^\circ$. The measurement was reproduced on ten samples and the error bar represents the standard deviation. c) Captive bubble measurement of water contact angle on graphene supported by a poly(methyl methacrylate) (PMMA) layer. The measurement was reproduced on ten samples and the error bar represents the standard deviation. d) Sessile drop contact angle measurement of graphene supported by a PMMA layer constantly exposed to air as a function of air exposure time. The measurement was reproduced on three samples and the error bar represents the standard deviation. e) Surface energies and polar and dispersive components of the surface energy for PMMA, graphene supported by PMMA and graphene supported by PMMA which was exposed to air for six days. The measurement was reproduced on three samples and the error bar represents the standard deviation.

4.2.2. Captive bubble method to study graphene. Inflection of floating graphene

For contact angle measurement on graphene using the captive bubble technique, an air bubble is deposited using an inverted needle underneath graphene (Figure 4.2a,b; for technical details on the sample preparation and contact angle measurements see Methods in Appendix 3). From the optical image one can see that the area of graphene surrounded by air on both sides is 1.5 by 1.5 mm large, the largest free-standing graphene area ever reported (Figure 4.2c).

However, due to its extreme flexibility and thinness, graphene inflects above the surface of water under the pressure of the air bubble and the inflection should be taken into account for the calculation of the contact angle. For flexible materials, forces at the three-phase contact line cannot be described by Young equation, as it is for flat rigid substrates. Instead, numerous investigations of the contact angle show that the force balance on soft materials is best described by Neumann's triangle.²²⁻²⁸ According to Neumann's theory the total contact angle on a deformed substrate can be described as a sum of two angles, beneath and above the contact line, i.e. $\theta_{\text{above}} + \theta_{\text{below}}$ (Figure 4.d). Since the angle measured in the captive bubble method is the contact angle between the air bubble and the solid, i.e. θ_{air} , the water contact angle should be recalculated as $180^\circ - \theta_{\text{air}}$. Taking into consideration the inflection of graphene, the contact angle of water on deflective graphene is therefore $180^\circ - (\theta_{\text{above}} + \theta_{\text{below}})$ (Figure 4.d).

The measurements of the contact angle of an air bubble on graphene, thus, are more complex than measuring the contact angle of a drop of water on graphene, and consist of measuring the contact angle measurement above and below the three-phase contact line. The schematics and optical image of an example of a water the contact angle measurement water on graphene are shown in Figure 4.2e and 4.2f respectively. The results show that graphene is hydrophilic with a contact angle of water of $42^\circ \pm 7^\circ$ (Figure 4.2f).

Interestingly, a smaller bubble causes a decrease of the measured angle $180^\circ - \theta_{\text{below}}$ and of the inflection angle θ_{above} , but the difference between the two, i.e. the actual contact angle, is independent of the bubble volume and equal to

$42^\circ \pm 3^\circ$: for a bubble volume of $6\mu\text{l}$, the resulting contact angle is 42° (i.e. the difference between the measured angle of 56° and the inflection angle of 14°), and for a bubble volume of $0.2\mu\text{l}$, the measured angle is 42° and there is no observable inflection to account for as the smaller bubble does not induce significant stretch in the graphene sheet (Figure 4.f, g). These observations are in agreement with other reported works and hypothesis that the size-dependence of the contact angle occurs only on rough and heterogeneous surfaces and not on smooth homogeneous surfaces like graphene.^{29–31}

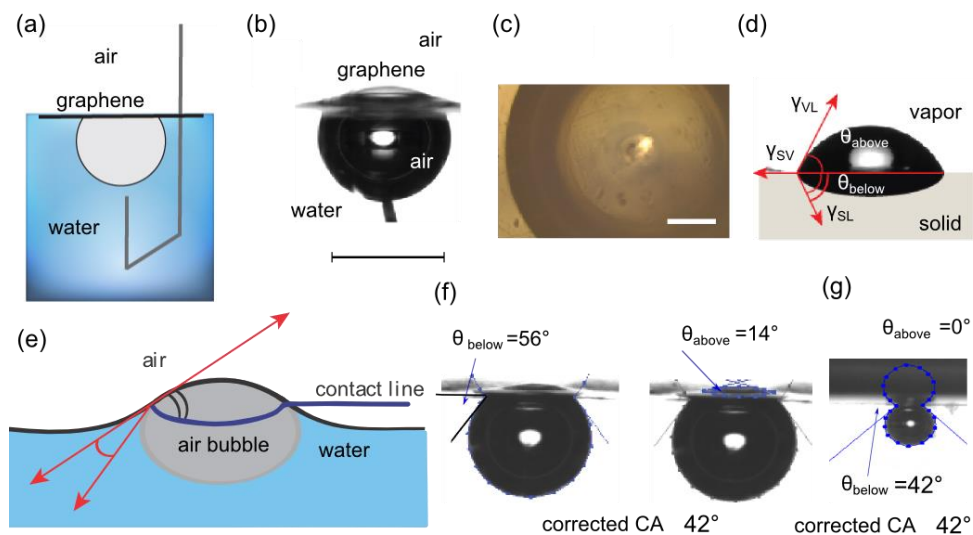


Figure 4.2. Captive bubble configuration for measuring the contact angle of water on free-standing graphene. a) Schematic illustration of the captive bubble setup for measuring the contact angle of water on free-standing graphene. b) Optical image of graphene on top of an air bubble (side view). Scale bar represents 2 mm. c) Optical image of graphene suspended above the air bubble (top view). Scale bar represents $500\mu\text{m}$. d) Geometry of the contact line on a soft elastic substrate. The contact angle of three phases is a sum of angles below (θ_{below}) and above (θ_{above}) the horizontal line. e) Neumann's triangle. Surface energy balance for captive bubble on graphene. f) Optical images of a captive bubble on graphene and calculation of the contact angle for an inflected graphene with an air bubble of $6\mu\text{l}$. g) Optical image of a captive bubble on graphene and calculation of the contact angle (bubble volume $0.2\mu\text{l}$)

4.2.3. Few-layer graphene and modified graphene

Multilayered graphene (bi- and four-layer) did not exhibit appreciable difference in the water contact angle (Figure 4.3a). Since defects and chemisorption of atomic hydrogen/oxygen on graphene are known to affect wetting,³² contact angles of graphene modified with H₂ and O₂ plasma were also measured (Figure 4.3a, see Methods in Appendix 3 for details on plasma treatment). After modification with H₂ plasma the contact angle on graphene-on-copper decreased from 76°±5° to 68°±5° which can be explained by the cleaning effect of the plasma (Raman characterization of graphene before and after the modification, Figure A3.3 in Appendix 3).^{33,34} No difference in the wettability of suspended graphene after the surface modification with a H₂ plasma was observed. Separately, an air bubble on graphene modified by a O₂ plasma was very unstable and tended to slip away from the graphene which could be explained by oxygen functionalities induced by the O₂ plasma.³⁵ Overall, contact angle values of modified and multilayer graphene are similar to the contact angle of monolayer pristine graphene given the error margins (Figure 4.a).

4.2.4. Effect of humidity

Recently graphene has been shown to turn hydrophilic when floating on water due to the wetting transparency effect.^{10,36} In order to test the effect of the environment on one side of graphene on its hydrophobicity on the other side, experiments under different humidities were performed. Contact angles of water using the captive bubble method were measured at the humidities of 98%, 85% and 50% regulated by saturated salt solution of K₂SO₄ and KCl (see Methods in Appendix 3 for more details).³⁷ Interestingly, a higher humidity level yields lower water contact angle: 29°±8° at 98%, 34°±7° at 85% and 42°±7° at 50% humidity (Figure 4.3b).

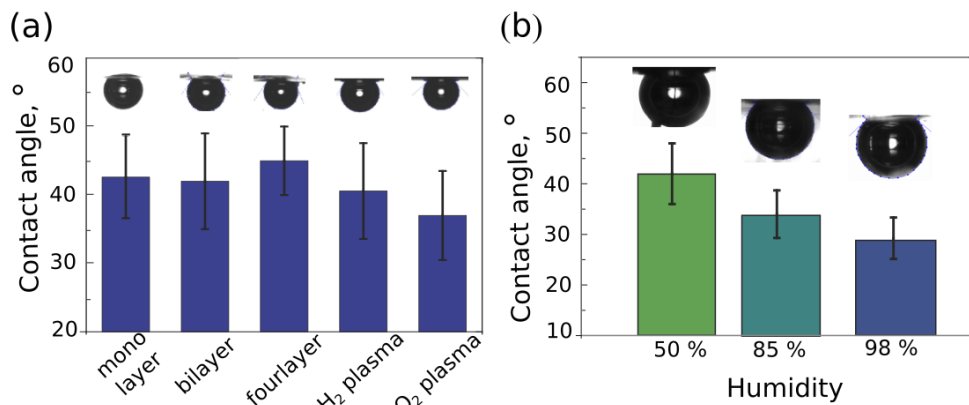


Figure 4.3. Graphene contact angles measured by the captive bubble method. a) Contact angles of water on free-standing, monolayer, bilayer, four-layer graphene and graphene modified with H₂ and O₂ plasma, measured using the captive bubble method. The measurement was reproduced on five samples and the error bar represents the standard deviation. b) Contact angle of water on free-standing graphene in 50%, 85% and 98% relative humidity. The measurement was reproduced on two samples and the error bar represents the standard deviation.

As for all microscopic approaches, the captive bubble method is technically challenging for studying 2D materials because they are fragile and even small vibrations can break them apart. In some cases cracks and holes appear on the graphene surface during the etching process¹⁵ which can prevent an air bubble from staying underneath the graphene. Furthermore, CVD (chemical vapor deposition) grown graphene is not monocrystalline and has grain boundaries which could make graphene permeable to air.^{38,39} In our experiments the air bubble underneath graphene was stable from two seconds up to fifteen minutes after which either the bubble or graphene would collapse (Figure A3.4 in Appendix 3 for optical images before and after the captive bubble experiment). The main sources of the degradation of graphene quality when floating on water were the high rate of copper etching, vibrations, intense air circulation and, partly as a result of all the aforementioned, movability of the graphene on the surface of water. In fact, the quality and stability of the floating graphene was significantly improved by using a less concentrated etchant solution of ammonium persulfate (0.3M and lower), or by minimizing vibrations and air circulations, and, importantly, immobilizing graphene with a lipid clamp (see

Methods in Appendix 3 for more details on the lipid clamp and sample preparation).⁴⁰

4.3. Discussion

Although partly suspended graphene on a texturized substrate shows hydrophobic properties with contact angle up to 85° ,^{15,16} our findings demonstrated that clean fully free-standing graphene is mildly hydrophilic (with a measured water contact angle of 42° , in agreement with theoretical predictions on the hydrophilicity of graphene with contact angle of water ranging from 37° to 44° ^{11,17,41}). However, such low contact angle is rather surprising, because given the wetting transparency of graphene^{9,10}, the contact angle of free-standing graphene should be identical to the contact angle of air, i.e. 180° . The wetting behavior, therefore, in this case cannot be only dictated by the transmission of air-water interactions, but is substantially affected by the phenomena occurring at the graphene surface. Remarkably, the measured contact angle values for mono-, bi-, four layer graphene and graphene treated with O_2 and H_2 plasma are similar (Figure 4.a), also supporting this assumption. The hydrophilicity of graphene (i.e., the fact that water wets free-standing graphene) could be explained by the formation of π -hydrogen bonding between water molecules and the aromatic system, as it is for benzene-water interaction.^{42,43} Another hypothesis attributes the hydrophilicity of graphene to the spontaneous adsorption of OH^- ions on graphene surfaces⁴⁴ which could lead to interactions with water and an increase of the repulsive double layer interaction between air (in the bubble) and graphene. As a complementary evidence for the hydrophilic behavior of graphene in water, stable surfactant-free dispersions of graphene have been recently obtained in degassed water.^{44,45} The apparent inability of graphene to form stable aqueous dispersions, which was previously attributed to the hydrophobicity of graphene, is now explained by the adsorption and further coalescence of nanobubbles on the graphene surface.

On the other hand, an increase in the environment humidity, i.e. the concentration of water molecules on the top side of graphene, leads to a decreasing water contact angle value and therefore an increase in the

hydrophilicity of graphene (Figure 4.b), indicating that the transparency of graphene to water-water interactions still has a substantial contribution in addition to the water-graphene interactions mentioned above.

In conclusion, a millimeter-sized suspended 2D material was obtained by simply harvesting surface tension forces at the air-water-graphene-air interface using an air bubble captivated on graphene floating on water. Direct contact angle measurements have shown that free-standing graphene has hydrophilic properties. Advantageously to other methods, the captive bubble technique allows to probe the water/graphene/air interface, in the cleanest way, avoiding any irregularities arising from the transfer and handling processes. The observed hydrophilicity could be explained by the formation of hydrogen bonds which would impact the spontaneous adsorption of water on the graphene surface. This work provides a stimulus to further study the still unexplored basic properties of suspended 2D materials, such as their surface chemistry, surface energy, compressive and flexural strength and device interaction at a millimeter scale in a free-standing geometry.

4.4. References

1. Shuo, S. *et al.* Graphene-based microfluidics for serial crystallography. *Lab Chip* **16**, 3082–3096 (2016).
2. Mirsaidov, U. *et al.* Scrolling graphene into nanofluidic channels. *Lab Chip* **13**, 2874–2878 (2013).
3. Chang, J., Zhou, G., Christensen, E. R., Heideman, R. & Chen, J. Graphene-based sensors for detection of heavy metals in water: a review. *Anal. Bioanal. Chem.* **406**, 3957–3975 (2014).
4. Dan, Y., Lu, Y., Kybert, N. J., Luo, Z. & Johnson, A. T. C. Intrinsic response of graphene vapor sensors. *Nano Lett.* **9**, 1472–1475 (2009).
5. Taherian, F., Marcon, V., Van Der Vegt, N. F. A. & Leroy, F. What is the contact angle of water on graphene? *Langmuir* **29**, 1457–1465 (2013).
6. Raj, R., Maroo, S. C. & Wang, E. N. Wettability of graphene. *Nano Lett.* **13**, 1509–1515 (2013).
7. Shin, Y. J. *et al.* Surface-energy engineering of graphene. *Langmuir* **26**, 3798–3802 (2010).
8. Wang, S., Zhang, Y., Abidi, N. & Cabrales, L. Wettability and surface free energy of graphene films. *Langmuir* **25**, 11078–11081 (2009).
9. Rafiee, J. *et al.* Wetting transparency of graphene. *Nat. Mater.* **11**, 217–222 (2012).
10. Belyaeva, L. A., van Deursen, P. M. G., Barbetsea, K. I. & Schneider, G. F. Hydrophilicity of graphene in water through transparency to polar and dispersive interactions. *Adv. Mater.* **30**, 1–7 (2018).
11. Li, Z. *et al.* Effect of airborne contaminants on the wettability of supported graphene and graphite. *Nat. Mater.* **12**, 925–931 (2013).
12. Kozbial, A., Gong, X., Liu, H. & Li, L. Understanding the Intrinsic Water Wettability of Molybdenum Disulfide (MoS₂). *Langmuir* **31**, 8429–8435 (2015).
13. Kozbial, A., Zhou, F., Li, Z., Liu, H. & Li, L. Are graphitic surfaces hydrophobic? *Acc. Chem. Res.* **49**, 2765–2773 (2016).

14. Aria, A. I. *et al.* Time evolution of the wettability of supported graphene under ambient air exposure. *J. Phys. Chem. C* **120**, 2215–2224 (2016).
15. Ondarçuhu, T. *et al.* Wettability of partially suspended graphene. *Sci. Rep.* **6**, 24237 (2016).
16. Zhao, Y. *et al.* Investigations on the wettability of graphene on a micron-scale hole array substrate. *RSC Adv.* **6**, 1999–2003 (2016).
17. Yiapanis, G., Makarucha, A. J., Baldauf, J. S. & Downton, M. T. Simulations of graphitic nanoparticles at air-water interfaces. *Nanoscale* **8**, 19620–19628 (2016).
18. Li, J. & Wang, F. Water graphene contact surface investigated by pairwise potentials from force-matching PAW-PBE with dispersion correction. *J. Chem. Phys.* **146**, (2017).
19. Read, M. L., Morgan, P. B., Kelly, J. M. & Maldonado-Codina, C. Dynamic contact angle analysis of silicone hydrogel contact lenses. *J. Biomater. Appl.* **26**, 85–99 (2011).
20. Lin, M. C. & Svitova, T. V. Contact lenses wettability in vitro: effect of surface-active ingredients. *Optom. Vis. Sci.* **87**, 440–447 (2010).
21. Kozbial, A. *et al.* Study on the surface energy of graphene by contact angle measurements. *Langmuir* **30**, 8598–606 (2014).
22. Style, R. W. *et al.* Universal deformation of soft substrates near a contact line and the direct measurement of solid surface stresses. *Phys. Rev. Lett.* **110**, 1–5 (2013).
23. Lubbers, L. A. *et al.* Drops on soft solids: free energy and double transition of contact angles. *J. Fluid Mech.* **747**, (2014).
24. Metois, J. J. Elastic straining of a thin graphite layer by a liquid droplet or a non-epitaxed Pb crystallite. *Surf. Sci.* **241**, 279–288 (1991).
25. Jerison, E. R., Xu, Y., Wilen, L. A. & Dufresne, E. R. Deformation of an elastic substrate by a three-phase contact line. *Phys. Rev. Lett.* **106**, 1–4 (2011).
26. Hui, C.-Y. & Jagota, A. Deformation near a liquid contact line on an elastic substrate. *Proc. R. Soc. A Math. Phys. Eng. Sci.* **470**, 20140085 (2014).

27. Style, R. W. & Dufresne, E. R. Static wetting on deformable substrates, from liquids to soft solids. *Soft Matter* **8**, 7177–7184 (2012).
28. Nadermann, N., Hui, C.-Y. & Jagota, A. Solid surface tension measured by a liquid drop under a solid film. *Proc. Natl. Acad. Sci.* **110**, 10541–10545 (2013).
29. Drelich, J., Miller, J. D. & Good, R. J. The effect of drop (bubble) size on advancing and receding contact angles for heterogeneous and rough solid surfaces as observed with sessile-drop and captive-bubble techniques. *J. Colloid Interface Sci.* **179**, 37–50 (1996).
30. Drelich, J. The effect of drop (bubble) size on contact angle at solid surfaces. *J. Adhes.* **63**, 31–51 (1997).
31. Drelich, J. & Miller, J. D. The effect of surface heterogeneity on pseudo-line tension and the flotation limit of fine particles. *Colloids and Surfaces* **69**, 35–43 (1992).
32. Xu, Z. *et al.* Reversible hydrophobic to hydrophilic transition in graphene via water splitting induced by UV irradiation. *Sci. Rep.* **4**, 6450 (2015).
33. Russo, C. J. & Passmore, L. A. Controlling protein adsorption on graphene for cryo-EM using low-energy hydrogen plasmas. *Nat. Methods* **11**, 649–652 (2014).
34. Jiang, L., Fu, W., Birdja, Y. Y., Koper, M. T. M. & Schneider, G. F. Quantum and electrochemical interplays in hydrogenated graphene. *Nat. Commun.* **9**, 793 (2018).
35. Mcevoy, N., Nolan, H., Nanjundan, A. K., Hallam, T. & Duesberg, G. Functionalization of graphene surfaces with downstream plasma treatments. *Carbon N. Y.* **54**, 283–290 (2013).
36. Driskill, J., Vanzo, D., Bratko, D. & Luzar, A. Wetting transparency of graphene in water. *J. Chem. Phys.* **141**, 18C517 (2014).
37. Greenspan, L. Humidity fixed points of binary saturated aqueous solutions. *J. Res. Natl. Bur. Stand. Sect. A Phys. Chem.* **81A**, 89 (1977).
38. Huang, P. Y. *et al.* Grains and grain boundaries in single-layer graphene atomic patchwork quilts. *Nature* **469**, 389–392 (2011).

39. Yu, Q. *et al.* Control and characterization of individual grains and grain boundaries in graphene grown by chemical vapour deposition. *Nat. Mater.* **10**, 443–449 (2011).
40. Lima, L. M. C., Arjmandi-Tash, H. & Schneider, G. F. Lateral non-covalent clamping of graphene at the edges using a lipid scaffold. *ACS Appl. Mater. Interfaces* **10**, 11328–11332 (2018).
41. Andrews, J. E., Sinha, S., Chung, P. W. & Das, S. Wetting dynamics of a water nanodrop on graphene. *Phys. Chem. Chem. Phys.* **18**, 23482–23493 (2016).
42. Sakae Suzuki, Peter G. Green, R. E. B. & Siddharth Dasgupta, William A. Goddard III, G. A. B. Benzene forms hydrogen bonds with water. **257**, 942–944 (1992).
43. Gierszal, K. P. *et al.* π -hydrogen bonding in liquid water. *J. Phys. Chem. Lett.* **2**, 2930–2933 (2011).
44. Bepete, G. *et al.* Surfactant-free single-layer graphene in water. *Nat. Chem.* **9**, 347–352 (2016).
45. Ricardo, K. B., Sendekci, A. & Liu, H. Surfactant-free exfoliation of graphite in aqueous solutions. *Chem. Commun.* **50**, 2751–2754 (2014).

CHAPTER 5

Hydrophilicity of graphene in water through transparency to polar and dispersive interactions

Establishing contact angles on graphene-on-water has been a long-standing challenge as droplet deposition causes free-floating graphene to rupture. In this chapter ice and hydrogels are used as substrates mimicking water while offering a stable support for graphene. The lowest water contact angles of graphene were measured, namely on graphene-on-ice and graphene-on-hydrogel. The contact angle measurements of liquids with a range of polarities allowed to quantify the transparency of graphene towards polar and dispersive interactions demonstrating that graphene in water is hydrophilic. These findings are anticipated to shed light on the inconsistencies reported so far on the wetting properties of graphene, and most particularly on their implications towards rationalizing how molecules interact with graphene in water.

This chapter was published as an article: Liubov A. Belyaeva, Pauline M.G. van Deursen, Kassandra I. Barbetsea, Grégory F. Schneider Adv. Mater. 2018, 30, 1703274

5.1. Introduction

The wetting properties of graphene are more complicated than those found in regular solid-liquid interfaces because graphene possesses no bulk phase and is only composed of a single atomic layer of carbon atoms separating two liquid media. Graphene is therefore subjected to a complexity of nonspecific interactions with adsorbates – primarily induced by wetting transparency – at the substrate-graphene-liquid and liquid-graphene-liquid interfaces.¹

Wetting transparency, opacity, hydrophilicity and hydrophobicity of graphene remain under debate. Intensive recent studies on the wetting transparency of graphene suggested that the wettability of graphene is governed by the wettability of the underlying support.¹⁻³ Other studies report complete wetting transparency of graphene when deposited on gold, copper and silicon, but not glass, where interactions with water are considered short-range². A later experimental work supported by molecular dynamics simulations suggests partial transparency of graphene and indicates that wetting transparency does not occur for superhydrophilic or superhydrophobic substrates,³ and number of papers suggest full wetting opacity of monolayer graphene irrespective of the substrate, with contact angle values similar to water contact angle on graphite.⁴⁻⁶ Consequently, contact angle values of water on graphene vary from 33° for graphene on silicon² to 90-127° for graphene respectively on silicon carbide, silicon oxide and copper⁴⁻⁷ despite a large number of theoretical studies suggesting that water contact angle values on graphene should be similar to the one of graphite.^{1,4,6} So far, the several contradictions and inconsistencies have partially been explained by the presence of adsorbates, graphene defects and surface charges.^{8,9}

Concerning the wetting properties of graphene in water, the direct measurement of the contact angle of water on graphene-on-water – i.e., depositing a droplet of water on graphene floating on water – has been technically impossible due to the immediate rupture of the graphene upon droplet deposition (Figure 5.1a, b) resulting from the growth- and handling-induced cracks and tears.¹⁰⁻¹³ Probing wetting properties of graphene in water and water solutions is, however, particularly important for application in sensing, water filtration, fuel cell membranes and more generally when graphene is exposed to water from the

both sides.^{1,14-16} This chapter shows that graphene is surprisingly hydrophilic when floating on water. Additionally, by changing the polarity of the liquid used to measure contact angles (both of the drop and of the solution), the surface energy of graphene was calculated indicating that monolayer graphene is transparent to both polar and dispersive interactions – i.e. fully transparent to wetting – with the condition that a smooth substrate/graphene/liquid interface free of contamination is obtained. In the contrary case – that is when graphene is physically transferred from the growth substrate to another support – graphene usually does not conform perfectly the target substrate resulting in the screening of short-range polar interactions while long-range dispersion interactions are fully transmitted. The latter often occurs in scenarios where graphene is transferred with the use of a polymer yielding surface corrugations, wrinkles, contamination, large sample-to-sample variations and immense discrepancies in the contact angles measurements.

5.2. Results and discussions

To quantify the hydrophobicity of graphene and to rationalize its wetting properties, ice and hydrogels can be used as models of liquid water. In fact, the water molecules at the surface of ice are in a supercooled liquid state retaining an amorphous liquid-like structure.¹⁷⁻²¹ Separately, a low weight percent hydrogel has a low surface concentration of polymer chains relative to that of interstitial water and, for that reason, has been used as a quasi-solid model for water surface properties since the sixties.^{22,23} By experimentally measuring the contact angle of water on floating graphene, the lowest contact angle reported for graphene so far were observed: $30\pm 5^\circ$ on ice and $10\pm 2^\circ$ on a 4 w% agarose hydrogel.

Importantly, the cleanliness of the graphene surface and of the graphene-substrate interface are critical factors for a reliable contact angle measurement and great care should be taken for the handling of graphene. For details on the cleaning procedure (e.g. from polymer residuals or hydrocarbon adsorbates), including handling and control measurements, see Appendix 4.

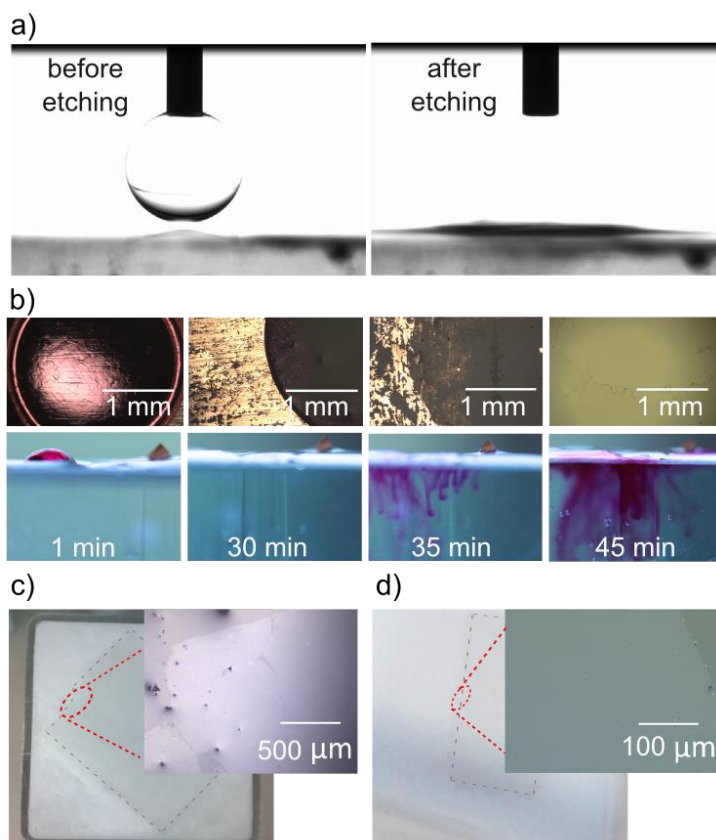


Figure 5.1. Graphene free-floating on liquid water, ice and hydrogels. a) Water contact angle (WCA) measurements of graphene floating on a water surface. Left: water droplet before being deposited on the surface of CVD-graphene floating on an aqueous solution of copper etchant. Right: a water droplet after being deposited on the surface of graphene sinks through the graphene, preventing the measurement of the contact angle. The rupture and consequent breaking of the graphene is also seen in the case of pure water instead of APS solution. b) Time lapse photographs of a water droplet sinking through a graphene/copper stack floating on the surface of an aqueous solution of ammonium persulfate (copper etchant) as a function of copper etching time (from left to right). Photographs were taken from the top of the droplet (top images) and from the side (bottom images). The water droplet was dyed with Rhodamine B for optimal visualization. c) Photograph and optical microscopy image (inset) of a monolayer of graphene on ice. d) Photograph and optical microscopy image (inset) of a monolayer of graphene on a 4% agarose hydrogel.

5.2.1. Graphene is hydrophilic in an aqueous environment

Investigating the wetting properties of graphene suspended on a liquid poses a critical challenge: although intact graphene floats well on water – presenting a graphene-on-water surface – the contact angle of such a surface cannot be measured (and has never been measured) because free-floating graphene immediately breaks apart when a droplet of water is casted onto the graphene top surface, inducing excessive mechanical and interfacial stress resulting in cracking and tearing of graphene, causing the water to leak out via the formed microcracks (Figure 5.1a). Those microcracks might result from the growth,^{10,11,13} during copper etching^{10–12} or simply under the droplet pressure. The water droplet therefore sinks through graphene even if the droplet is deposited before copper is completely etched away, i.e. when the dynamic stress in graphene is minimized (Figure 5.1b). To overcome this limitation and to probe the wetting properties of graphene in water, liquid water underneath graphene was replaced with water ice and an agarose hydrogel (Figure 5.1c and 5.1d). These systems are especially benign to graphene as they avoid using a protective polymer (usually PMMA) layer that always yields contamination such as polymer residues.

5.2.2. Ice as a model for water

Graphene grown by CVD on copper (see Methods for details) is placed on the surface of an aqueous solution of 0.5 M ammonium persulfate (APS), which serves as a copper etchant. After cool-down and the solidification of water, the contact angle of a droplet of water deposited on graphene-on-ice was measured. To prevent condensation, the chamber was flushed with dry air during the entire process of water freezing and measurements. Another possible source of inaccuracy in measurements is strain in graphene that may be induced upon freezing of water. However, later in this chapter it will be shown that it does not affect the wetting transparency, as in the case of strain no significant change in graphene-ice distance occurs to screen the interactions. The contact angle and surface energy of graphene on ice were found to be very close to those of bare ice.

Remarkably, the water contact angle (WCA) on graphene-on-ice at 0°C is $30^{\circ} \pm 5$ which is only 13° greater than the water contact angle of pure ice and 30° smaller than the water contact angle of freshly exfoliated graphite (see Figure 5.2a). Repeating the experiment with double layer graphene increases the WCA to 35° on average. At -20°C the WCA also showed a similar hydrophilic behavior of graphene when deposited on ice (see Figure 5.2a). To prevent the water droplet from instant freezing at the moment of its deposition on graphene, 18% of nitric acid was added (see Methods in Appendix 4), yielding slightly smaller contact angles compared to experiments carried at 0°C due to the increase in the polarity of the liquid droplet: $11^{\circ} \pm 3$ for ice, $18^{\circ} \pm 4$ for monolayer graphene on ice, $34^{\circ} \pm 5$ for bilayer graphene on ice and $57^{\circ} \pm 2$ for graphite. To take into consideration the effect of added nitric acid on the contact angle and on the surface energy the approach typically used for an electrolyte solution was followed (experimental details and calculations of the surface energy can be found in Appendix 4). One and two layers of graphene, therefore, transmit major portion of water-water interactions, although the bilayer is less hydrophilic and screens a noticeable part of the interactions due to the increased thickness.

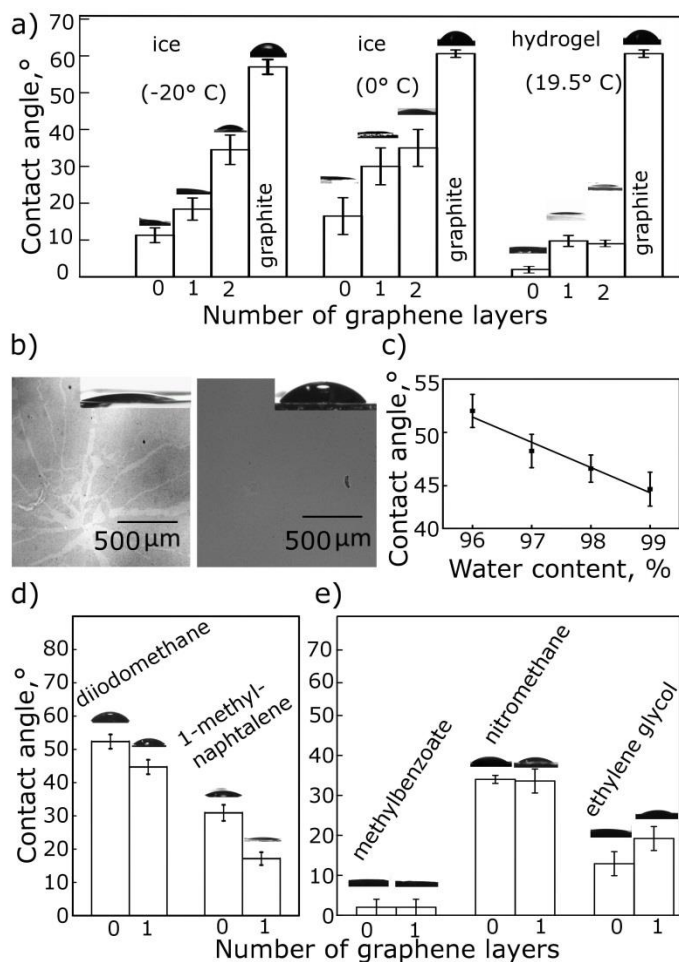


Figure 5.2. Contact angles of graphene on ice and hydrogel. a) Water contact angle (WCA) of graphene-on-ice measured at -20°C, 0°C and for graphene on a 4% agarose hydrogel measured at 19.5°C. WCA were measured for bare ice/hydrogel, monolayer graphene and bilayer graphene. b) Contact angle photographs (insets) and optical microscopy images of the graphene after drop-casting water (left) and diiodomethane (right) on top of graphene floating on a 4% agarose hydrogel. The process of drop-casting a droplet of water typically causes graphene to crack while drop-casting of an organic liquid leaves no visible mechanical damages on graphene. c) Hydrogel as a water model: diiodomethane contact angle values for an agarose hydrogel with different water content. d) Contact angles of graphene on a 4% agarose hydrogel with diiodomethane and 1-methylnaphtalene as liquid droplets. e) Contact angle values of graphene on ice with methylbenzoate, nitromethane and ethylene glycol.

Although the properties of ice differ from the properties of liquid water, the surface of ice stays in a supercool state and retain amorphous liquid-like structure,^{17–21} which makes ice with graphene on top a reasonable approximation of free-floating graphene on water.

5.2.3. Hydrogel as a model of water

In the graphene-hydrogel system developed for contact angle measurements, CVD graphene grown on copper was supported by a 4% agarose gel network.²⁴

Graphene on hydrogel is hydrophilic, with a contact angle of $10 \pm 2^\circ$ for single layer graphene. Optical microscopy images of graphene on hydrogel after contact angle measurement with water (left) and diiodomethane (right) are shown in Figure 5.2b. The micrographs show that multiple cracks have formed after the deposition of a water droplet (Figure 5.2b, left) while an intact surface is preserved during the deposition of organic liquids (Figure 5.2b, right). The cracking under the influence of water is attributed to the strong interactions between water underneath graphene and water in the droplet. Despite the appearance of cracks, no water leaks away into the gel, as water droplets attain a stable shape within three seconds after drop deposition – during which the droplet spreads out. Moreover, the graphene coverage, despite the presence of cracks, was still well above 95%, with no noticeable cracks on the periphery of the droplet. Analogous crack analysis was not possible for ice samples due to technical limitations: because the sample has to be cooled down the liquid droplet does not evaporate after the contact angle measurement, rendering impossible to inspect the surface of ice using a microscope.

By measuring contact angles of water-immiscible solvents on hydrogels with a range of agarose concentrations, a linear extrapolation was made to 100% water.²² Figure 5.2c shows the linear extrapolation of the contact angle of diiodomethane on an agarose hydrogel with agarose concentrations range from 1 to 4% agarose in weight (see Figure A4.7 in Appendix 4 for the extrapolation with 1-methylnaphtalene). From the extrapolation, the contact angle of diiodomethane on water would be 41° . Conversely, such data cannot be gathered

for graphene-on-hydrogel, because graphene relies on a high (4%) agarose concentration for mechanical support.

In summary, two independent experiments have proven that when placed in a water-like environment, graphene, surprisingly, presents hydrophilic properties very close to those of pure water, i.e. graphene is transparent to water-water interactions. Studying only graphene-water interactions, however, is not sufficient for understanding graphene wetting properties and claiming its wetting transparency.

For that reason contact angle measurements with other liquids possessing different polarities were performed (Table A4.1 in Appendix 4). With all probed liquids, graphene-on-ice and graphene-on-hydrogel showed contact angle similar to the contact angles on pure ice and pure hydrogel respectively (Figure 5.2d and e). Contact angles with organic liquids seem to be more reliable than those with water, as no damage to the graphene structure occurs during the measurement (see Figure 5.2b for comparison). The damage that typically occurs for measurements with water can result from very strong water-water interactions between the water molecules across the graphene sheet.

5.2.4. Selective screening of polar interactions by graphene: Is graphene transparent to wetting?

To explain the inconsistencies reported in literature on the contact angle of graphene, it is logical to question whether the great variety of WCA reported for graphene results from the fact that graphene transmits only a part of the interactions between the substrate and the liquid. In that case, transparency or opacity of graphene to wetting would be determined by the dominating type of interactions between the molecules constituting the droplet and the substrate, and its transmission through a graphene layer. Depending on the chemical nature of the adsorbate and adsorbent, all intermolecular interactions can be divided into two main groups: site-specific *polar* (hydrogen bonding, dipole-dipole, and dipole-induced interactions) and nonspecific *dispersive* interactions (London - van der Waals interactions)^{25,26}. Polar interactions appear whenever the electron density or a positive charge are localized along the bonds; and dispersive

interactions appear due to instantaneous dipole moments of all atoms and molecules and, therefore, are always present regardless of the chemical nature of the interacting molecules. These two types of interactions can be quantified in terms of surface energy components.^{26,27} According to the Owens-Wendt²⁶ or Fowkes²² theory, the total surface tension of a liquid or a solid can be represented as a sum of polar and dispersive components corresponding to polar and dispersive interactions:

$$\begin{aligned}\sigma_L &= \sigma_L^P + \sigma_L^D \\ \sigma_S &= \sigma_S^P + \sigma_S^D\end{aligned}$$

and all four components can be linked with each other by the Owens-Wendt equation:

$$\frac{\sigma_L(\cos\theta + 1)}{2\sqrt{\sigma_L^D}} = \frac{\sqrt{\sigma_S^P}\sqrt{\sigma_L^P}}{\sqrt{\sigma_L^D}} + \sqrt{\sigma_S^D}$$

Calculating the surface energies using the Fowkes model^{22,27} yielded a good agreement with the surface energies obtained using the Owens-Wendt model (see Figure A4.12 in Appendix 4). Detailed calculations of surface energies by Owens-Wendt theory and results of the Fowkes calculations can be found in Appendix 4.

Probing contact angles of liquids with different polarities allowed to determine polar σ_S^P and dispersive σ_S^D components of the solid and to identify the character of the interactions between the droplet and the solid.²⁶ The variation of the σ_S^P and σ_S^D caused by the addition of the graphene layer was examined in order to elucidate what interactions are transmitted or screened by the graphene and to what extent. Water, diiodomethane and 1-methylnaphthalene were chosen because of their compatibility with the hydrogel matrix. Their polar and dispersive components are tabulated (see Table A4.1 in Appendix 4). More in details: water, methyl benzoate, nitromethane and ethylene glycol were chosen as test liquids for ice due to their low freezing points and known polar and dispersive components; and water, diiodomethane, formamide, nitromethane and methyl benzoate were chosen for Si/SiO₂, polydimethylsiloxane (PDMS) and copper (Table A4.1 in Appendix 4).

Separately, three types of substrates possessing three distinct surface free energies were chosen: substrates with dominating polar component (i.e., ice and hydrogel), substrates with similar polar and dispersive components (i.e., Si/SiO₂ wafers and PDMS), and a substrate with dominating dispersive component (i.e., copper). Importantly, because graphene has not been transferred on copper, ice and hydrogel (see Methods for the details on the samples preparation), graphene conforms the surface of the substrates allowing for a perfect adhesion.²⁸ Contrarily, graphene being transferred from copper does not conform as effectively the PDMS surface and possesses multiple out-of-plane irregularities such as wrinkles, bucklings and foldings,^{29,30} resulting in a larger graphene-substrate separation and, consequently, poorer adhesion.²⁸

As shown in Figure 5.2, graphene does not alter contact angles of all tested liquids when deposited on top of copper, ice or hydrogel and, consequently, transmits both polar and dispersive interactions (Figure 5.3). Important to note, that an increase in the number of graphene layers results in poorer reproducibility due to contamination, defect formation, and uncontrollable interlayer distance occurring during the transfer of the layers on top of each other (the multilayer samples were purchased from Graphenea, and are prepared by repetitively transferring graphene layers on top of each other). The error margins are therefore wider for bilayer graphene than those for monolayer graphene, and error margins for three- and four- layer graphene did not allow making a conclusion on the average contact angle value (see Figure A4.9 in Appendix 4). Importantly, in all cases graphene showed contact angles different from the contact angle of freshly-exfoliated (to avoid airborne hydrocarbons contamination) graphite measured to be $61\pm 3^\circ$ which is consistent with previously reported values.^{8,31-33}

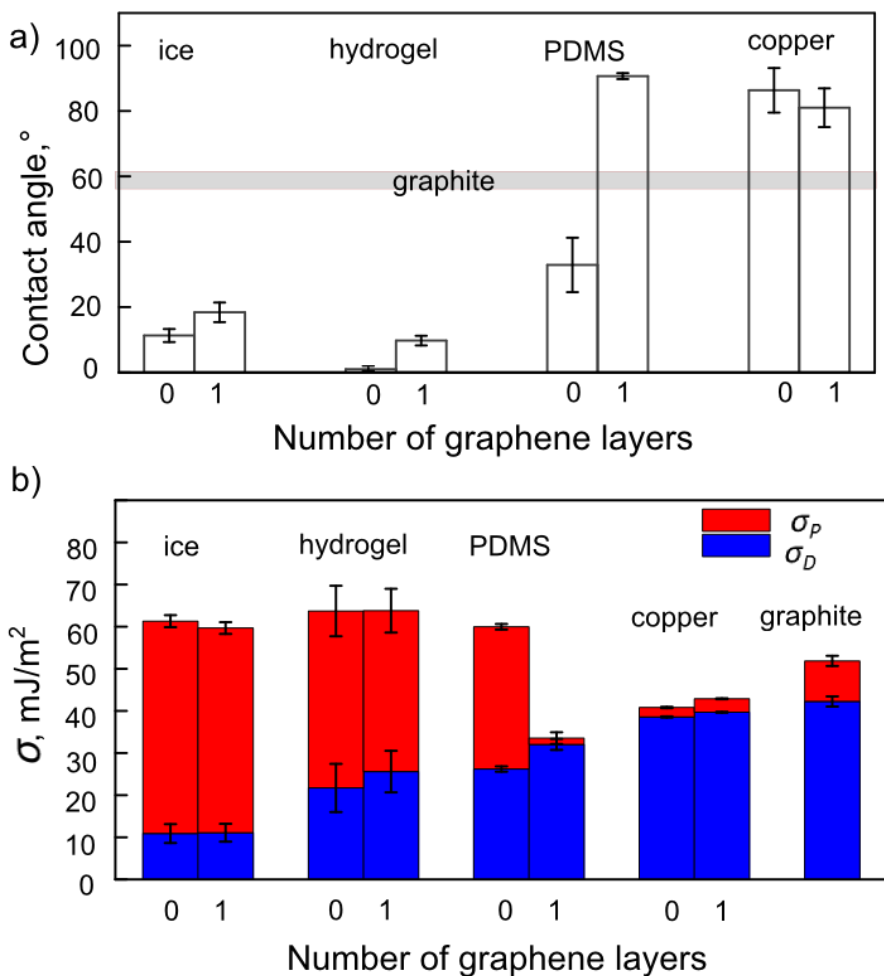


Figure 5.3. Water contact angle values and surface energy of graphene on different substrates compared to bare substrates. a) Water contact angle (WCA) of graphene deposited on ice (-20°C), hydrogel (19.5°C), PDMS (19.5°C) and copper (19.5°C) versus WCA of pristine ice, hydrogel, PDMS and copper. b) Polar and dispersive components of the surface energy of graphene deposited on ice, hydrogel, PDMS and copper versus pristine ice, hydrogel, PDMS and copper. The polar and dispersive components of the surface energy were calculated using the Owens-Wendt theory.

The transparency effect for ice, hydrogel and copper is even more evident from the surface energy chart (Figure 5.3b). Surface energy calculations are based on the contact angle measurements with various liquids and are, in that respect, a

more comprehensive characteristic of the interactions than a contact angle measurement. Notably, the total surface energy of graphene supported by a substrate is different from the total surface energy of graphite ($52 \pm 2 \text{ mJ/m}^2$) for all tested substrates and equals to the surface energy of the bare substrate itself with the only exception of PDMS, as shown in Figure 5.3b ($\sim 60 \text{ mJ/m}^2$ for ice, $\sim 64 \text{ mJ/m}^2$ for hydrogel and $\sim 43 \text{ mJ/m}^2$ for copper). Thus, although graphene is often considered as a graphite-like material and expected to have graphite-like wetting behavior and surface energy,^{5,7,8} clearly, its surface energy and wetting properties are governed by the bulk medium underneath. Furthermore, the presence of graphene does not affect the distribution of polar and dispersive forces between the molecules of adsorbate and adsorbent for all types of substrates (the case of PDMS will be discussed further below). Noteworthy, surface energies and polar and dispersive components of the surface energies of ice, graphene-on-ice, hydrogel and graphene-on-hydrogel are all very close to those of pure water, which indicates that ice and hydrogels are suitable as water models for probing wetting properties of graphene in water.

As opposed to graphene-on-ice, graphene-on-hydrogel or graphene-on-copper, graphene transferred onto a Si/SiO₂ wafer or onto a PDMS slab showed significantly different wetting properties than the substrate underneath it (Figure 5.3a and Figure A4.10 in Appendix 4). Moreover, measurements for graphene on Si/SiO₂ (but not for bare Si/SiO₂ wafers, which were reproducible) were highly irreproducible with all tested liquids with water contact angles varying from 40° to 90° (Figure A4.10 in Appendix 4) and were therefore not included in the present analysis. This can be attributed to the different graphene-substrate adhesion forces that result from sample-to-sample variation occurring during the transfer process. Although electronic properties of graphene on Si/SiO₂ are well defined in literature, contamination and even subtle alterations of adhesion forces - which have minor effects on the electronic properties - can crucially affect the wetting properties of graphene.

Transfer of graphene to PDMS is more straightforward and, importantly, does not involve coverage of graphene with another polymer than PDMS, permitting reproducible contact angle measurements (see Methods in Appendix 4 for more details on the transfer). After transferring graphene onto PDMS the water contact angle increased from $33 \pm 5^\circ$ to $91 \pm 1^\circ$ (see Figure 5.3a) and the total

surface energy decreased from 60 ± 1 mJ/m² to 34 ± 1 mJ/m² (Figure 5.3b). The polar component dropped drastically from 34 ± 1 mJ/m² to 2 ± 1 mJ/m², whereas the dispersive component remained almost unchanged at 26 ± 1 mJ/m². Given the full transparency of graphene to the both types of interactions for “well-conforming” substrates, the selective screening of the polar interactions therefore originates from the mismatch in conformation between the surface of graphene and PDMS caused by the transfer process. The lack of conformity between a substrate and graphene transferred on top of it has been independently proven by the AFM analysis of the surface morphology of PDMS with and without graphene (Figure A4.2 in Appendix 4). Graphene transferred to PDMS rather represents the roughness pattern of copper than of PDMS which results in conformational mismatch and breakdown of the wetting transparency of graphene (Figure A4.2 in Appendix 4). Polar interactions are short-range and, therefore, evanesce upon increasing the adsorbate-adsorbent distance whereas long-range dispersion interactions can still be fully transmitted.^{34–37} This implies that the observed polar component of 2 ± 1 mJ/m² can be attributed to the inherent polar component of graphene.

Noteworthy, to exclude the influence of adsorbed contaminants from air,⁸ samples of graphene on copper and Si/SiO₂ were annealed before the measurements (see Appendix 4 for more details).

5.3. Conclusions

The mechanical fragility of a single layer of graphene floating on the surface of water has prevented so far to probe the surface hydrophilicity by means of contact angle measurements. Contact angle measurements of graphene on water ice and on hydrogels show that graphene is hydrophilic and transparent to water-water interactions. Importantly, the interface between the graphene layer and underlying substrate plays an important role: graphene transmits polar and dispersive interactions if the graphene-substrate interface is clean and not corrugated, otherwise polar interactions are screened while dispersive interactions are transmitted. In applications where graphene is suspended between two liquids, these results now shed light and propose a radically

different understanding of the wetting properties of graphene and will have prompt implications in understanding how hydrophobic and hydrophilic molecules interact with the surface of a two-dimensional material subjected to full wetting transparency. This work might also inspire several research communities to (re)consider how hydrophilicity and hydrophobicity of two-dimensional materials and molecules are defined.

5.4. References

1. Driskill, J., Vanzo, D., Bratko, D. & Luzar, A. Wetting transparency of graphene in water. *J. Chem. Phys.* **141**, 18C517 (2014).
2. Rafiee, J. *et al.* Wetting transparency of graphene. *Nat. Mater.* **11**, 217–222 (2012).
3. Shih, C. J. *et al.* Breakdown in the wetting transparency of graphene. *Phys. Rev. Lett.* **109**, 1–5 (2012).
4. Taherian, F., Marcon, V., Van Der Vegt, N. F. A. & Leroy, F. What is the contact angle of water on graphene? *Langmuir* **29**, 1457–1465 (2013).
5. Shin, Y. J. *et al.* Surface-energy engineering of graphene. *Langmuir* **26**, 3798–3802 (2010).
6. Raj, R., Maroo, S. C. & Wang, E. N. Wettability of graphene. *Nano Lett.* **13**, 1509–1515 (2013).
7. Wang, S., Zhang, Y., Abidi, N. & Cabrales, L. Wettability and surface free energy of graphene films. *Langmuir* **25**, 11078–11081 (2009).
8. Li, Z. *et al.* Effect of airborne contaminants on the wettability of supported graphene and graphite. *Nat. Mater.* **12**, 925–931 (2013).
9. Ghaderi, N. & Peressi, M. First-principle study of hydroxyl functional groups on pristine, defected graphene, and graphene epoxide. *J. Phys. Chem. C* **114**, 21625–21630 (2010).
10. Arjmandi-Tash, H., Jiang, L. & Schneider, G. F. Rupture index: A quantitative measure of sub-micrometer cracks in graphene. *Carbon N. Y.* **118**, 556–560 (2017).
11. Belyaeva, L. A., Fu, W., Arjmandi-Tash, H. & Schneider, G. F. Molecular caging of graphene with cyclohexane: transfer and electrical transport. *ACS Cent. Sci.* **2**, 904–909 (2016).
12. Gao, L. *et al.* Face-to-face transfer of wafer-scale graphene films. *Nature* **505**, 190–194 (2014).
13. Hwangbo, Y. *et al.* Fracture characteristics of monolayer CVD-graphene. *Sci. Rep.* **4**, 4439 (2015).

14. Postma, H. W. C. Rapid sequencing of individual DNA molecules in graphene nanogaps. *Nano Lett.* **10**, 420–425 (2010).
15. Arjmandi-Tash, H., Belyaeva, L. A. & Schneider, G. F. Single molecule detection with graphene and other two-dimensional materials: nanopores and beyond. *Chem. Soc. Rev.* **45**, 476–493 (2016).
16. Cohen-Tanugi, D. & Grossman, J. C. Water desalination across nanoporous graphene. *Nano Lett.* **12**, 3602–3608 (2012).
17. Faraday, M. On certain conditions of freezing water. *Athenaeum* 283–284 (1850).
18. Elbaum, M., Lipson, S. G. & Dash, J. G. Optical study of surface melting on ice. *J. Cryst. Growth* **129**, 491–505 (1993).
19. Kuroda, T. & Lacmann, R. Growth kinetics of ice from the vapour phase and its growth forms. *J. Cryst. Growth* **56**, 189–205 (1982).
20. Jellinek, H. H. . Adhesive properties of ice. *J. Colloid Sci.* **14**, 268–280 (1959).
21. Asakawa, H., Sazaki, G., Nagashima, K., Nakatsubo, S. & Furukawa, Y. Two types of quasi-liquid layers on ice crystals are formed kinetically. *Proc. Natl. Acad. Sci.* **113**, 1749–1753 (2016).
22. Van Oss, C. J., Roberts, M. J., Good, R. J. & Chaudhury, M. K. Determination of the apolar component of the surface tension of water by contact angle measurements on gels. *Colloids and Surfaces* **23**, 369–373 (1987).
23. Van Oss, C. J., Ju, L., Chaudhury, M. K. & Good, R. J. Estimation of the polar parameters of the surface tension of liquids by contact angle measurements on gels. *J. Colloid Interface Sci.* **128**, 313–319 (1989).
24. Zhang, D. *et al.* The electrochemical transfer of CVD-graphene using agarose gel as solid electrolyte and. *Chem. Commun.* **51**, 2987–2990 (2015).
25. Kiselev, A. V. Non-specific and specific interactions of molecules of different electronic structures with solid surfaces. *Discuss. FARADAY Soc.* 205–218 (1965).

26. Owens, D. K. & Wendt, R. C. Estimation of the surface free energy of polymers. *J. Appl. Polym. Sci.* **13**, 1741–1747 (1969).
27. Fowkes, F. M. Attractive forces at interfaces. *Ind. Eng. Chem.* **56**, 40–52 (1964).
28. Yoon, T. *et al.* Direct measurement of adhesion energy of monolayer graphene as-grown on copper and its application to renewable transfer process. *Nano Lett.* **12**, 1448–1452 (2012).
29. Deng, S. & Berry, V. Wrinkled, rippled and crumpled graphene: An overview of formation mechanism, electronic properties, and applications. *Mater. Today* **19**, 197–212 (2016).
30. Tang, X., Xu, S., Zhang, J. & Wang, X. Five orders of magnitude reduction in energy coupling across corrugated graphene / substrate interfaces. *ACS Appl. Mater. Interfaces* **6**, 2809–2818 (2014).
31. Tadros, M. E., Hu, P. & Adamson, A. W. Adsorption and contact angle studies I. Water on smooth carbon, linear polyethylene, and stearic acid-coated copper. *J. Colloid Interface Sci.* **72**, 515–523 (1979).
32. Kozbial, A., Trouba, C., Liu, H. & Li, L. Characterization of the intrinsic water wettability of graphite using contact angle measurements: Effect of defects on static and dynamic contact angles. *Langmuir* **33**, 959–967 (2017).
33. Ondarçuhu, T. *et al.* Wettability of partially suspended graphene. *Sci. Rep.* **6**, 24237 (2016).
34. Buckingham, a. D. Theory of long-range dispersion forces. *Discuss. Faraday Soc.* **40**, 232 (1965).
35. Leite, F. L., Bueno, C. C., Da Róz, A. L., Ziemath, E. C. & Oliveira, O. N. Theoretical models for surface forces and adhesion and their measurement using atomic force microscopy. *Int. J. Mol. Sci.* **13**, 12773–12856 (2012).
36. Hamaker, H. C. The London-Van Der Waals attraction between spherical particles. *Physica* **4**, 1058–1072 (1937).
37. Tai Yup Chang. Moderately long-range interatomic forces. *Rev. Mod. Phys.* **39**, 911–942 (1967).

CHAPTER 6

Macroscopic and microscopic wettability of graphene: substrate effect

Interactions between water and graphene can be probed on a macroscopic level through wettability by measuring water contact angle, and on microscopic level through water desorption kinetics studies using surface science methods. Contact angle studies of graphene pinpointed the critical role of sample preparation and measurement conditions for assessing the wettability of graphene. So far, studies of water desorption from graphene under the conditions of ultra-high vacuum provided superior control over the environment, but disregarded the importance of sample preparation. In this chapter the effect of the morphology of the growth substrate and of transfer process on the macroscopic and microscopic wettability of graphene is systematically examined. Remarkably, macroscopic wetting transparency of graphene does not always translate into microscopic wetting transparency, particularly in the case of atomically-defined Cu(111) substrate. Additionally, subtle differences in substrates significantly alter the interactions between graphene and the first monolayer of adsorbed water, but have negligible effect on the apparent macroscopic wettability.

Manuscript in preparation. L.A. Belyaeva, C. Tong, G.F. Schneider, L. Juurlink

6.1. Introduction

The subject of wettability of graphene has been widely studied, but nonetheless, remains under ongoing debate.^{1,2} Understanding and taking control of the wetting behavior of graphene would benefit to the wide range of graphene applications – sensors, nanoelectronics, fuel cells etc.^{3–8} However, there exist a remarkable discrepancy of the reported contact angles of graphene, varying from very hydrophilic when supported by water,⁹ mildly hydrophilic on glass¹⁰ to hydrophobic on silicon carbide and copper.^{11,12} In general, three factors determine the wetting properties of graphene: the intrinsic wettability of graphene, the effect of the underlying substrate, i.e. the wetting transparency of graphene,^{10,13,14} and the sample preparation-related environmental factors, such as morphological features and defects caused by the growth and transfer processes,¹⁵ contamination and adsorption of airborne hydrocarbons.¹⁶ And while the intrinsic contact angle of clean free-standing graphene has been already determined to be $42^\circ \pm 3^\circ$ both theoretically^{17,18} and experimentally,¹⁹ the effects of wetting transparency and imperfections linked to performing measurements under ambient conditions are difficult to disentangle. As a result of the diversity of growth and handling conditions, graphene has been independently shown to be fully transparent,¹⁰ partially transparent¹⁴ and fully opaque to wetting.^{11,20} Particularly, irregularities in graphene structure caused by the transfer appear paramount for the disruption of the wetting transparency.⁹

Another route to approach the wettability of graphene is to study water desorption using surface science methods, such as temperature programmed desorption (TPD)²¹ and thermal desorption spectroscopy (TDS).^{22,23} Contrarily to the macroscopic contact angle measurements in ambient atmosphere, TPD and TDS probe interactions between a surface and isolated water molecules under ultra high vacuum (UHV) conditions and characterize the so called “wettability on a molecular level”. The wettability on a molecular level, however, does not necessarily correlate with the apparent macroscopic wettability (e.g. in the case of silver and gold), but complements the macroscopic observations. Macroscopic wettability observed in ambient atmosphere involves significantly larger number of collisions and interactions between molecules (both of water and environment) than microscopic wettability observed in UHV.²⁴ As for studies involving contact angle measurements, several TPD and TDS studies of graphene

124

showed contrasting results on the wetting transparency (on molecular level) of graphene, particularly, graphene on Ru(0001), Cu and Si/SiO₂, were shown to be opaque in water desorption measurements,^{22,23,25} but nearly transparent in the benzene desorption measurements (with the exception of graphene on Ru(0001) which was opaque in both cases).²⁶ A theoretical study also demonstrated the prominent substrate effect on the water desorption on graphene by investigating the electronic properties of graphene upon water adsorption.²⁷ Given the extreme accuracy and cleanliness of the measurements under UHV, the reported discrepancies in microscopic wettability of graphene distinctly point at the crucial role of the sample preparation preceding the desorption experiments.

Here the effects of substrate crystallinity and of transfer process on the wettability and wetting transparency of graphene were studied both from macroscopic and microscopic perspectives. The same samples were used for contact angle measurements and TPD allowing, therefore, for a direct comparison between macroscopic wettability and water desorption in vacuum. Although graphene manifests nearly wetting transparent macroscopically regardless preceding treatment, desorption measurements showed that the morphology of the substrate and transfer-induced irregularities significantly alter interactions between graphene and the first monolayer of water molecules.

6.2. Results

Three different samples were studied comparatively by contact angle measurements and TPD: i) graphene as-grown on Cu(111), ii) graphene as-grown on polycrystalline copper and iii) graphene transferred to a polycrystalline copper substrate. The bare polycrystalline copper and Cu(111) were also tested after the graphene layer was removed by argon sputtering in UHV. The as-grown samples were prepared using chemical vapor deposition (CVD) method and the transferred sample was first grown on a different copper foil according to the same CVD protocol and then transferred to polycrystalline copper using the PMMA-assisted transfer method (see Appendix 5 for more details). Then the samples were studied using TPD at various water coverages on graphene. After each measurement, the graphene layer was removed directly in the UHV

chamber by sputtering, and water desorption from the bare copper substrates was also studied using the same procedures (see Appendix 5). As copper quickly oxidizes once exposed to air, contact angles were measured for bare copper crystals after annealing in hydrogen atmosphere (i.e. within 1-2 minutes) and 30 minutes after the annealing. No oxide layer was formed in the samples of as-grown graphene on copper, as during CVD graphene grows on copper directly in vacuum without exposure to air. However, to remove the adsorbed airborne hydrocarbons¹⁶ all graphene samples were also annealed right before contact angle measurements.

6.2.1. Graphene grown on Cu(111)

Figure 6.1a, b show that graphene grown on Cu(111) is not fully transparent to water desorption. Specifically, although graphene on Cu(111) and bare Cu(111) show the same onset desorption temperature T_{onset} close to 160K, their kinetic characteristics differ significantly. Shared leading edge and shift to higher temperatures with the increase in coverage in Figure 6.1a indicate a zero-order desorption in the case of graphene on Cu(111); and the mixed features of the zero and first order in Figure 6.1 b indicate a fractional order (between 0 and 1) desorption for bare Cu(111). The zero-order kinetics in the case of graphene on Cu(111) is ascribed to two-dimensional equilibrium between individual water molecules and islands of condensed water^{21,28} and, thus, indicates that water tends to form multilayer clusters rather than continuous monolayer on graphene. Contrastingly, the fractional kinetic order of the bare Cu(111) shows that its surface is more favorable (compared to graphene on Cu(111)) for the adsorption of water molecules.

Remarkably, the adsorbed water forms different crystalline phases on graphene on Cu(111) and bare Cu(111). The desorption curves of graphene on Cu(111) display a “bump” on their descending edge (Figure 1a), indicative of the formation of the metastable amorphous water ice,^{21,29–31} while the shape of the desorption curves for bare Cu(111) suggests formation of thermodynamically stable crystalline water ice.

Raman spectra in Figure 6.1c confirmed that graphene is monolayer with a sharp 2D mode and high quality with very small defect-related D mode. The absence of graphene bands in Figure 6.1d indicates that graphene was completely removed from copper after argon sputtering .

As seen from Figure 6.1e, f, the contact angle measurements did not show a significant difference between graphene on Cu(111) and bare Cu(111): $90^\circ \pm 1^\circ$ for graphene grown on Cu(111)(Figure 6.1e) and $76^\circ \pm 3^\circ$ for bare nonoxidized Cu(111)(Figure 6.1f). However, the slightly more hydrophobic behavior of graphene on Cu(111) coincides with its lower affinity to water on a molecular level observed in TPD.

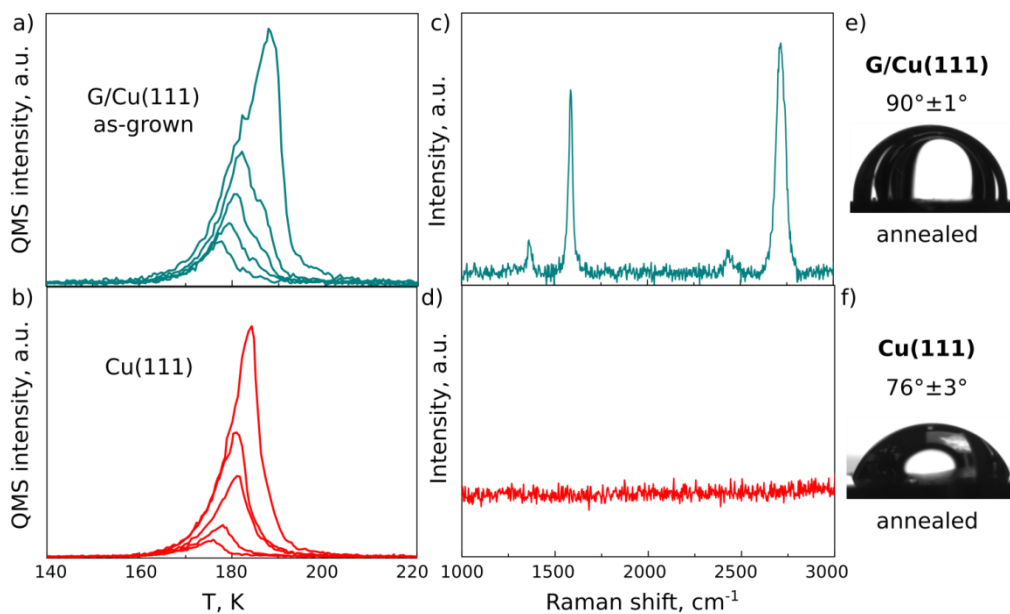


Figure 6.1. Microscopic and macroscopic wettability of graphene grown on Cu(111). a) TPD curves of graphene grown on Cu(111) at submonolayer coverages. b) Temperature programmed desorption (TPD) curves of bare Cu(111) at submonolayer coverages. c) Typical Raman spectrum of graphene grown on Cu(111). d) Typical Raman spectrum of bare Cu(111) after graphene removal by argon sputtering. e) Water contact angle of graphene grown on Cu(111) measured immediately after annealing. f) Water contact angle of Cu(111) measured immediately after annealing.

6.2.2. Graphene as-grown on polycrystalline Cu

Unlike graphene on Cu(111), graphene grown on polycrystalline copper is transparent to water desorption (Figure 6.2). The water desorption curves from graphene as-grown on polycrystalline copper and bare copper (Figure 6.2a and b respectively) display the same onset temperature T_{onset} , at 160K (also equal to that of graphene on Cu (111) and bare Cu(111)). The desorption curves show similar shapes with overlapping leading edges. This behavior is representative of zero-order desorption kinetics.^{21,28} Interestingly, the shapes of the TPD curves (no “bump” on the leading edges) suggest that water forms a crystalline state on graphene on polycrystalline Cu and bare polycrystalline Cu, as opposed to amorphous in the case of graphene on Cu(111).

Contact angle measurements, on the other hand, showed that bare and graphene-coated polycrystalline copper substrates have similar contact angles ($74^{\circ}\pm 1^{\circ}$ and $85^{\circ}\pm 1^{\circ}$ respectively, Figure 6.2e and f), suggesting that graphene is nearly transparent macrosopically when grown on polycrystalline copper. Interestingly, the equality of the $T_{\text{onset}}=160\text{K}$ for the polycrystalline Cu and Cu(111) is consistent with the equality of their contact angles (i.e., $74^{\circ}\pm 1^{\circ}$ for annealed polycrystalline copper and $76^{\circ}\pm 3^{\circ}$ for annealed Cu(111), Figure 6.2f and Figure 6.1f respectively).

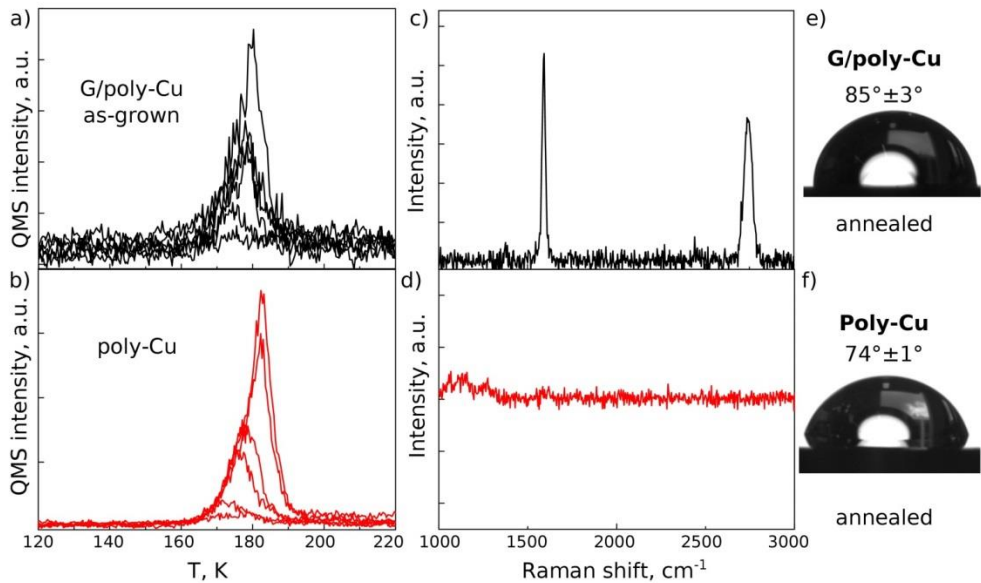


Figure 6.2. Microscopic and macroscopic wettability of graphene grown on polycrystalline Cu. a) TPD curves of graphene grown on polycrystalline Cu at submonolayer coverages. b) TPD curves of bare polycrystalline Cu at submonolayer coverages. c) Typical Raman spectrum of graphene grown on polycrystalline Cu. d) Typical Raman spectrum of bare polycrystalline Cu after graphene removal. e) Water contact angle of graphene grown on polycrystalline Cu measured right after annealing. f) Water contact angle of polycrystalline Cu measured right after annealing.

Clearly, relationships between microscopic and macroscopic wettability of graphene are not straightforward and are difficult to decipher. On one hand, the TPD was more sensitive to the morphology of the growth substrate (Cu(111) versus polycrystalline copper) and demonstrated that the morphology of the copper affects the interactions between the first layer of adsorbed water molecules and graphene, while the contact angle measurements showed no difference for graphene on Cu(111) and on polycrystalline copper (slight increase of the contact angle by $\sim 10^\circ$ as compared to the bare substrates). On the other hand, in the case of graphene on polycrystalline copper, the contact angle measurements indicated a difference in the wetting of graphene on copper and of bare copper (Figure 6.2e and f), while the desorption measurements did not detect any difference in kinetics between the two samples.

6.2.3. Graphene transferred onto polycrystalline copper

Graphene transferred onto the same polycrystalline copper, on one hand, similarly manifests wetting transparent at a molecular level, showing no difference in desorption behavior between graphene on copper and bare copper (Figure 6.3a, b). On the other hand, the TPD curves in this case exhibit different kinetic features compared to the as-grown sample: the T_{onset} of 140K and a fractional kinetic order of desorption between zero and one (shift to a higher temperature range with increasing coverage but an ascending leading edge, Figure 6.3a, b). The surprising difference in T_{onset} and kinetics even between two, in principle, identical bare copper substrates in Figure 6.2 and Figure 6.3 can be explained by the formation of copper oxide on the top copper layer in the case when graphene was transferred.³² During the transfer process the copper crystal is inevitably exposed to air and immersed in water, which are factors that are known to cause the oxidation of copper.³³ In the case of the as-grown graphene, the copper crystal is pre-annealed in hydrogen for three hours and then immediately followed by the graphene growth in vacuum, without any exposure to the ambient oxygen. For transferred samples, therefore, the contact angle of oxidized, i.e. exposed to air, copper crystal must be measured for appropriate referencing with TPD results. Similarly to the as-grown sample, the contact angle of the graphene transferred onto Cu crystal ($91^\circ \pm 5^\circ$, Figure 6.3e) is close to the $83^\circ \pm 2^\circ$ of the oxidized copper crystal after exposure to air (Figure 6.3f). Interestingly, these values are higher than the $74^\circ \pm 1^\circ$ measured for freshly-annealed copper (Figure 6.2f), which together with the lower T_{onset} of the desorption peaks (Figure 6.3a, b) indicate a more hydrophobic behavior for graphene transferred onto (oxidized) copper and bare (oxidized) copper compared to the as-grown sample and non-oxidized copper.

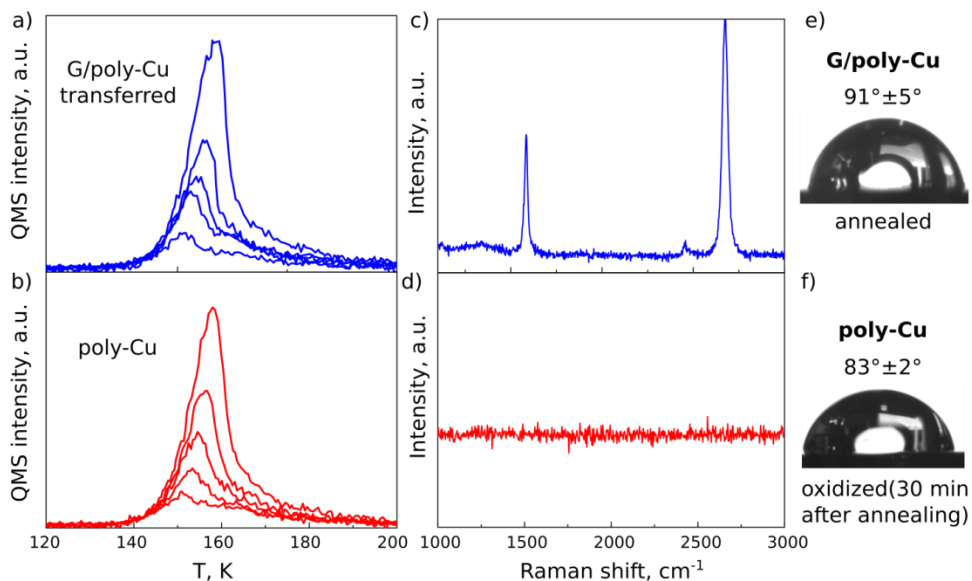


Figure 6.3. Microscopic and macroscopic wettability of graphene transferred on polycrystalline Cu. a) TPD curves of graphene transferred on polycrystalline Cu at submonolayer coverages. b) TPD curves of bare polycrystalline Cu after graphene removal at submonolayer coverages. c) Typical Raman spectrum of graphene transferred on polycrystalline Cu. d) Typical Raman spectrum of bare polycrystalline Cu after graphene removal. e) Water contact angle of graphene transferred on polycrystalline Cu measured immediately after annealing. f) Water contact angle of oxidized polycrystalline Cu measured 30 minutes after annealing.

6.3. Conclusions

In summary, the effects of substrate crystallinity and of transfer process on the interactions between graphene and water were investigated from both a microscopic and a macroscopic perspectives. Contact angle measurements showed that the macroscopic wettability of graphene is independent of the substrate crystallinity and transfer, and addition of graphene layer on top of copper only slightly increases the contact angle by $\sim 10^\circ$, indicating that graphene is nearly wetting transparent in all three samples. Contrastingly, desorption measurements demonstrated that the morphology of the substrate and transfer-

related imperfections appreciably affect the adsorption of the water monolayer on the graphene surface. In the case of smooth and atomically-defined Cu(111), the deposition of a graphene layer not only resulted in the change of water desorption kinetics, but also in the formation of metastable amorphous water ice, as opposed to crystalline ice in the case of bare Cu(111). For rougher polycrystalline copper, on the other hand, the deposition of the graphene layer (both by direct growth and transfer) did not alter the kinetic characteristics of the copper, manifesting, therefore, wetting transparency on a molecular level. Interestingly, annealed and oxidized polycrystalline copper crystals have different desorption characteristics (T_{onset} and desorption order, see Figure 6.2b and Figure 6.3b) which are completely retained after the deposition of the graphene layer on top. The difference in wettability of as-grown and transferred graphene, observed in this work and elsewhere, therefore, seems to stem from the fact that copper is inevitably oxidized in the case of transferred graphene.

As a conclusion, the TPD and contact angle data describe different phenomena and are not perfectly intercorrelated, but rather provide complementary insights. Suchwise, due to the extreme smoothness and homogeneity of the surface of monocrystalline Cu(111), its microscopic wetting properties are readily affected by the addition of a graphene layer, while in the case of polycrystalline copper the surface properties are dominated by its significant roughness and the addition of graphene – a monoatomic and fully conforming layer – has a negligible effect. The TPD proves very sensitive to the subtle changes in the graphene and the underlying substrate (such as crystallinity) and is informative in the scenarios when interactions between graphene and individual molecules of adsorbate are of interest. Macroscopic wettability measured by contact angle measurements, on the other hand, cannot predict the interactions with individual molecules, but, instead, characterizes the interactions between graphene and macroscopic phases of adsorbate under ambient pressures. Following up the recent studies on the effect of sample preparation on the macroscopic wettability of graphene, this chapter goes further and provides more detailed insights on how different aspects of sample preparation affect the interactions of graphene with individual molecules and with bulk phases.

6.4 References

1. Shih, C.-J., Strano, M. S. & Blankschtein, D. Wetting translucency of graphene. *Nat. Mater.* **12**, 866–869 (2013).
2. Parobek, D. & Liu, H. Wettability of graphene. *2D Mater.* **2**, 32001 (2015).
3. K. S. Novoselov, S. V. Morozov, D. Jiang, Y. Zhang, S. V. Dubonos, I. V. Grigorieva, A. A. Firsov, A. K. G. Electric field effect in atomically thin carbon films. *Science* **306**, 666–669 (2004).
4. Xu, Y. *et al.* In-plane and tunneling pressure sensors based on graphene/hexagonal boron nitride heterostructures. *Appl. Phys. Lett.* **99**, 1–4 (2011).
5. Schedin, F. *et al.* Detection of individual gas molecules adsorbed on graphene. *Nat. Mater.* **6**, 652–655 (2007).
6. Heerema, S. J. & Dekker, C. Graphene nanodevices for DNA sequencing. *Nat. Nanotechnol.* **11**, 127–136 (2016).
7. Wang, Z. & Liu, C. J. Preparation and application of iron oxide/graphene based composites for electrochemical energy storage and energy conversion devices: Current status and perspective. *Nano Energy* **11**, 277–293 (2015).
8. Yoon, J. C., Yoon, C. S., Lee, J. S. & Jang, J. H. Lotus leaf-inspired CVD grown graphene for a water repellent flexible transparent electrode. *Chem. Commun.* **49**, 10626–10628 (2013).
9. Belyaeva, L. A., van Deursen, P. M. G., Barbetsea, K. I. & Schneider, G. F. Hydrophilicity of graphene in water through transparency to polar and dispersive interactions. *Adv. Mater.* **30**, 1–7 (2018).
10. Rafiee, J. *et al.* Wetting transparency of graphene. *Nat. Mater.* **11**, 217–222 (2012).
11. Taherian, F., Marcon, V., Van Der Vegt, N. F. A. & Leroy, F. What is the contact angle of water on graphene? *Langmuir* **29**, 1457–1465 (2013).
12. Wang, S., Zhang, Y., Abidi, N. & Cabrales, L. Wettability and surface free

- energy of graphene films. *Langmuir* **25**, 11078–11081 (2009).
13. Driskill, J., Vanzo, D., Bratko, D. & Luzar, A. Wetting transparency of graphene in water. *J. Chem. Phys.* **141**, 18C517 (2014).
 14. Shih, C. J. *et al.* Breakdown in the wetting transparency of graphene. *Phys. Rev. Lett.* **109**, 176101 (2012).
 15. Ghaderi, N. & Peressi, M. First-principle study of hydroxyl functional groups on pristine, defected graphene, and graphene epoxide. *J. Phys. Chem. C* **114**, 21625–21630 (2010).
 16. Li, Z. *et al.* Effect of airborne contaminants on the wettability of supported graphene and graphite. *Nat. Mater.* **12**, 925–931 (2013).
 17. Yiapanis, G., Makarucha, A. J., Baldauf, J. S. & Downton, M. T. Simulations of graphitic nanoparticles at air-water interfaces. *Nanoscale* **8**, 19620–19628 (2016).
 18. Andrews, J. E., Sinha, S., Chung, P. W. & Das, S. Wetting dynamics of a water nanodrop on graphene. *Phys. Chem. Chem. Phys.* **18**, 23482–23493 (2016).
 19. Prydatko, A. V, Belyaeva, L. A., Jiang, L., Lima, L. M. C. & Schneider, G. F. Contact angle measurement of free-standing square-millimeter single-layer graphene. *Nat. Commun.* **9**, 4185 (2018).
 20. Raj, R., Maroo, S. C. & Wang, E. N. Wettability of graphene. *Nano Lett.* **13**, 1509–1515 (2013).
 21. Smith, R. S., Matthiesen, J. & Kay, B. D. Desorption kinetics of methanol, ethanol, and water from graphene. *J. Phys. Chem. A* **118**, 8242–8250 (2014).
 22. Chakradhar, A. & Burghaus, U. Adsorption of water on graphene/Ru(0001)—an experimental ultra-high vacuum study. *Chem. Commun.* **50**, 7698–7701 (2014).
 23. Chakradhar, A., Sivapragasam, N., Nayakasinghe, M. T. & Burghaus, U. Support effects in the adsorption of water on CVD graphene: an ultra-high vacuum adsorption study. *Chem. Commun.* **51**, 11463–11466 (2015).

24. Ceyer, S. T. New mechanisms for chemistry at surfaces. *Science* **249**, 133–139 (1990).
25. Chakradhar, A., Trettel, K. & Burghaus, U. Benzene adsorption on Ru(0001) and graphene/Ru(0001)—How to synthesize epitaxial graphene without STM or LEED? *Chem. Phys. Lett.* **590**, 146–152 (2013).
26. Chakradhar, A., Sivapragasam, N., Nayakasinghe, M. T. & Burghaus, U. Adsorption kinetics of benzene on graphene: an ultrahigh vacuum study. *J. Vac. Sci. Technol. A Vacuum, Surfaces, Film.* **34**, 21402 (2016).
27. Wehling, T. O., Lichtenstein, A. I. & Katsnelson, M. I. First-principles studies of water adsorption on graphene: the role of the substrate. *Appl. Phys. Lett.* **93**, 202110 (2008).
28. Daschbach, J. L., Peden, B. M., Smith, R. S. & Kay, B. D. Adsorption, desorption, and clustering of H₂O on Pt(111). *J. Chem. Phys.* **120**, 1516–1523 (2004).
29. Stevenson, K. P., Kimmel, G. A., Dohnálek, Z., Smith, R. S. & Kay, B. D. Controlling the morphology of amorphous solid water. *Science* **283**, 1505–1507 (1999).
30. Smith, R. S., Petrik, N. G., Kimmel, G. A. & Kay, B. D. Thermal and nonthermal physiochemical processes in nanoscale films of amorphous solid water. *Acc. Chem. Res.* **45**, 33–42 (2012).
31. Smith, R. S., Matthiesen, J., Knox, J. & Kay, B. D. Crystallization kinetics and excess free energy of H₂O and D₂O nanoscale films of amorphous solid water. *J. Phys. Chem. A* **115**, 5908–5917 (2011).
32. Gottardi, S. *et al.* Comparing graphene growth on Cu(111) versus oxidized Cu(111). *Nano Lett.* **15**, 917–922 (2015).
33. Luo, D. *et al.* Role of graphene in water-assisted oxidation of copper in relation to dry transfer of graphene. *Chem. Mater.* **29**, 4546–4556 (2017).

CHAPTER 7

Summary, conclusions and outlook

Graphene is known as a “wonder material” which was believed – 15 years ago – to revolutionize electronic technologies, a physicist’ treasure full of exciting fundamental phenomena, and at the same time, a material that has not yet met the industrial expectations. When it was first isolated in 2004, the research world was astonished by the ultimate simplicity with which it then became possible to produce a material in many aspects excelling the existing ones. Isolating this single material led to a number of fundamental discoveries and motivated several new research fields. In terms of application, the rich functionality of graphene inspired a multitude of new concepts and designs implemented in laboratory settings. However, despite the potential capability to revolutionize a number of current technologies, the much-anticipated transition from laboratory prototypes of graphene-based devices to large scale industrialization faced serious challenges: production, manipulation and design of devices based on large-scale production methods. And while mass-scale production of high-quality graphene now can be done with the CVD growth, methods to transfer and handle large sheets of CVD graphene are still under on-going development, aiming at cleaner and nondisruptive strategies. Finally, during the fabrication and operation of the device, graphene is routinely transferred from surface to surface and is affected by the changing environment – water, supporting substrate, air, electrodes, adsorbates, analytes etc. The overall device performance, therefore, is difficult to predict without assessing the impacts of every step of manipulation (and thus, of different interfaces and environment) on graphene. Graphene-liquid interfaces are of particular interest: they are ubiquitously used in graphene handling and device operation, but, nonetheless, are poorly understood, especially in comparison to graphene-solid interfaces.

This thesis expands the current knowledge on the interactions between graphene and fluidic interfaces, particularly on the effects that liquids have on the structural, electronic and mechanical properties of graphene. Secondly, it offers new liquid-based experimental solutions and methods for improving handling and characterizing graphene. Liquids and liquid interfaces, therefore, transform throughout this thesis from the subjects of studies into the tools for studies and *vice versa*.

7.1. Summary and conclusions

Chapter 2 shows how a biphasic system of two immiscible liquids can be used for graphene transfer. This method avoids polymer contamination typical for most common transfer methods, but also protects the graphene structure from cracking and folding, in contrast to other polymer-free strategies. It was found that liquids underneath and on top of graphene can serve both as a mechanical support and a protecting layer for graphene, similarly to a solid substrate and a polymer film. In fact, liquids can be a more flexible tool to transfer and handle graphene: their properties can be *in situ* modified by mixing with other liquids, freezing, evaporating etc. For example, a cyclohexane phase on top of graphene can be frozen to form a soft plastic crystal polymorph (similarly to a protective polymer film), which after the transfer can be removed by sublimation directly from solid to gaseous phase. Additionally, in Chapter 2 a liquid interface (namely, cyclohexane and water with graphene in between) was harnessed to study electron transport across the graphene sheet. Noteworthy, charge carrier mobilities exceeding the ones measured for the solid substrates were measured.

Chapter 3 concludes that the major reasons behind the measured improved electrical performance of graphene floating at liquid interfaces are lower strain and doping levels, as opposed to supported graphene. Interestingly, strain is well known as a major factor responsible for degraded electrical performance of graphene and graphene-based devices, but is almost impossible to prevent, as solid supports do not match the inherent morphology of graphene and disturb the homogeneity of the graphene surface. In contrast, liquid interfaces, irrespective of their chemical nature, are naturally more homogeneous and adapt to the inherent morphology of graphene.

Chapters 4 and 5 demonstrate how the use of liquids can provide insights where solid supports are impractical. The concept of using liquids, and water specifically, simultaneously as subjects of research and parts of the experimental setup proved particularly fruitful for the wettability studies on graphene. Unlike bulk solids, conventional sessile drop configuration is unstable on free-standing graphene: graphene breaks, due to gravity and surface tension of water. However, graphene is perfectly stable in the inverted configuration where water is used underneath graphene as a support; injection of an air bubble underneath

floating graphene results in an inverted but equivalent (to sessile drop setup) water-graphene-air interface allowing for a stable contact angle measurement (Chapter 4). In Chapter 5 water, this time in the form of ice and hydrogels, was again used as an underlying support for graphene, to probe for the first time the much debated wetting transparency of graphene in water. Altogether, the approaches described in Chapters 4 and 5 resulted in a number of principal insights: 1) graphene is intrinsically hydrophilic (water contact angle of $42^\circ \pm 3^\circ$) 2) graphene is wetting transparent in water, *i.e.* transmits water-water interactions, and 3) the quality of the graphene-substrate interface is a determinative factor for the occurrence of the wetting transparency of graphene.

Chapter 6 is the only part of this thesis that does not use or study interactions between graphene and liquids *per se*. It, however, adds a new important insight to the discourse: wetting properties of graphene at the macroscopic level do not straightforwardly translate into interactions between graphene and individual water molecules. Concepts of hydrophilicity and hydrophobicity are often used to interpret other phenomena, such as adsorption, desorption and chemical affinity to certain types of compounds. And while finding correlations between them provides a wider perspective, generalization can lead to incorrect conclusions. In particular, Chapter 6 demonstrates that the crystallinity of the growth substrate alters the desorption kinetics of water molecules from graphene, but has no effect on its macroscopic wettability.

7.2. Outlook

Graphene and other 2D materials promise unique opportunities for research and technology, but in return demand special approaches and development of alternative tools and characterization methods, different from those conventionally used for 3D materials. The approaches proposed in this thesis have already yielded interesting insights, but more importantly, they provide the ground for further developments. As a most straightforward implication, the knowledge and the methodology developed in this thesis can already be applied to other 2D van der Waals materials, such as hexagonal boron nitride, dichalcogenides and fluorographene.

Furthermore, the characterization and electrical measurements of graphene floating at liquid interfaces, presented in Chapters 2 and 3, provide settings for studying a variety of interfacial phenomena *in situ* – by varying the solvent composition, adding solutes and surfactants, applying gate voltage and magnetic field, and other external stimuli. Chemically functionalized graphene can be used for tuning the interactions with the liquid medium and solutes. Furthermore, the Surface Enhanced Raman Spectroscopy (SERS), instead of conventional Raman spectroscopy used in Chapter 3, can be applied to achieve higher resolution and detect more subtle effects occurring at the interface.

The relaxation of strain and enhanced charge carrier mobilities – arguably, the most significant findings of this thesis – make fluidic interfaces with free-floating graphene particularly appealing for *in situ* sensing in liquids: liquids can allow for increased sensitivity (due to reduced strain and enhanced charge carrier mobilities) and serve as an experimental media at the same time. The technical implementation, however, faces a major challenge: electrical probing of a one-atom-thin graphene layer free-floating on a liquid is extremely difficult (at least, in the way described in Chapter 2) even in laboratory conditions. In order to obtain an electrical response few problems must be first addressed: establishing non-destructive yet reliable graphene-electrodes contacts, preserving structural integrity of graphene and stabilizing graphene on the surface of water. The lack of stability, as the flip side of structural flexibility, is the major drawback of using fluidic interfaces in graphene research in general. As an alternative to direct electrical measurements, remote electrical probing of graphene in liquids can be used to circumvent the stability issues, especially given the rapid advancement that the remote technologies are currently undergoing.

Although liquids cannot fully replace solid substrates in graphene research, this work showed that their advantages as substrates certainly can be used more widely and facilitate several research fields. In a world seeking sustainable energy solutions, liquids with their ubiquitous presence in nature, commercial availability and inexpensiveness (especially compared to the solid substrates used in hi-tech industries) will inevitably have to become an essential part of future technologies. Research presented in this thesis contributed to this emerging trend by developing concepts and tools to harness liquids in application to

graphene, and by proving that simple and sustainable solutions can also yield superior performance.

APPENDIX 1

Supporting Information to Chapter 2

1.1. Methods

1.1.1. Growth and transferring of graphene

Copper foil with the thickness of 25 μm was annealed at 1035°C and the monolayer graphene films were grown using chemical vapor deposition.¹ After the chemical vapor deposition (CVD) synthesis, the graphene grown on the backside of the copper foil was removed by using oxygen plasma. After etching the graphene at the backside of the copper foil, the piece was placed at the interface of a biphasic mixture of cyclohexane and water supplemented with ammonium persulfate (*i.e.* the copper etchant). For transferring the graphene onto substrates with the interfacial caging method the approaches described in the “Results” section of Chapter 2 were followed. All samples were rinsed with water and ethanol after the transfer. For the poly(methyl methacrylate) (PMMA)-assisted method the protocol from Reference 2 was reproduced. For the contact stamping method a wafer was directly placed on graphene floating on the etchant, transferred and rinsed with water; alternatively, the etchant is replaced by pure water prior stamping. For the hexane-assisted transfer method reproduced the protocol from Reference 3 was reproduced: placed a wafer beneath graphene (in the etchant) and fishing from below the graphene with hexane as the top phase. In all four transfer methods 0.5 M solution of $(\text{NH}_4)_2\text{S}_2\text{O}_8$ was used as copper etchant.

1.1.2. Characterization

Raman spectroscopy

Micro-Raman spectroscopy was performed with a commercial inVia model from Renishaw spectrometer set-up with a dual-axis XY piezo stage. A laser with 532 nm excitation wavelength was used. The grating has 600 lines/mm. Raman spectra are recorded in air with a 100x objective. The laser power was limited to below 2 mW to prevent any laser induced heating of the samples.

Atomic force microscopy (AFM)

All AFM experiments with graphene on silicon wafers were carried out on Multimode Bruker (ex-DI) Nanoscope V. The experiments were performed using a silicon 254 probe (AC160TS, Asylum Research) with 300 kHz nominal resonance

frequency. The images were scanned in an intermittent contact mode at room temperature with 512×512 pixels. All the samples have been annealed at 400°C prior to the imaging.

Scanning electron microscopy (SEM)

SEM of graphene transferred to TEM quantifoil grids was performed with a FEI NANOSEM 200 at 10 kV. For the measurements graphene samples were transferred to quantifoil grids using the interfacial caging method.

1.1.3. Electrical measurements

To evaluate the quality of the transferred graphene in a large area, in this study graphene transistors with a channel length of several millimeters were fabricated. As the contact resistance between our graphene and metal electrodes (both are of large area) is negligible, a two-point source-drain measurements were applied and all the results were normalized by using the length/width ratio of the graphene transistors to obtain the field-effect mobility values. The transistor characteristics of the electrolyte-gated graphene field-effect transistor devices with different geometry were tested using a home-made setup. For that, a SR830 DSP lock-in amplifier with narrow filters was used to recover weak signal from a noisy background. The electrolyte gate voltage V_{ref} (up to ± 0.4 V) was applied to a Ag/AgCl reference electrode immersed in the electrolyte. For the electrical probing of graphene samples floating at the biphasic interface, the etchant solution was replaced with 0.1 M solution of KCl. During the replacement of the etchant solution, the entire mixture was cooled down to freeze the cyclohexane phase in order to avoid the effect of vibrations on the integrity of the graphene sheet.

1.2. References

1. Pierson, H. O. *Handbook of chemical vapor deposition (CVD)*. (Noyes Publications / William Andrew Publishing, LLC, 1999).
2. Suk, J. W. *et al.* Transfer of CVD-grown monolayer graphene onto arbitrary substrates. *ACS Nano* **5**, 6916–6924 (2011).
3. Zhang, G. *et al.* Versatile polymer-free graphene transfer method and applications. *ACS Appl. Mater. Interfaces* **8**, 8008–8016 (2016).

APPENDIX 2

Supporting Information to Chapter 3

2.1. Methods

2.1.1. Sample preparation

Graphene on copper. All graphene samples were grown on a copper foil by chemical vapor deposition (CVD) method, according to the protocol described in ref¹.

Graphene on Si/SiO₂ wafers and free-standing graphene. CVD graphene grown on copper was transferred to Si/SiO₂ wafers and quantifoil grids using the interfacial caging method.²

Graphene at water/air and deuterated water/air interfaces. CVD graphene grown on copper was first placed in a 0.1 M solution of ammonium persulfate (APS) in water for copper etching. After copper removal the solution underneath graphene was replaced with ultrapure water. Slightly wider variations of G and 2D peaks positions were found for graphene floating on an APS solution than for graphene on ultrapure water (see Figure A2.8 of this Appendix), attributing to doping effect, and, therefore, always thoroughly replaced APS with ultrapure water. Although, CVD graphene can stably float on the surface of water, for Raman measurements, it is also advisable to immobilize graphene from moving on the surface. This can be achieved in different ways: by placing a physical limitation, such as a plastic frame around graphene or by using very small volumes of water. The immobilization of graphene does not affect Raman results.

Graphene at a water/cyclohexane and water/1-octanol interfaces. Graphene on copper was first placed on a surface of a 0.1M solution of ammonium persulfate in water. Then cyclohexane (or 1-octanol) was added on top to form a biphasic system with graphene floating at the interface. During etching of the copper, the samples were covered with lids to prevent evaporation of the top organic phase; more cyclohexane (or 1-octanol) was added during experiments to prevent full evaporation of the top phase. After copper removal the bottom phase underneath graphene was replaced with ultrapure water. To minimize graphene movability on the surface of liquids, the size of graphene sample was fitted to the size of the Petri dish.

Hydrogenated graphene-on-copper. Graphene on copper was hydrogenated using a H₂ plasma in a computer controlled Diener plasma generator (1mbar, 10W) for 10 and 60 seconds.³

Hydrogenated graphene-on-water. The samples of hydrogenated graphene on copper were placed in a 0.1 M solution of APS for copper etching. After copper was etched away, the solution underneath hydrogenated graphene was replaced with ultrapure water.

2.1.2. Raman spectroscopy

Raman measurements were carried out with confocal spectrometer WITEC at a power below 2mW to avoid excessive thermal damage of graphene, and at excitation wavelengths of 457 nm and 532 nm. 100× objective was used for graphene on copper, graphene on Si/SiO₂ and free-standing graphene; a 70× immersion objective was used for graphene on liquid supports. Graphene/Cu samples were typically cut into 5 mm×10 mm or 10 mm×10 mm pieces, which were then studied by Raman spectroscopy directly on copper. Then graphene was transferred from copper to a SiO₂/Si substrate or a transmission electron microscopy (TEM) grid (for free-standing configuration) using the interfacial caging method,² or to liquid interfaces using the method described above. A comparative analysis showed no statistical difference between the samples of 5 mm×10 mm and 10 mm×10 mm (Figure A2.9 of this Appendix). For each substrate or liquid support 3-10 samples were tested, and for each sample 10-20 Raman spectra from different areas of graphene were recorded. There was no significant sample-to-sample variation for all substrates except free-standing graphene (see Figure A2.3 of this Appendix), which is in agreement with other reported studies.^{4,5} Noteworthy, because Raman measurements of graphene at liquid interfaces, especially in between two liquids, are technically more challenging, the spectra of such samples are typically more noisy which may have resulted in a less accurate determination and, consequently, the apparent broadening of the 2D width.

Figure A2.1a and b show the intensities of the G and 2D bands of graphene upon scanning across the water/graphene/1-octanol interface, with the position of

highest intensities (blue circles in Figure A2.1a and blue spectrum in Figure A2.1b) corresponding to the separation between the top and the bottom phase. Scanning the same interface without graphene (i.e. the same vertical coordinate and different horizontal positions) and profiling intensities of the solvents, however, do not yield any information about the position of the interface (i.e. there is no difference between the solvents peaks in the bulk phases and near the interface, see Figure A2.2).

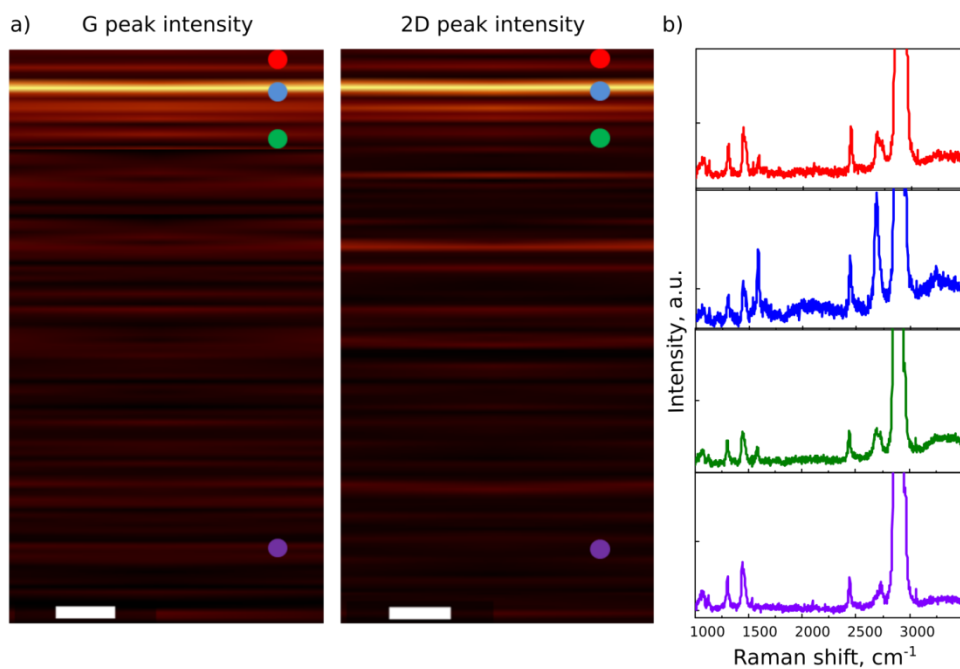


Figure A2.1. In-depth profile Raman scan of graphene at water/1-octanol interface with a 532 nm excitation wavelength. a) In-depth profiles of G and 2D peaks intensities. Coloured circles represent different positions of the measurement area with the respect to the interface between water and 1-octanol (i.e. to the line of maximum intensities of G and 2D peaks): above the interface in the 1-octanol phase (red), at the interface (blue), below but in the vicinity of the interface in the water phase (green), below the interface deeply in the water phase (purple). The scale bars represent 2 μm b) Corresponding Raman spectra recorded above the interface in the 1-octanol phase (red), at the interface (blue), below but in the vicinity of the interface in the water phase (green), below the interface deeply in the water phase (purple).

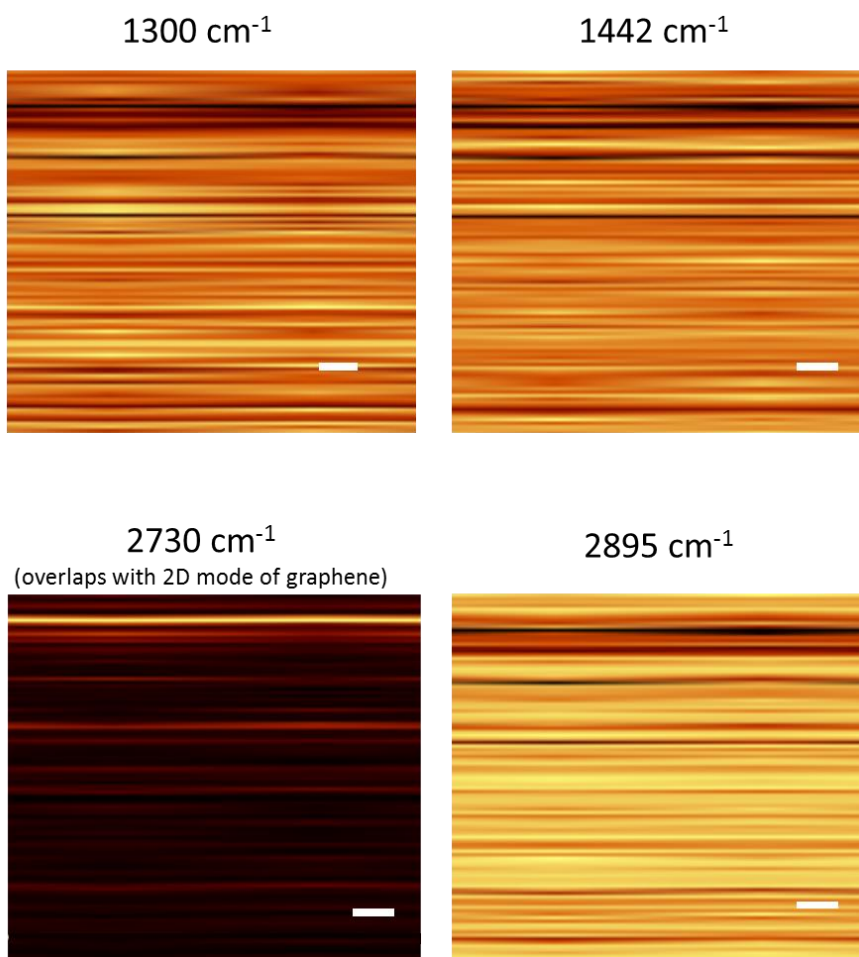


Figure A2.2. An in-depth Raman scan of water/1-octanol interface at 532 nm excitation wavelength. In-depth profiles of the intensities of 1-octanol bands at 1300cm^{-1} , 1442cm^{-1} , 2730cm^{-1} and 2895cm^{-1} . The scale bars represent $2\ \mu\text{m}$

Table A2.1. Raman bands of biphasically caged graphene, pure water, 1-octanol and cyclohexane at 457 nm and 532 nm excitation wavelengths.

	ω , cm^{-1} (457 nm)	ω , cm^{-1} (532 nm)
graphene (in biphasic caging)	~1585	~1585
	~2730	~2696
water	1640	1640
	2800-3700	2800-3700
1-octanol	1300	1300
	1442	1442
	2730	2730
	2895	2895
cyclohexane	1264	1264
	1442	1442
	2662	2662
	2851	2851
	2922	2922
	2936	2936

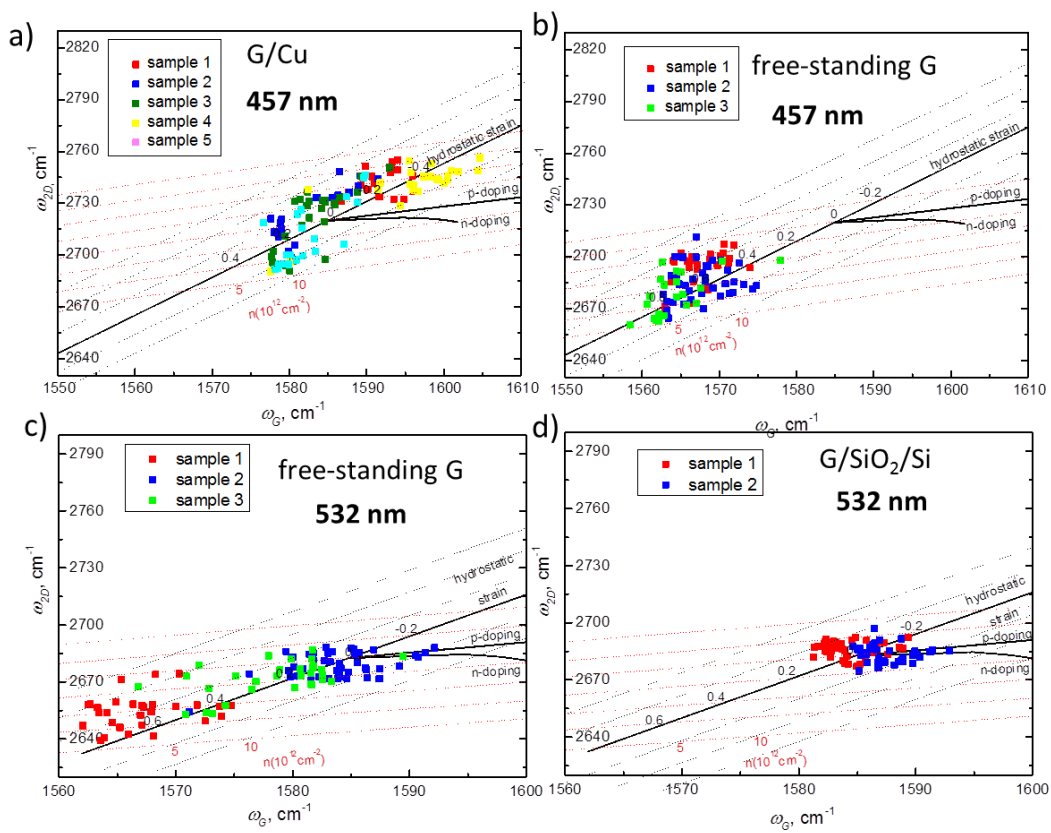


Figure A2.3. Sample to sample variation of the correlation maps of G and 2D peak positions of graphene on different substrates. a) Correlation map of graphene on copper, excitation wavelength 457 nm. b) Correlation map of free-standing graphene, excitation wavelength 457 nm. c) Correlation map of free-standing graphene, excitation wavelength 532 nm. d) correlation map of graphene on Si/SiO₂, excitation wavelength 532 nm.

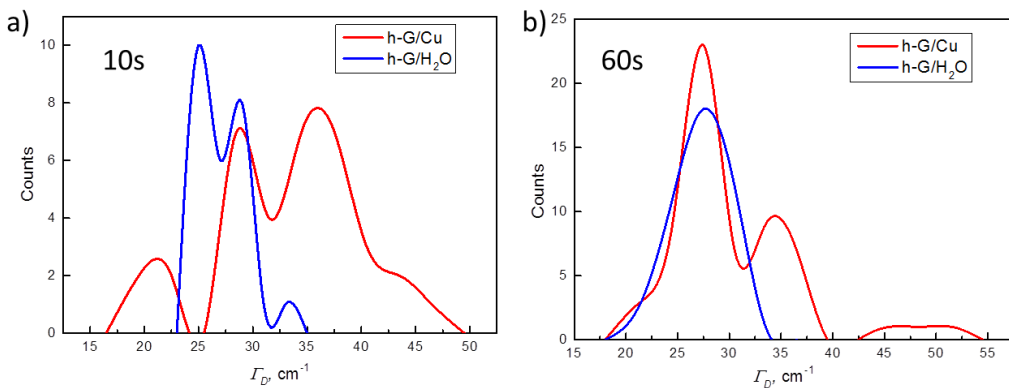


Figure A2.4. Statistical distributions of D peak widths (Γ_D) of hG on copper and water. a) Hydrogenation time 10 s. b) Hydrogenation time 60 s.

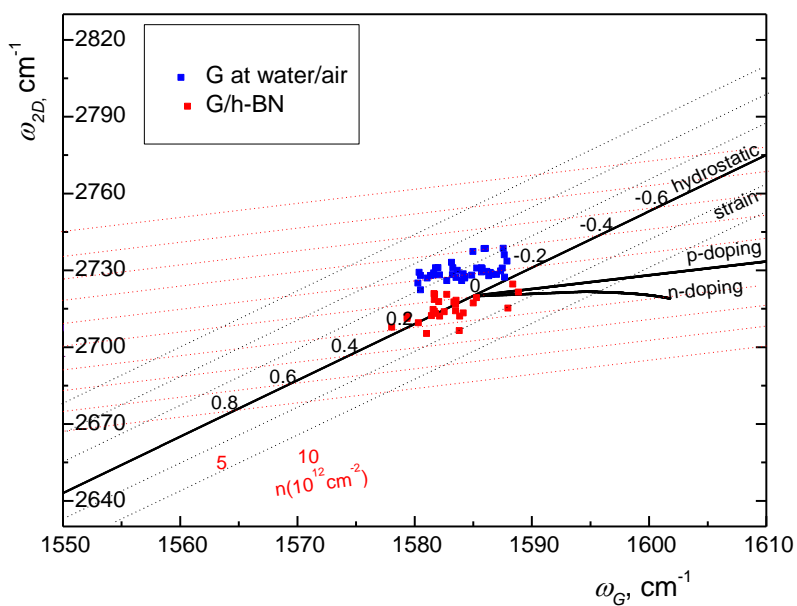


Figure A2.5. Correlation maps of graphene on water and graphene transferred to h-BN/copper, excitation wavelength 457 nm.

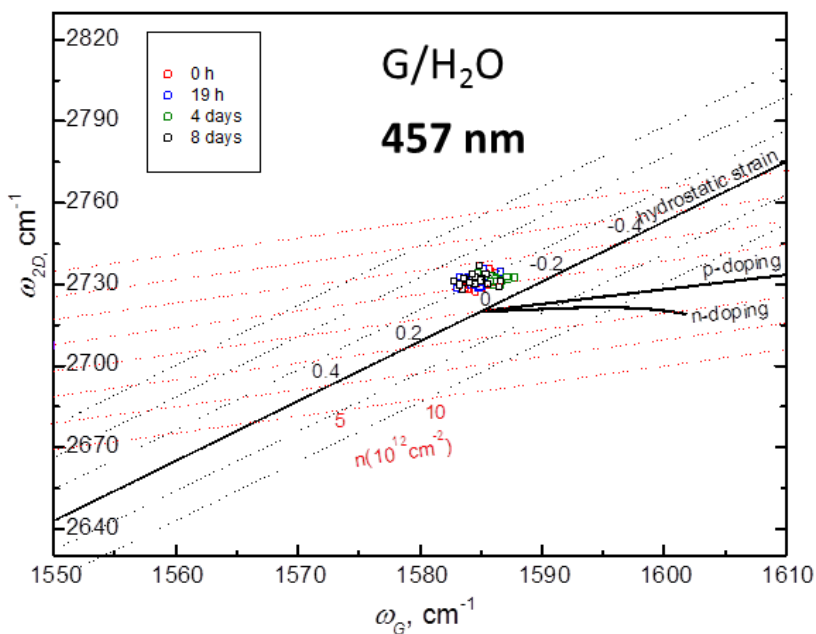


Figure A2.6. Durability of strain relaxation effect of water on graphene. Correlation map of G and 2D Raman frequencies (w_G and w_{2D}) of graphene on water that was floating on the surface of water for 0 hours, 19 hours, 4 days and 8 days.

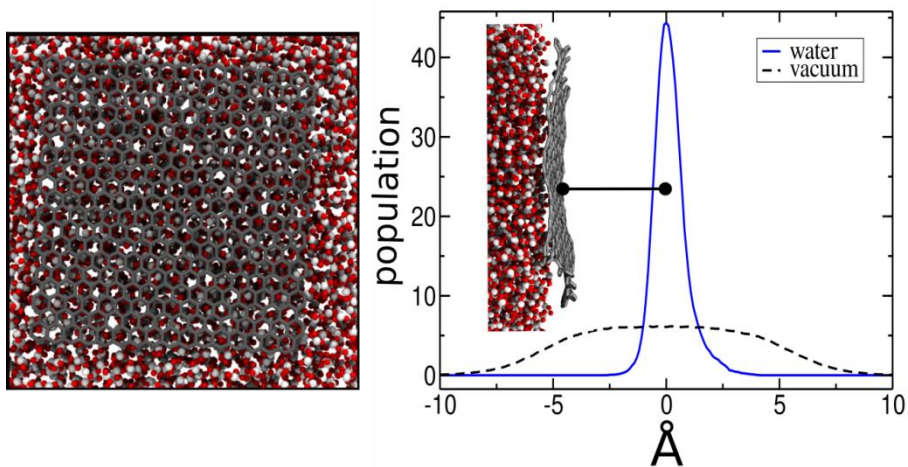


Figure A2.7. MD simulations of graphene on water surface versus graphene in vacuum.

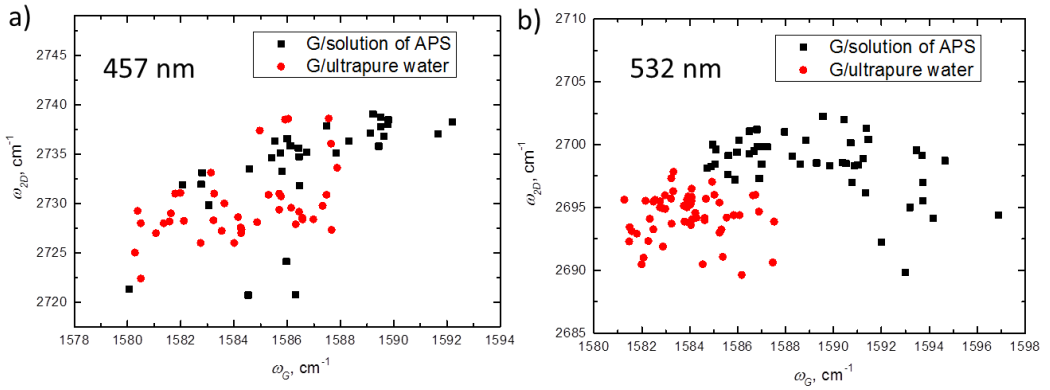


Figure A2.8. Correlation maps of G and 2D peaks frequencies of graphene in APS solution and ultrapure water. a) measured at the excitation wavelength of 457 nm. b) measured at the excitation wavelength of 532 nm.

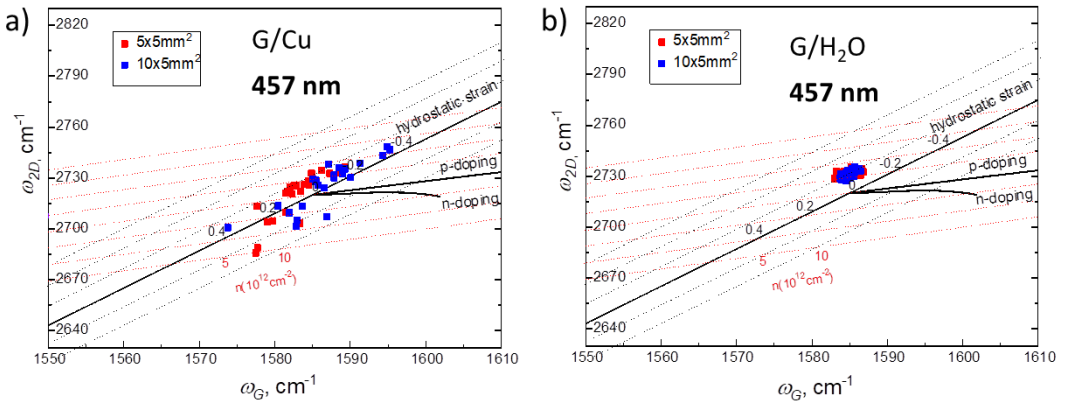


Figure A2.9. Effect of size on the strain and doping distribution in graphene. a) Correlation maps of G and 2D peaks frequencies of graphene/Cu samples in sizes 5 mm×10 mm and 10 mm×10 mm. b) Correlation maps of G and 2D peaks frequencies of graphene/water samples in sizes 5 mm×10 mm and 10 mm×10 mm.

References

1. Fu, W. *et al.* Graphene transistors are insensitive to pH changes in solution. *Nano Lett.* **11**, 3597–3600 (2011).
2. Belyaeva, L. A., Fu, W., Arjmandi-Tash, H. & Schneider, G. F. Molecular caging of graphene with cyclohexane: transfer and electrical transport. *ACS Cent. Sci.* **2**, 904–909 (2016).
3. Jiang, L., Fu, W., Birdja, Y. Y., Koper, M. T. M. & Schneider, G. F. Quantum and electrochemical interplays in hydrogenated graphene. *Nat. Commun.* **9**, 793 (2018).
4. Metten, D., Federspiel, F., Romeo, M. & Berciaud, S. Probing built-in strain in freestanding graphene monolayers by raman spectroscopy. *Phys. Status Solidi Basic Res.* **250**, 2681–2686 (2013).
5. Bendiab, N. *et al.* Unravelling external perturbation effects on the optical phonon response of graphene. *J. Raman Spectrosc.* **49**, 130–145 (2018).

APPENDIX 3

Supporting Information to Chapter 4

3.1. Methods

3.1.1. Materials

Two types of graphene were used: monolayer graphene on a copper substrate provided by Graphenea and graphene grown in a tube oven on a 25 μm copper foil at 1035° according to the procedure described in ref.¹. Before conducting contact angle experiments the backside of graphene-on-copper (G/Cu) was removed with O₂ plasma. Both types of graphene show the same results for water contact angle measurements. Multilayered graphene was prepared by repetitive PMMA transfer² of graphene on G/Cu.^{3,4} Highly Oriented Pyrolytic Graphite (*HOPG*, 7x7x0.8-1.8 mm with mosaic spread 0.8-1.2 degree) was purchased from NT-MDT.

3.1.2. Sample preparation

CVD graphene on a copper substrate was placed in a 0.3 M water solution of ammonium persulfate (APS) (98% Sigma-Aldrich). Once the copper foil was etched away the APS solution was repeatedly replaced with ultrapure water by sequential diluting steps yielding a clean graphene surface without any observable APS crystals.¹ In general, presence of ions in water has very small effect on the surface tension of water – in the order of 3% or lower at the concentration of 0.3 M⁵⁻⁷ – and, therefore, negligible effects on the measured contact angle. Consequently, and given the precautions undertaken to replace the etching APS solution by water, possible presence of residual ions had no effect on the contact angle measurements (the CA of graphene in 0.1 M FeCl₃ is equal to the CA of graphene in pure water, Figure A3.1 of this Appendix).

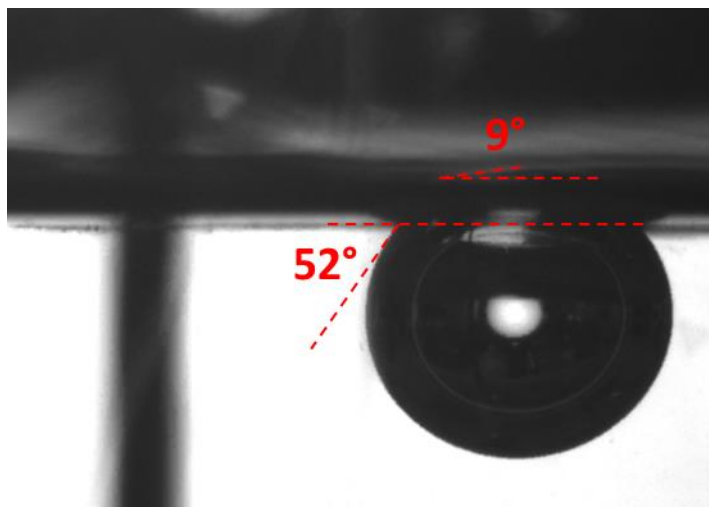


Figure A3.1. Contact angle of graphene on the surface of a 0.1 M aqueous solution of FeCl_3 . Presence of ions in concentrations below 0.3 M does not affect the measured contact angle, the contact angles of graphene in different etchant solutions are equal to the contact angle of graphene in pure water.

To place a 6 μl air bubble under the water-graphene-air interface, air was injected through a J-shaped inverted needle underneath the graphene (Figure 4.2a in Chapter 4). The contact angle was then measured at least five times at the three-phase line interface (Figure 4.2d in Chapter 4).

To improve the stability of graphene on the water surface, graphene was surrounded with a Langmuir–Blodgett film of 1,2-dipalmitoyl-*sn*-glycero-3-phosphocholine (DPPC) lipids (Avanti Polar Lipids Inc.) at a surface pressure of 30 mN m^{-1} as it is described in ref.^{8,9}. The lipids had a concentration of 1 mg mL^{-1} and were first dissolved in $\text{CHCl}_3/\text{CH}_3\text{OH}$ 3:1 vol %. First, graphene on copper¹ (copper facing down) was placed floating on the etchant solution and the appropriate amount of lipids (depending on the size of the graphene and of the cuvette) was added on the surface of the etchant solution around graphene. The etchant solution was then sequentially replaced with ultrapure water and the contact angle was measured. The lipids are known to only spread on the surface of water

(around the graphene) without adsorbing on its surface (as measured by infra-red spectroscopy).^{8,9}

Graphene surrounded with lipids showed a higher stability during the deposition of the air bubble. Both graphene samples, without and with lipids, showed similar measured contact angles, *i.e.* $42^\circ \pm 3^\circ$ and $42^\circ \pm 3^\circ$ respectively (Figure A3.2 of this Appendix), confirming the absence of lipids on the graphene surface.

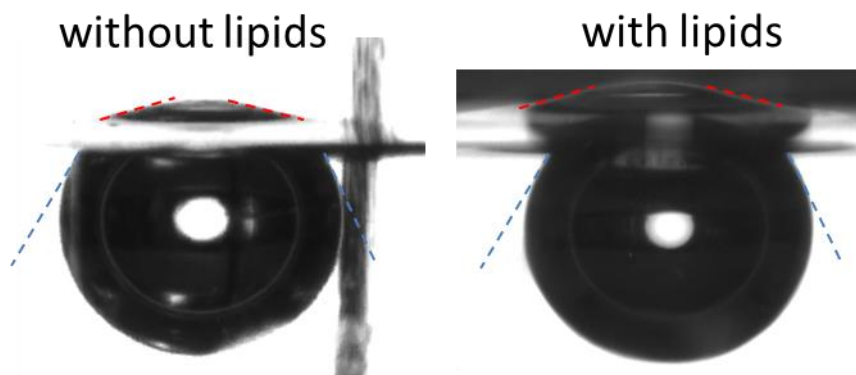


Figure A3.2. Captive bubble on graphene with (right) and without (left) a DPPC (1,2-dipalmitoyl-*sn*-glycero-3-phosphocholine) lipid scaffold. Lipids do not affect the contact angle value measured to be $42^\circ \pm 3^\circ$ in both situations.

Immobilizing the graphene with lipids is essential for contact angle measurement. If graphene is not stabilized with lipids, the action of placing the air bubble creates a momentum and pushes the graphene sheet away from the field of view of the camera, despite the fact that the bubble is stable and does not collapse.

For contact angle measurements of hydrogenated and oxygenated graphene, graphene was first hydrogenated (respectively, oxygenated) using a H_2 (respectively, O_2) plasma in a computer controlled Diener plasma generator for 247 seconds (1 mbar, 10 W).¹⁰

3.1.3. Raman spectroscopy

The quality and the number of layers of all graphene samples were characterized by Raman spectroscopy¹¹ at room temperature using a 100× objective and 457 nm and 532 nm lasers at a power below 2mW to avoid excessive thermal damage of graphene. Figure A3.3 of this Appendix displays typical Raman spectra of graphene on copper (Figure A3.3 a) and transferred onto a SiO₂/Si wafer (Figure A3.3 b). The shape of the 2D peak ($\sim 2700\text{ cm}^{-1}$), that can be fitted with a single Lorentzian component is indicative of single-layer graphene.¹¹ The absence of a D peak at $\sim 1370\text{ cm}^{-1}$ (Figure A3.3 a,b) suggests a low density of defects for non-treated graphene samples.¹¹

For hydrogenated and oxygenated graphene, however, the appearance of the D peak (Figure A3.3 c,d) results from the introduced sp³ defect sites.¹⁰ Particularly, the ratio $I(2D)/I(G)$ decreased from ~ 2 (pristine graphene) to ~ 1 after 4 min of hydrogen plasma treatment, indicating the effective doping in the lattice induced by hydrogenation.¹² Moreover, the appearance of a D' peak ($\sim 1620\text{ cm}^{-1}$) in hydrogenated graphene is also related to the activation of defects. The $I(D)/I(D')$ value of ~ 10 further confirms the sp³ nature of hydrogenated defects.¹³

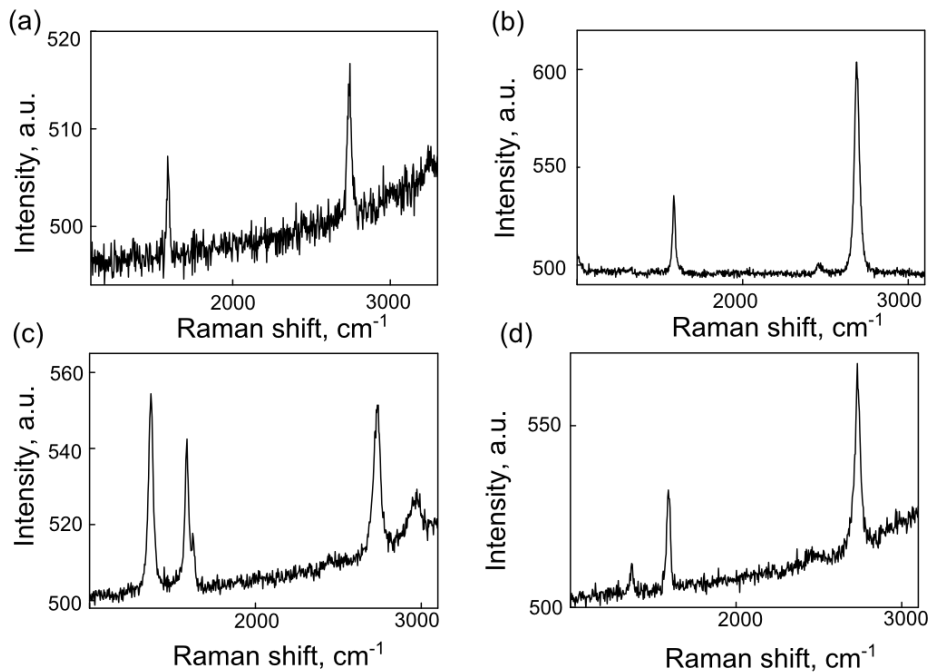


Figure A3.3. Raman spectra of CVD (chemical vapor deposition) graphene before and after plasma modification. (a) Non-treated graphene on Cu after the growth. (b) Non-treated graphene transferred onto a Si/SiO₂ wafer. (c) Graphene on Cu after H₂ plasma treatment. (d) Graphene on Cu after O₂ plasma treatment.

3.1.4. Optical microscopy

Optical images of graphene on water (Figure A3.4) and graphene transferred on silicon wafer were taken with a Leica optical microscope (DM 2700 M).

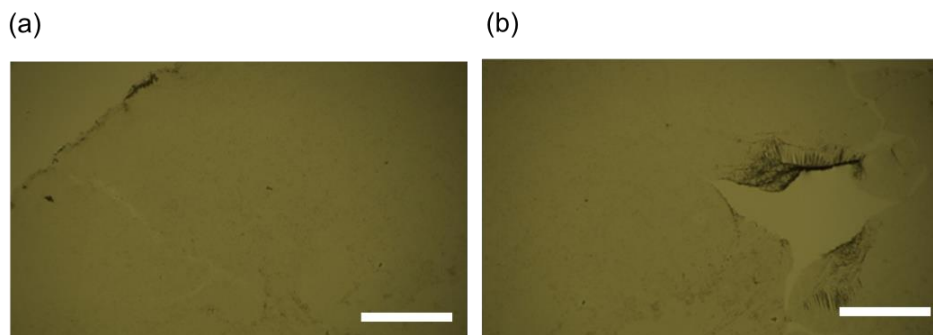


Figure A3.4. Optical images of graphene floating on the surface of water. (a) Before captive bubble measurement. The scale bar represents 500 μm . (b) After captive bubble measurement. The scale bar represents 500 μm .

3.1.5. Contact angle measurements

Contact angle measurements were conducted with a standard Ramé-Hart 250 goniometer (Netcong, NJ) and recorded with the DROPimage advanced v 2.8 software under ambient conditions (22°C). Two methods were used for the characterization of wetting. For the sessile drop technique a water droplet of 5-7 μL was deposited on a substrate and contact angle was measured within five seconds. For the captive bubble method, an air bubble with a volume of 6 μL was supplied with a microsyringe at the interface with an inverted needle (28 gauge, 304 SS Ramé-Hart). The analysis of contact angles from recorded videos were made with the software ImageJ (Drop snake analysis).

3.1.6. Measurements at different humidities

Experiments with controlled humidities were carried out using the saturated salt solution method, commonly used for accurate humidity control and the calibration of hygrometers.⁵⁷⁻⁵⁹ For that, an oversaturated salt solution is placed in a closed box and certain equilibrium vapor pressure (and thus relative humidity) is created. The oversaturation of the solution assures that the built vapor pressure is stable to presence of moisture sources and sinks (the excess of the salt precipitates and the solution remains saturated with the vapor pressure

unchanged) and, therefore, provides a precise humidity level. Different salts have different saturated vapor pressures at a given temperature, and the humidity thus can be varied by changing the chemical composition of the salt.

For the experiments oversaturated solutions of KCl for the humidity of $85.11 \pm 0.29\%$ ¹⁵ and K_2SO_4 for the humidity of $97.59 \pm 0.53\%$ were used.¹⁵ For measurements at every given humidity a beaker with the corresponding salt solution was placed in a sealed glass chamber with an embedded syringe (for further contact angle measurements) together with the cuvette containing graphene floating on water. Then the contact angle was measured using the captive bubble method. The relative humidity of 50% was the standard ambient humidity of the laboratory maintained by a moisture extractor and measured by a hygrometer, and the contact angle measurements were conducted without salt solutions.

3.2. Surface energy calculation

The surface energy and its components were calculated from the contact angle measurement of different liquids on target surfaces using the Owens-Wendt technique.¹⁸ Ultrapure water, ethanol, ethylene glycol, diiodomethane, methylnaphthalene were used as test liquids.

Surface energies of bare PMMA (poly(methyl methacrylate)) and PMMA-coated graphene samples were calculated according the Owens-Wendt model.¹⁹ Based on the contact angle measurements with liquids of different polarities, the Owens-Wendt equation allows for the determination of total surface energy of a solid and its polar and dispersive components:

$$\gamma_{lv}(1 + \cos \theta) = 2(\sqrt{\gamma_s^d \gamma_l^d} + \sqrt{\gamma_s^p \gamma_l^p})$$

The polar and dispersive components of liquids γ_L^P and γ_L^D were determined by measuring contact angles (sessile drop method) and applying the Owens/Wendt Theory for PTFE (teflon), which is a solid with known polar and dispersive

components of the surface tension ($\gamma_s^p=0 \text{ mN m}^{-1}$, $\gamma_s^d=18 \text{ mN m}^{-1}$). The determined surface tensions and their components of all used liquids are listed in Table A3.1.

Then contact angles of bare and PMMA-coated graphene with the liquids listed in Table A3.1 were measured. The results were plotted as $\frac{\gamma_L(\cos\theta+1)}{2\sqrt{\gamma_L^D}}$ versus $\frac{\sqrt{\gamma_L^P}}{\sqrt{\gamma_L^D}}$ for each substrate and the dependences were fitted linearly. The slope of the plot equals $\sqrt{\gamma_s^P}$ and the intercept equals $\sqrt{\gamma_s^D}$. The squares of the latter two equal γ_s^P and γ_s^D respectively. The resulting surface tensions and their polar and dispersive components are presented in Table A3.2 below and charted in Figure 4.1c of Chapter 4.

Table A3.1. Calculated surface tensions, polar and dispersive components of tested liquids

Liquid	γ_L^P , mJ m ⁻²	γ_L^D , mJ m ⁻²	γ_L^{total} , mJ m ⁻²
Water	51	21.8	72.8 ± 2.4
Ethylene glycol	19.2	28.8	48.0 ± 1.9
10% Ethanol in water	36.1	23.9	60.0 ± 2.2
Diiodomethane	0	50.8	50.8 ± 2.3
1-Methylnaphthalene	0	42.0	42.0 ± 1.1

Table A3.2. Calculated surface tensions, polar and dispersive components of PMMA, freshly PMMA-coated graphene and PMMA-coated graphene aged for six days

Surface energy/Sample	PMMA	Graphene on PMMA	Graphene on PMMA after 6 days
γ_s^P , mN m ⁻¹	9.8±1.6	10.8±1.5	9.1±1.4
γ_s^D , mN m ⁻¹	41.9±1.3	39.1±2.1	30.6±2.4
γ_D^{total} , mN m ⁻¹	51.6±2.3	47.9±1.6	39.7±1.5

3.3. References

1. Belyaeva, L. A., Fu, W., Arjmandi-Tash, H. & Schneider, G. F. Molecular caging of graphene with cyclohexane: transfer and electrical transport. *ACS Cent. Sci.* **2**, 904–909 (2016).
2. Suk, J. W. *et al.* Transfer of CVD-grown monolayer graphene onto arbitrary substrates. *ACS Nano* **5**, 6916–6924 (2011).
3. Batrakov, K. *et al.* Flexible transparent graphene/polymer multilayers for efficient electromagnetic field absorption. *Sci. Rep.* **4**, 7191 (2014).
4. Wu, B. *et al.* Experimental demonstration of a transparent graphene millimetre wave absorber with 28% fractional bandwidth at 140 GHz. *Sci. Rep.* **4**, 1–7 (2014).
5. Weissenborn P.K., Pugh, R. J. Surface tension of aqueous solutions of electrolytes: relationship with ion hydration, oxygen solubility, and bubble coalescence. *J. Colloid Interface Sci.* **184**, 550–563 (1996).
6. Hård, S. & Johansson, K. The surface tension of concentrated aqueous solutions of 1:1-electrolytes measured by means of Wilhelmy and laser light scattering methods. *J. Colloid Interface Sci.* **60**, 467–472 (1977).
7. Dutcher, C. S., Wexler, A. S. & Clegg, S. L. Surface tensions of inorganic multicomponent aqueous electrolyte solutions and melts. *J. Phys. Chem. A* **114**, 12216–12230 (2010).
8. Lima, L. M. C., Fu, W., Jiang, L., Kros, A. & Schneider, G. F. Graphene-stabilized lipid monolayer heterostructures: a novel biomembrane superstructure. *Nanoscale* **8**, 18646–18653 (2016).
9. Lima, L. M. C., Arjmandi-Tash, H. & Schneider, G. F. Lateral non-covalent clamping of graphene at the edges using a lipid scaffold. *ACS Appl. Mater. Interfaces* **10**, 11328–11332 (2018).
10. Jiang, L., Fu, W., Birdja, Y. Y., Koper, M. T. M. & Schneider, G. F. Quantum and electrochemical interplays in hydrogenated graphene. *Nat. Commun.* **9**, 793 (2018).
11. Ferrari, A. C. Raman spectroscopy of graphene and graphite: Disorder, electron-phonon coupling, doping and nonadiabatic effects. *Solid State Commun.* **143**, 47–57 (2007).

12. Das, A. *et al.* Monitoring dopants by Raman scattering in an electrochemically top-gated graphene transistor. *Nat. Nanotechnol.* **3**, 210–215 (2008).
13. Eckmann, A. *et al.* Probing the nature of defects in graphene by Raman spectroscopy. *Nano Lett.* **12**, 3925–3930 (2012).
14. Wexler, A., Brombacher, W. G. Methods of measuring humidity and testing hydrometers. *National Bur. Stand.* **512**, 1–18 (1951).
15. Greenspan, L. Humidity fixed points of binary saturated aqueous solutions. *J. Res. Natl. Bur. Stand. Sect. A Phys. Chem.* **81A**, 89 (1977).
16. Lu, T. & Chen, C. Uncertainty evaluation of humidity sensors calibrated by saturated salt solutions. *Meas. J. Int. Meas. Confed.* **40**, 591–599 (2007).
17. Carotenuto, A. & Dell’Isola, M. An experimental verification of saturated salt solution-based humidity fixed points. *Int. J. Thermophys.* **17**, 1423–1439 (1996).
18. Kaelble, D. H. Dispersion-polar surface tension properties of organic solids. *J. Adhes.* **2**, 66–81 (1970).
19. Owens, D. K. & Wendt, R. C. Estimation of the surface free energy of polymers. *J. Appl. Polym. Sci.* **13**, 1741–1747 (1969).

APPENDIX 4

Supporting Information to Chapter 5

4.1. Methods

4.1.1. Graphene synthesis and transfer

Two types of CVD graphene were used: commercially purchased from Graphenea and synthesized in a cold-wall CVD oven.^{1,2} For the latter, a copper foil with a thickness of 25 μm was annealed at 1035°C and the monolayer graphene films were grown according to the protocol described in ref.³. After the CVD synthesis, the graphene grown on the backside of the copper foil was removed by using oxygen plasma. Multilayer samples were purchased from Graphenea, where they were fabricated by the “repeat transfer” of monolayer graphene sheets on top of each other.

After etching the graphene on the backside of the copper foil, graphene samples were transferred to ice, hydrogel, PDMS and SiO₂/Si.

Graphene-on-ice. Copper with graphene on top was etched in an aqueous solution of 0.5 M ammonium persulfate (APS). After complete etching of the copper, the solution was placed at -20°C until the liquid was completely solidified. For several samples we replaced the etchant solution with pure water after the etching, with no effects on resulting contact angles (Figure A4.1 of this Appendix).

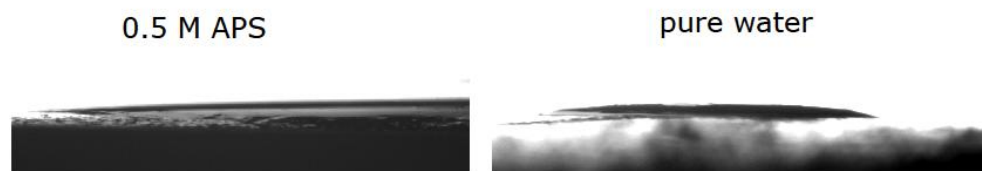


Figure A4.1. Water contact angle on frozen 0.5 M water solution of ammonium persulfate (APS) and pure water ice

Graphene-on-hydrogel. To ensure that the agarose-water ratio at this surface was the same as the bulk agarose-water ratio, a polystyrene petri dish was exposed to oxygen plasma for one minute to render the surface hydrophilic. A 4% agarose gel in deionized water was poured into the petri dish and then cut to 1 cm³ cubes. With the side that had set against the hydrophilic glass surface facing up, the cubes were submerged halfway in 0.5 M APS, with a graphene/copper sample placed on top. Etching began when the APS solution diffused through the

gel matrix to the surface of copper. Typically complete copper etching occurred after 12 to 18 hours, resulting in a graphene layer 'floating' on top of the hydrogel. The sample was then soaked in pure water in order to replace the solution of ammonium persulfate and copper (II) ions with pure water. The integrity of graphene after this long etching time was confirmed by Raman spectroscopy.

Graphene on PDMS. A mixture of a silicone elastomer base and a silicone elastomer curing agent (Sylgard[®] 184, weight ratio 10:1) was prepared and left in the fridge for 1.5 hours for degassing. Then a graphene/copper piece was placed onto PDMS with the copper side facing upwards. After that, PDMS was cured in an oven at 80°C for one hour. When PDMS was solidified the PDMS/graphene/copper stack was placed on the surface of 0.5 M water solution of ammonium persulfate for etching the copper. After copper was etched graphene was rinsed with water to wash away the ammonium persulfate salt crystals. Then the contact angle was measured. Before preparing graphene-on-PDMS sample, graphene on copper was annealed and then placed onto PDMS with the copper side facing upwards, such that hydrocarbons adsorption was avoided for these samples. Thus, graphene was only exposed to air for a time period not longer than 5 minutes. The surface morphology of graphene on PDMS was inspected using AFM (Figure A4.2 of this Appendix).

Graphene on SiO₂/Si. To transfer graphene onto a SiO₂/Si wafer we used the conventional PMMA-assisted method reported in ref.⁴. Prior to the transfer, wafers were cleaned in several steps following a procedure similar to described in ref.⁵⁻⁷ The wafers were first cleaned with cotton swap soaked with ethanol to remove big particles. Thereafter, the wafers were rinsed with water, acetone, isopropanol and ethanol and blow-dried with argon. Then the wafers were immersed in a piranha solution for 5 minutes (1 part H₂O₂ and 3 parts H₂SO₄) to remove residues of the organic solvents and, finally, rinsed with ultrapure water. The surface morphology of graphene on SiO₂/Si was inspected using AFM (Figure A4.2 of this Appendix).

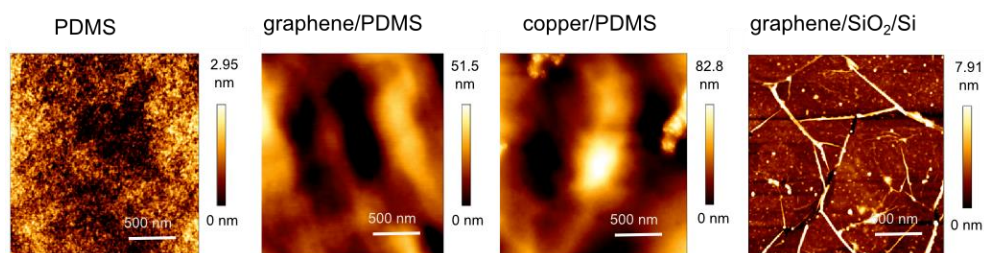


Figure A4.2. Surface morphology of PDMS and SiO₂/Si graphene substrates imaged by AFM. The high corrugation of graphene on PDMS compared to bare PDMS stems from the copper foil on which graphene was grown and brought into contact with PDMS before it was cured. For PDMS deposited on bare copper (no graphene present) and graphene on PDMS similar roughness is seen. The contact angle on the graphene-on-PDMS surface may be influenced by the corrugation and no longer governed by wetting transparency. Graphene deposition on SiO₂/Si involves polymer transfer, and typically results in wrinkled graphene and even polymer residues, resulting in poorer conformity and irreproducible contact angles

4.1.2. Contact angle measurements

Contact angle measurements are very sensitive to any contamination of the surface, therefore, great care should be taken in order to keep the samples as clean as possible. Liquids that were used for contact angle measurements are listed in Table A4.1 of this Appendix.

Table A4.1. Solvents for contact angle measurements

Test liquid	σ_L , mN/m	σ_L^D , mN/m	σ_L^P , mN/m	Freezing point, °C	Substrates
water	72.8	26.4	46.4	0	Ice, hydrogel, SiO ₂ /Si, PDMS, copper
diiodomethane	50.8	44.4 to 50.8	0	5.4 to 6.2	Hydrogel, SiO ₂ /Si, PDMS, copper
1- methylnaphtalene	30.06- 38.7	20.6	0.8	-22	Hydrogel
methylbenzoate	37.2	27	10.2	-12.5	Ice, SiO ₂ /Si, PDMS, copper
nitromethane	36.5	22	14.5	-29	Ice, SiO ₂ /Si, PDMS, copper
ethylene glycol	47.7	26.4	21.3	-12.9	Ice, SiO ₂ /Si, PDMS, copper
formamide	57	39	19	2 to 3	SiO ₂ /Si, PDMS, copper

Graphene-on-ice

Contact angle (CA) measurements with ice were performed at 0°C (with pure water) and -20°C (water with addition of nitric acid). Although experiments with ice are fairly straightforward, one should account for several technical difficulties accompanying measurements at temperatures below 0°, namely condensation and freezing of the droplet. We minimized the effect of condensation by constantly flushing the chamber with dry air. Control experiments with graphite and a Si/SiO₂ wafer confirmed no effect of condensation on the water contact angle (see Figure A4.3 of this Appendix). Control experiments with graphite at temperatures below 0°C showed that the addition of nitric acid has negligible effects on the contact angle. Contact angles with pure water and 18% nitric acid

are equal within the margins of experimental error (see Figure 5.2a of Chapter 5).



Figure A4.3. Control water contact angle on SiO₂/Si under ambient conditions (left) and under conditions identical to the measurements with ice (right). For the latter the wafer was placed on the surface of water solution of ammonium persulfate and then cooled down to -20°C in Peltier chamber with constant flushing the chamber with dry air. No significant difference in WCA was detected

Raman characterization was not possible for graphene on ice. Ice starts melting as soon as the laser hits the graphene surface, and even when kept in cold. Additionally, the signal from ice appears to be much more intensive not allowing to detect any of the graphene typical bands. A typical Raman spectrum of graphene on ice is presented in Figure A4.4 of this Appendix.

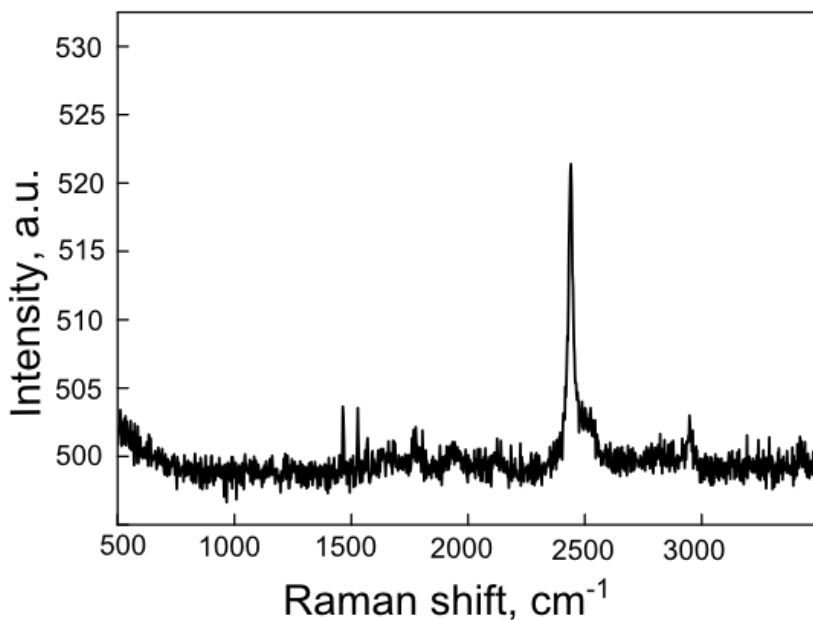


Figure A4.4. Typical Raman spectrum of graphene on ice (laser wavelength 532 nm): no graphene bands are detectable.

For ice we cannot completely avoid exposure to ambient air, those samples are normally exposed air for 1-1.5 hour. For that reason, experiments in controlled atmosphere were performed on graphene that had been minimally exposed to ambient atmosphere. Graphene on copper was thermally annealed and then directly transferred into the controlled N₂ atmosphere of a glove bag (Aldrich® Atmosbag), where etching was performed. The sample was then cooled down at -20°C. Contact angles were then taken in ambient atmosphere within 5 min and did not show any measurable difference between the samples measured in ambient and controlled atmospheres (Figure A4.5 of this Appendix).

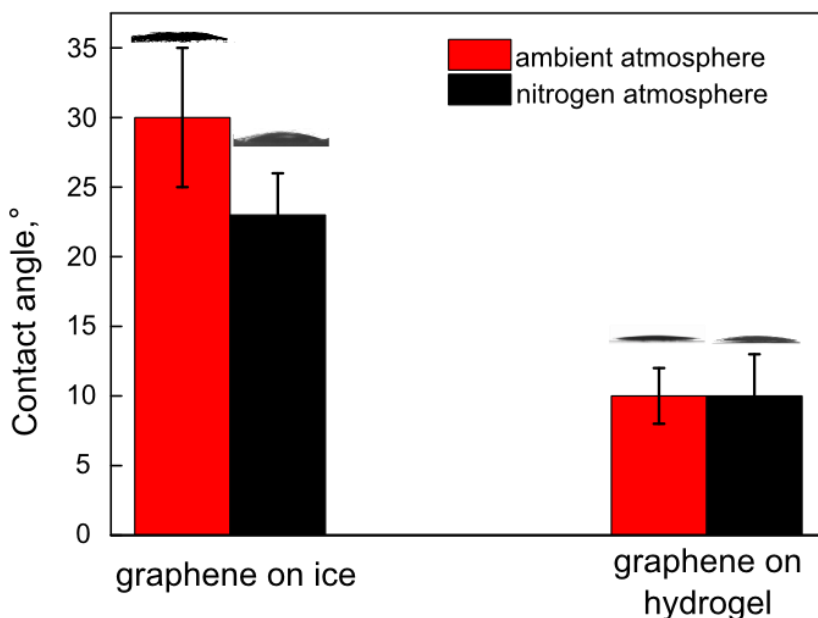


Figure A4.5. Water contact angles of graphene on ice and graphene on hydrogel prepared in ambient atmosphere (red) and controlled atmosphere of nitrogen (black)

Graphene-on-hydrogel

A 4% agarose (w/w) was used to support CVD grown graphene from the beginning of the etching process until CA is measured. To confirm that during the contact angle measurements the hydrogel matrix did not contain any impurities and/or residuals from the etching process of copper, Atomic Force Microscopy (AFM) and Raman spectroscopy were performed on graphene-on-hydrogel (Figure A4.6 of this Appendix).

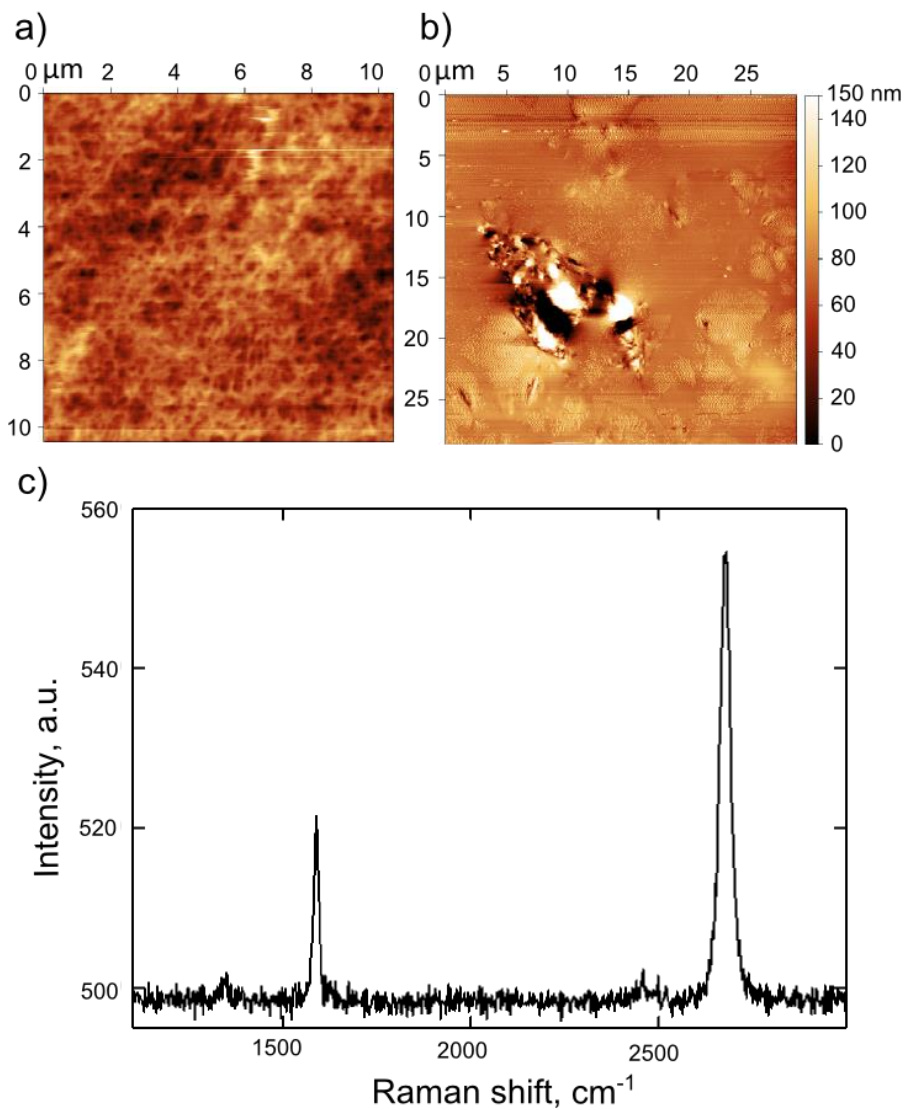


Figure A4.6. Characterization of graphene on hydrogel. a) AFM image of bare hydrogel. b) AFM image of graphene on hydrogel. c) Raman spectrum of graphene on hydrogel.

For hydrogel we cannot completely avoid exposure to ambient air, those samples are normally exposed air for 13-18 hours. For that reason, experiments in

controlled atmosphere were performed on graphene that had been minimally exposed to ambient. Graphene on copper was thermally annealed and directly transferred into the controlled N₂ atmosphere of a glove bag (Aldrich® Atmosbag), where etching on hydrogel was performed. Contact angles were then taken in ambient atmosphere. The total time that the graphene surface was exposed to ambient conditions before contact angle measurement never exceeded 5 minutes (Figure A4.5 of this Appendix). These control experiments did not show any measurable difference between the samples measured in ambient and controlled atmospheres (Figure A4.5 of this Appendix).

In addition to the linear extrapolation for diiodomethane (Figure 5.2c of Chapter 5), the linear extrapolation of the CA of 1-methylnaphtalene on hydrogel based on agarose concentration of 1 to 4% agarose was also made, showing that the CA of 1-methylnaphtalene on water would be 25° (Figure A4.7 of this Appendix).

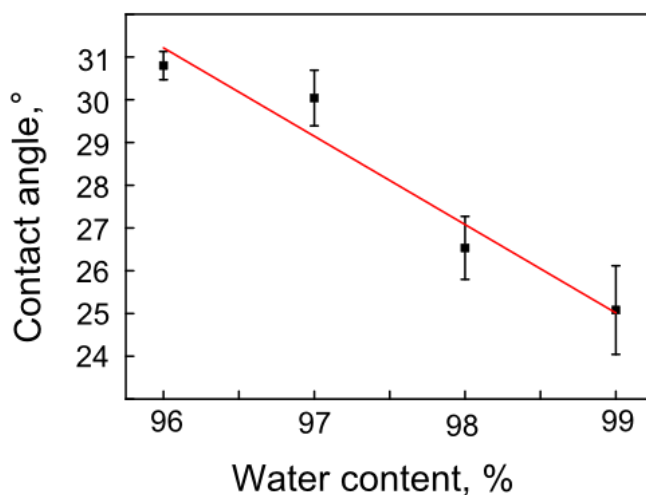


Figure A4.7. Hydrogel as a water model: contact angle of 1-methylnaphtalene on an agarose hydrogel with different water content

Graphene on copper, SiO₂/Si and PDMS

Graphene on copper, SiO₂/Si and PDMS were prepared as described in the above section. The transferred samples were then annealed at 550°C for one hour

under 100 mbar. Contact angle measurements were conducted within 3 min after the annealing. In general, no difference in contact angle was detected for samples probed right after the annealing and 48 hours later (see Figure A4.8 of this Appendix).

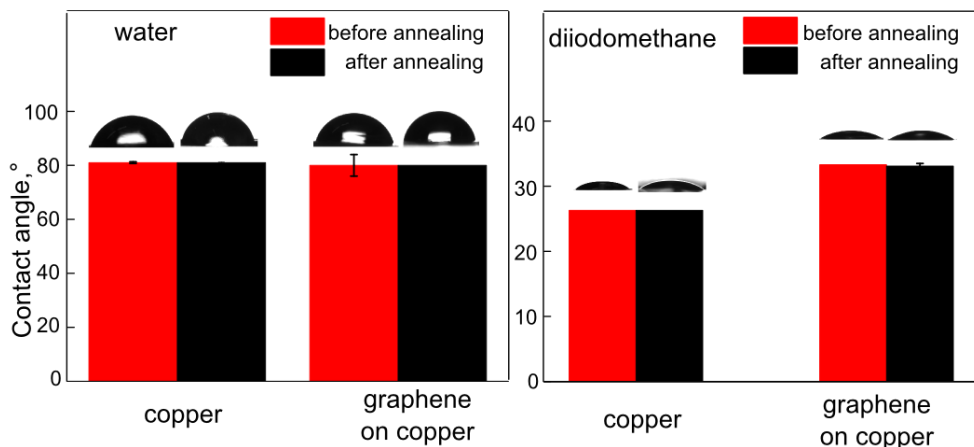


Figure A4.8. Contact angles of copper and graphene on copper with water and diiodomethane before and after annealing.

Contact angles of mono-, bi-, tri- and four-layer graphene on copper with water and diiodomethane did not show measurable difference (Figure A4.9 of this Appendix).

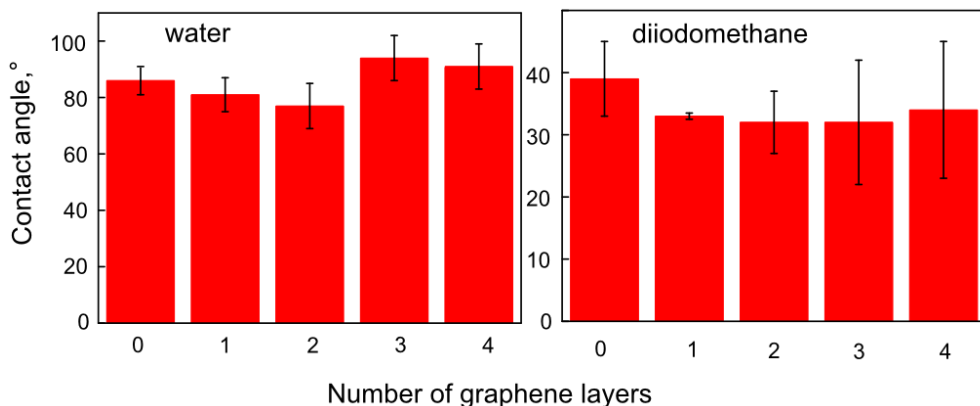


Figure A4.9. CA of water and diiodomethane on mono-, bi-, three- and four-layer graphene on copper.

Samples of graphene transferred to SiO₂/Si substrates showed high sample-to-sample variations and irreproducible contact angle values (Figure A4.10 of this Appendix).



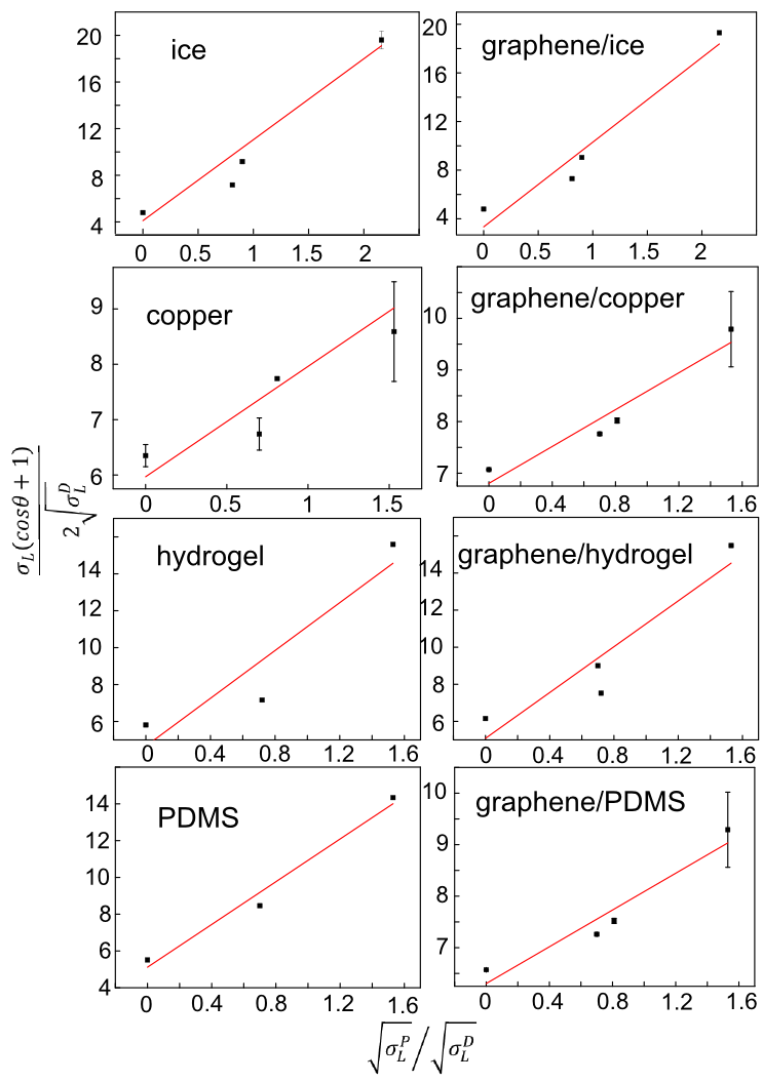
Figure A4.10. Irreproducibility of the WCA of graphene transferred onto SiO₂/Si wafers: WCA of bare SiO₂/Si wafer and WCA of graphene transferred onto SiO₂/Si wafer for different samples.

PDMS samples underwent exactly the same treatment steps as graphene/PDMS samples: after curing, PDMS was incubated in the APS solution for one hour, then rinsed with water and then the contact angle was measured.

4.2. Calculation of polar and dispersive components by Owens-Wendt

method

Contact angles of all samples with the liquids listed in Table A4.1 of this Appendix were measured. Then the results were plotted as $\frac{\sigma_L(\cos\theta+1)}{2\sqrt{\sigma_L^D}}$ versus $\frac{\sqrt{\sigma_L^P}}{\sqrt{\sigma_L^D}}$ (see Figure A4.11 of this Appendix) for each substrate and the dependences were fitted linearly. The slope of the plot equals $\sqrt{\sigma_S^P}$ and the intercept equals $\sqrt{\sigma_S^D}$. The square of the latter two equals σ_S^P and σ_S^D respectively.



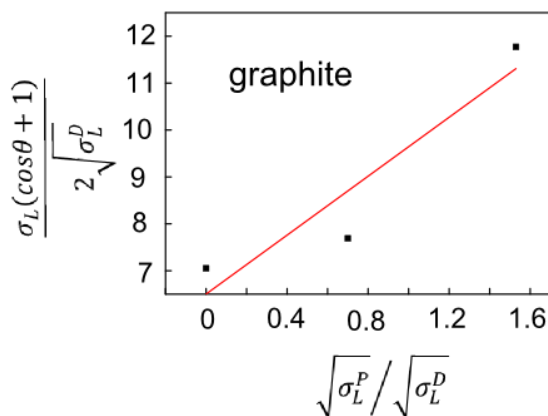


Figure A4.11. Owens-Wendt plots for ice, graphene/ice, copper, graphene/copper, hydrogel, graphene/hydrogel, PDMS, graphene/PDMS and graphite.

4.2.1. Calculation of the polar and dispersive components for 18% HNO₃

To determine the polar and dispersive components of 18% HNO₃ we applied the Owens/Wendt Theory for teflon, which is a solid with known polar and dispersive components of the surface tension ($\sigma_s^P=0\text{mN/m}$, $\sigma_s^D=18\text{ mN/m}$). CA between the teflon plate and nitric acid solution was found to be $96.8^\circ\pm 0.2$. The total surface tension of 18% HNO₃ was calculated according the model described in ref.⁸ and is equal to 69.26 mN/m.

In this way the Owens/Wendt equation reduces to $\sigma_L^D = \frac{(\sigma_L(\cos\theta+1))^2}{72} = 57\text{ mN/m}$ and $\sigma_L^P = \sigma_L - \sigma_L^D = 12.26\text{ mN/m}$.

4.2.2. Comparison with the Fowkes method

Surface energies calculated by Owens-Wendt and Fowkes methods agree within experimental error margins (Figure A4.12 of this Appendix).

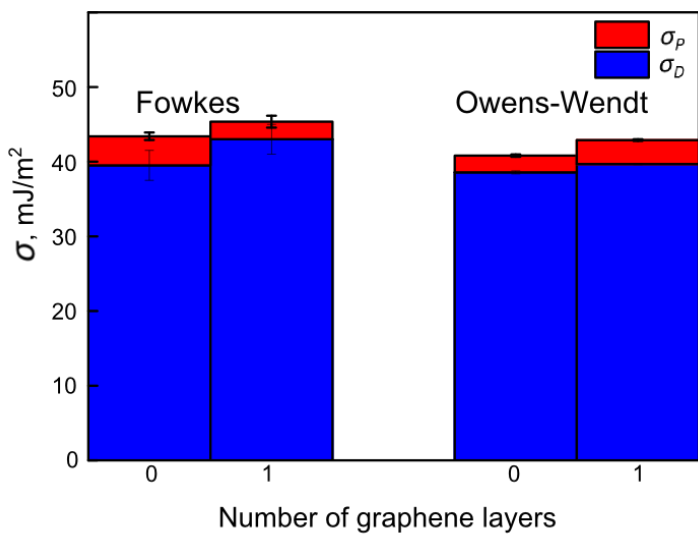


Figure A4.12. Polar and dispersive components of the surface tensions of bare copper and graphene/copper calculated by Fowkes and Owens-Wendt models.

4.3. References

1. Pierson, H. O. *Handbook of chemical vapor deposition (CVD)*. (Noyes Publications / William Andrew Publishing, LLC, 1999).
2. Muñoz, R. & Gómez-Aleixandre, C. Review of CVD synthesis of graphene. *Chem. Vap. Depos.* **19**, 297–322 (2013).
3. Arjmandi-Tash, H., Lebedev, N., van Deursen, P., Aarts, J. & Schneider, G. F. Hybrid cold and hot-wall chamber for fast synthesis of uniform graphene. *Carbon N. Y.* **118**, 438–442 (2017).
4. Suk, J. W. *et al.* Transfer of CVD-grown monolayer graphene onto arbitrary substrates. *ACS Nano* **5**, 6916–6924 (2011).
5. Wang, Q. H. *et al.* Understanding and controlling the substrate effect on graphene electron-transfer chemistry via reactivity imprint lithography. *Nat. Chem.* **4**, 724–732 (2012).
6. Shim, J., Rivera, J. A. & Bashir, R. Electron beam induced local crystallization of HfO₂ nanopores for biosensing applications. *Nanoscale* **5**, 10887–93 (2013).
7. Kim, S. S. *et al.* Strain-assisted wafer-scale nanoporation of single-layer graphene by arrayed Pt nanoparticles. *Chem. Mater.* **27**, 7003–7010 (2015).
8. Dutcher, C. S., Wexler, A. S. & Clegg, S. L. Surface tensions of inorganic multicomponent aqueous electrolyte solutions and melts. *J. Phys. Chem. A* **114**, 12216–12230 (2010).

APPENDIX 5

Supporting Information to Chapter 6

5.1. Methods

5.1.1. Sample preparation

All graphene samples were grown using the same CVD protocol.¹ The as-grown samples were grown directly on Cu(111) and on polycrystalline copper substrates that were further studied in TPD. The transferred graphene was first grown on copper foil and then transferred to a polycrystalline copper substrate using the PMMA-assisted transfer method.² All samples were characterized with Raman spectroscopy at an excitation wavelength of 457 nm.

5.1.2. TPD measurements

TPD experiments were performed in a home-built UHV apparatus with a differentially pumped quadrupole mass spectrometer.³ The procedure that corrects for the changing background pressure during a TPD experiment has also been described previously.⁴ After introducing copper samples with transferred or as-grown graphene into the UHV chamber, the samples were annealed at modest temperatures (~ 400 K) to remove contaminants. Ultrahigh purity water was dosed from a capillary array doser onto the sample. After a series of water TPD spectra for various water coverages on graphene were obtained, graphene was removed by cycles of Ar⁺ sputtering at 1 kV and annealing at ~ 900 K. From the cleaned Cu substrates, water desorption was also studied by the same procedures. All TPD spectra were obtained using a temperature ramp of ~ 1.0 K/s.

5.1.3. Contact angle measurements

To prevent copper oxidation upon exposure to air, bare copper crystals were annealed at 500°C in hydrogen atmosphere. The contact angles were measured right after (*i.e.* within 1-2 minutes) and 30 minutes after the annealing. When graphene is grown on copper substrate (which was pre-annealed), it protects the copper surface from oxidation, and, therefore, no copper oxide layer was formed in the samples of graphene grown on copper. However, to remove the adsorbed airborne hydrocarbons⁵ all graphene samples were also annealed right before

contact angle measurements. Additional Raman spectra of the Cu samples were taken after removal of graphene by sputtering in UHV and re-exposing the samples to air.

5.2. References

1. Fu, W. *et al.* Graphene transistors are insensitive to pH changes in solution. *Nano Lett.* **11**, 3597–3600 (2011).
2. Suk, J. W. *et al.* Transfer of CVD-grown monolayer graphene onto arbitrary substrates. *ACS Nano* **5**, 6916–6924 (2011).
3. Badan, C., Koper, M. T. M. & Juurlink, L. B. F. How well does Pt(211) represent Pt[n (111) × (100)] surfaces in adsorption/desorption? *J. Phys. Chem. C* **119**, 13551–13560 (2015).
4. den Dunnen, A., van der Niet, M. J. T. C., Koper, M. T. M. & Juurlink, L. B. F. Interaction between H₂O and preadsorbed D on the stepped Pt(553) surface. *J. Phys. Chem. C* **116**, 18706–18712 (2012).
5. Li, Z. *et al.* Effect of airborne contaminants on the wettability of supported graphene and graphite. *Nat. Mater.* **12**, 925–931 (2013).

Samenvatting

Dit proefschrift verbreedt onze kennis over de interactie tussen grafeen en vloeistofoppervlakken, in het bijzonder aangaande de effecten die vloeistoffen hebben op de structurele, elektronische en mechanische eigenschappen van grafeen. Daarnaast biedt het experimentele oplossingen en methodes, gebruikmakend van vloeistoffen, om het gebruik en de karakterisatie van grafeen te vergemakkelijken. In andere woorden, vloeistoffen en vloeistofoppervlakken veranderen gedurende dit proefschrift van studieonderwerp tot studievoorwerp en *vice versa*.

Hoofdstuk 2 laat zien hoe een tweefasensysteem bestaande uit twee onmengbare vloeistoffen gebruikt kan worden voor het verplaatsen van grafeen. Enerzijds vermijdt deze methode polymeervervuilingen die kenmerkend zijn voor de gebruikelijke verplaatsingsmethodes, en anderzijds versterkt het de grafeenstructuur, waardoor scheuren en vouwen van het grafeen wordt voorkomen. Dit is in contrast met andere polymeer-vrije verplaatsingsmethodes. Dit komt doordat de aanwezigheid van vloeistof boven en onder het grafeen mechanische steun verleent en een beschermlaag vormt voor het grafeen, zoals een vast substraat of polymeerlaag dat ook doet. In het bijzonder kan gesteld worden dat vloeistoffen een meer flexibele mogelijkheid geven voor de verplaatsing en gebruikmaking van grafeen, omdat hun eigenschappen *in situ* kunnen worden aangepast middels het mengen met andere vloeistoffen, bevroering, verdamping, etcetera. Bijvoorbeeld, een laag cyclohexaan bovenop grafeen kan worden bevroren om een zacht plastic polymorf kristaal te vormen (gelijk een beschermende polymeerlaag), welke na de verplaatsing kan worden verwijderd door directe sublimatie van de vaste fase naar de gasfase. Daarnaast wordt in hoofdstuk 2 een vloeistofgrensvlak (namelijk die van cyclohexaan en water, met daartussen grafeen) geïsoleerd om de elektronentransport door de grafeenlaag te bestuderen. Hier dient te worden opgemerkt dat de zogeheten *charge carrier mobility* groter was dan die gemeten werd op vaste substraten.

Daarna laat hoofdstuk 3 zien wat de voornaamste redenen zijn voor de verbeterde elektronische eigenschappen van grafeen wanneer het zich op het vloeistofgrensvlak bevindt, versus wanneer het zich op een vast substraat

bevindt, zijnde een verlaagde oppervlaktespanning en doping niveaus. Het is interessant om op te merken dat oppervlaktespanning al reeds lang bekend staat als een belangrijke factor voor de verslechterde elektronische eigenschappen van grafeen, en apparaten die hierop zijn gebaseerd, maar dat dit onmogelijk te voorkomen is aangezien vaste substraten niet perfect complementair zijn met de morfologie van grafeen en zodoende de homogeniteit van het grafeenoppervlak kunnen verstoren. Vloeistofoppervlakken, daarentegen, zijn homogeen van aard en volgen de morfologie van grafeen, ongeacht hun chemische samenstelling.

Hoofdstukken 4 en 5 demonstreren hoe vloeistoffen gebruik kunnen worden in toepassingen waar het gebruik van vaste substraten onpraktisch is. Het idee om vloeistoffen, in het bijzonder water, te gebruiken als studieonderwerp en tegelijkertijd als studievoorwerp blijkt bijzonder gunstig voor het bestuderen van de zogeheten *wettability* van grafeen. In tegenstelling tot vaste stoffen, is de zittende druppel configuratie instabiel op vrijstaand grafeen: grafeen breekt, als gevolg van zwaartekracht en de oppervlaktespanning van water. Echter, grafeen is geheel stabiel in de omgekeerde configuratie waar het water zich onder het grafeen bevindt ter ondersteuning; injectie van een luchtbel onder het drijvende grafeen resulteert in een omgekeerd (maar aan de zittende druppel configuratie gelijk zijnde) water-grafeen-lucht grensvlak, waardoor een betrouwbare contacthoekmeting kan worden uitgevoerd (Hoofdstuk 4). In hoofdstuk 5 zal water wederom, dit keer in de vorm van ijs en *hydrogels*, gebruikt worden als steunlaag voor grafeen, dit keer om de veel bediscussieerde *wetting transparency* van grafeen in water te onderzoeken. Tesaamen geven hoofdstukken 4 en 5 een aantal fundamentele inzichten: 1) grafeen is intrinsiek hydrofiel van aard (watercontacthoek van $42^{\circ} \pm 3^{\circ}$) 2) grafeen is *wetting transparant* voor water, wat betenkent dat het water-water interacties doorlaat, en 3) de kwaliteit van het grafeen-substraat grensvlak is een bepalende factor voor het ontstaan van de *wetting transparency* van grafeen.

Hoofdstuk 6 is het enige hoofdstuk in dit proefschrift dat niet per se de interactie tussen grafeen en vloeistoffen bestudeert. Het voegt echter wel een belangrijk inzicht toe aan het geheel van het in dit proefschrift beschreven onderzoek, namelijk, dat de *wetting* eigenschappen van grafeen op macroscopisch niveau niet eenduidig vertaald kunnen worden naar de interactie tussen grafeen en individuele watermoleculen. Concepten als hydrofiliciteit en hydrofobiciteit

worden vaak gebruikt om andere fenomenen te kunnen beschrijven, zoals bijvoorbeeld adsorptie, desorptie en chemische affiniteit jegens bepaalde typen stoffen. En hoewel het vinden van correlaties tussen dezen breder perspectief biedt, kan een algehele generalisatie leiden tot onjuiste conclusies. In het bijzonder, hoofdstuk 6 laat zien dat de kristalliniteit van het gegroeide substraat de desorptie kinetiek van watermoleculen van grafeen kan beïnvloeden, maar geen effect heeft op de macroscopische wettability.

Grafeen en andere 2D-materialen bieden unieke mogelijkheden voor onderzoek en technologie, maar eisen daarvoor wel een bijzondere aanpak en de ontwikkeling van alternatieve hulpmiddelen en karakterisatiemethodes, anders dan die normaal gebruikt worden voor 3D materialen. De aanpak die in dit proefschrift wordt beschreven heeft reeds enkele interessante inzichten verschaft maar, des te belangrijker, bidet ook een aanknopingspunt voor verdere ontwikkeling. Een eerste aanzet is in dit proefschrift beschreven en methodologieën kunnen rechtstreeks toegepast worden op andere 2D van der Waals materialen, zoals hexagonaal boor-nitride, dichalcogeniden en fluorgrafeen.

Bovendien, de karakterisatie en elektronische metingen van grafeen, gesitueerd op vloeistofgrensvlakken, zoals beschreven in hoofdstukken 2 en 3, levert de mogelijkheid voor het *in situ* bestuderen van grensvlakfenomenen door het variëren van de oplosmiddelsamenstelling, het oplossen van stoffen of surfactanten, het aanbrengen van een *gate voltage*, een magnetisch veld, of andere externe stimuli. Chemisch gefunctionaliseerd grafeen kan worden gebruikt om de interactie tussen het vloeistofmedium en de opgeloste stoffen af te stemmen. Bovendien, Surface Enhanced Raman Spectroscopy (SERS), zoals beschreven in hoofdstuk 3, kan in tegenstelling tot conventionele Raman spectroscopie, toegepast worden om subtiele veranderingen op het grensvlak waar te kunnen nemen met een hogere resolutie.

Het relaxeren van de spanning en het vergroten van de *charge carrier mobilities* – mogelijk de belangrijkste bevindingen van dit proefschrift – maken vloeistofoppervlakken met grafeen in het bijzonder aantrekkelijk voor het *in situ* bestuderen van vloeistoffen: vloeistoffen staan een verhoogde gevoeligheid toe (door het reduceren van de spanning en vergroting van de charge carrier

mobilities) en dient tegelijkertijd als een experimenteel medium. Technische implementatie wordt echter verhinderd door één grote uitdaging: het elektrisch meten van een één-atoom-dikke laag grafeen, op een vloeistofoppervlak is extreem moeilijk, zelfs in een laboratoriumomgeving (zie hoofdstuk 2). Om dit te bewerkstelligen dienen een aantal problemen te worden opgelost: het aanbrengen van een betrouwbaar grafeen-electrode contact, waarbij de structurele integriteit intact blijft, en het grafeen dient gestabiliseerd te worden op het wateroppervlak. De inherente flexibiliteit is een significant nadeel voor het gebruik van vloeistofoppervlakken voor grafeenonderzoek. Als alternatief voor directe elektrische metingen, werd *remote electrical probing* van grafeen in vloeistof toegepast, ook vanwege de snelle ontwikkeling die deze techniek momenteel ondergaat.

Hoewel vaste substraten niet volledig door vloeistoffen vervangen kunnen worden in grafeenonderzoek, laat dit proefschrift zien dat de voordelen die vloeistoffen rieden hun toepassing vinden in een breed aantal onderzoeksgebieden. In een wereld die zoekt naar oplossingen voor duurzame energie zullen vloeistoffen vanwege de commerciële beschikbaarheid (in het bijzonder in vergelijking met vaste substraten in high-tech industrieën) zondermeer een essentieel onderdeel gaan vormen van toekomstige technologieën. De resultaten die in dit proefschrift zijn beschreven dragen bij aan deze trend door de ontwikkeling van concepten en middelen die het gebruik van vloeistoffen in combinatie met grafeen mogelijk maakt, en door te bewijzen dat simpele en duurzame oplossingen superieure resultaten op kunnen leveren.

Curriculum Vitae

Liubov A. Belyaeva was born in Naberezhnie Chelny, Russia, on July 7th 1990.

She attended primary and secondary schools in Elabuga, Russia, and high school with the focus on Mathematics and Physics in Naberezhnie Chelny, from which she graduated in 2007.

In 2007 she was admitted to the Department of Materials Sciences of the Moscow State University, where she received her Bachelor degree in Materials Science in 2011 with the thesis "Disaggregation and formation of a secondary structure in detonation nanodiamonds" (advisor prof. Michael V. Korobov).

She completed her master studies at the Department of Materials Sciences of the Moscow State University, and received her Master degree in Chemistry in 2013. Her master research was focused on graphene and graphite oxide solvates and adaptation of the thermodynamic methods for the characterization of nanomaterials, and yielded the thesis "Thermodynamic properties of graphite oxide solvates" (advisor prof. Michael V. Korobov).

As a part of her master studies, in 2012 she undertook an internship at the University of Erlangen-Nuremberg, Germany, in the group of Functional Carbon Allotropes, where she worked on the hydrogenation of graphene under modified Birch conditions (advisor prof. Andreas Hirsch).

In November 2014 she started a joint PhD between Chemistry and Physics departments of Leiden University, in the group of Supramolecular and Biomaterials Chemistry, under supervision of Gregory F. Schneider and with Jan Aarts and Alexander Kros as promotor. Her work mainly focused on the investigation and development of liquid platforms for graphene application and is summarized in this thesis.

During her PhD she collaborated with the Leiden Institute of Physics, in particular with the groups of prof. Jan Aarts and prof. Sense Jan van der Molen. She supervised bachelor and master students, and assisted in the practical and laboratory courses "Practicum Basisvaardigheden", "Scheikunde" and "Natuurkunde".

She also had the opportunity to present her work in various workshops and conferences in the Netherlands, France and Greece:

- CHAINS 2017, Veldhoven, Netherlands. Hydrophilicity of free-floating graphene on water. Poster presentation.
- Graphene week 2017, Athens, Greece. Hydrophilicity of free-floating graphene on water. Oral presentation.
- European Conference on Chemistry of Two-Dimensional Materials (Chem2DMat) 2017, Strasbourg, France. Molecular caging of graphene with cyclohexane: a chemical platform for liquid-liquid electronics and transfer. Poster presentation.
- CHAINS 2016, Veldhoven, Netherlands. Molecular caging of graphene with cyclohexane: a chemical platform for liquid-liquid electronics and transfer. Poster presentation.

List of publications

1. A. V. Prydatko*, L.A. Belyaeva*, L. Jiang, L. M. C. Lima and G. F. Schneider. Contact angle measurement of free-standing square-millimeter single-layer graphene. *Nature Communications* 9, 4185, **2018**. * *Equal contribution*
2. B. Bera, N. Shahidzadeh, H. Mishra, L.A. Belyaeva, G.F. Schneider and D. Bonn. Wetting of water on graphene nanopowders of different thicknesses. *Applied Physics Letters* 112 (15), 151606, **2018**.
3. L.A. Belyaeva, P.M.G. van Deursen, K.I. Barbetsea and G.F. Schneider. Hydrophilicity of graphene in water through transparency to polar and dispersive interactions. *Advanced Materials* 30 (6), 1703274, **2018**.
4. L.A. Belyaeva, W. Fu, H. Arjmandi-Tash and G.F. Schneider. Molecular caging of graphene with cyclohexane: transfer and electrical transport. *ACS Central Science* 2 (12), 904-909, **2016**.
5. H. Arjmandi-Tash, L.A. Belyaeva and G.F. Schneider. Single molecule detection with graphene and other two-dimensional materials: nanopores and beyond. *Chemical Society Reviews* 45 (3), 476-493, **2016**.
6. S. You, J. Yu, B. Sundqvist, L. A. Belyaeva, N. V. Avramenko, M.V. Korobov and A. V. Talyzin. Selective intercalation of graphite oxide by methanol in water/methanol mixtures. *The Journal of Physical chemistry C*, 117, pp. 1963-1968, **2013**.
7. M. V. Korobov, D. S. Volkov, N. V. Avramenko, L. A. Belyaeva, P.I. Semenyuk and M. A. Proskurnin. Improving the dispersity of detonation nanodiamond: differential scanning calorimetry as a new method of controlling the aggregation state of nanodiamond powders. *Nanoscale*, 5, pp. 1529-1536, **2013**.
8. L. A. Belyaeva and G.F. Schneider. Wettability of graphene. *Submitted*
9. L.A. Belyaeva, L.Jiang and G.F. Schneider. Liquids relax and unify strain in graphene. *Under revision*.